# Small scale turbulence in high Karlovitz number premixed flames

Thesis by

Brock D. Bobbitt

In Partial Fulfillment of the Requirements

for the Degree of

Doctor of Philosophy

**Caltech**

California Institute of Technology

Pasadena, California

2016

(Defended March 1st, 2016)

This is dedicated to my wife, Lindsay,

who contributed no less than myself towards the completion of this work.

# Acknowledgments

I am in debt to the guidance and instruction provided by the professors here at Caltech. They have inspired me towards the pursuit of truth and excellence, while fostering a supportive academic community. Within this community, I would especially like to thank my committee members, Prof. Joseph Shepherd, Prof. Tim Colonius, and Prof. Melany Hunt. I specifically want to acknowledge my graduate research advisor, Professor Guillaume Blanquart, for his support and guidance which spurred my growth in many areas, including a love of chemistry, developing logical arguments, formulating research questions, and enjoying math. Without his encouragement, the work in this thesis would not have been possible.

I want to acknowledge my family: my wife, Lindsay, and daughters, Aubrey and Annabelle.

Lindsay's resolve and commitment was instrumental to the completion of this thesis. I am deeply grateful for her support. Thank you Aubrey and Annabelle for your smiles and patience. The emotional and practical support of our parents, Brian, Cherri, Joe, and Eileen gave us strength during our time here. Lastly, I want to thank our Lake Avenue Church community for their friendship and faithful help.

# Abstract

The purpose of this thesis is to characterize the behavior of the smallest turbulent scales in high Karlovitz number ($Ka$) premixed flames. These scales are particularly important in the two-way coupling between turbulence and chemistry and better understanding of these scales will support future modeling efforts using large eddy simulations (LES). The smallest turbulent scales are studied by considering the vorticity vector, $\boldsymbol{\omega}$, and its transport equation.

Due to the complexity of turbulent combustion introduced by the wide range of length and time scales, the two-dimensional vortex-flame interaction is first studied as a simplified test case. Numerical and analytical techniques are used to discern the dominate transport terms and their effects on vorticity based on the initial size and strength of the vortex. This description of the effects of the flame on a vortex provides a foundation for investigating vorticity in turbulent combustion.

Subsequently, enstrophy, $\omega^2 = \boldsymbol{\omega} \cdot \boldsymbol{\omega}$, and its transport equation are investigated in premixed turbulent combustion. For this purpose, a series of direct numerical simulations (DNS) of premixed $n$-heptane/air flames are performed, the conditions of which span a wide range of unburnt Karlovitz numbers and turbulent Reynolds numbers. Theoretical scaling analysis along with the DNS results support that, at high Karlovitz number, enstrophy transport is controlled by the viscous dissipation and vortex stretching/production terms. As a result, vorticity scales throughout the flame with the inverse of the Kolmogorov time scale, $\tau_\eta$, just as in homogeneous isotropic turbulence. As $\tau_\eta$ is only a function of the viscosity and dissipation rate, this supports the validity of Kolmogorov's first similarity hypothesis for sufficiently high $Ka$ numbers ($Ka \gtrsim 100$). These conclusions are in contrast to low Karlovitz number behavior, where dilatation and baroclinic torque have a significant impact on vorticity within the flame. Results are unaffected by the transport model, chemical model,

turbulent Reynolds number, and lastly the physical configuration.

Next, the isotropy of vorticity is assessed. It is found that given a sufficiently large value of the Karlovitz number ($Ka \gtrsim 100$) the vorticity is isotropic. At lower Karlovitz numbers, anisotropy develops due to the effects of the flame on the vortex stretching/production term. In this case, the local dynamics of vorticity in the strain-rate tensor, $S$, eigenframe are altered by the flame. At sufficiently high Karlovitz numbers, the dynamics of vorticity in this eigenframe resemble that of homogeneous isotropic turbulence.

Combined, the results of this thesis support that both the magnitude and orientation of vorticity resemble the behavior of homogeneous isotropic turbulence, given a sufficiently high Karlovitz number ($Ka \gtrsim 100$). This supports the validity of Kolmogorov's first similarity hypothesis and the hypothesis of local isotropy under these condition. However, dramatically different behavior is found at lower Karlovitz numbers. These conclusions provides/suggests directions for modeling high Karlovitz number premixed flames using LES. With more accurate models, the design of aircraft combustors and other combustion based devices may better mitigate the detrimental effects of combustion, from reducing $CO_2$ and soot production to increasing engine efficiency.

# Published Content

Chapter 2 is based in large part on the publication [104]: B. Savard, Y. Xuan, B. Bobbitt, and G. Blanquart. A computationally-efficient, semi-implicit, iterative method for the time-integration of reacting flows with stiff chemistry. *J. Comput. Physics*, 295:740-769, 2015.

http://dx.doi.org/10.1016/j.jcp.2015.04.018.

http://www.sciencedirect.com/science/article/pii/S0021999115002648.

Chapters 4 and 5 are based in large part on the publication [8]: Brock Bobbitt, Simon Lapointe, and Guillaume Blanquart. Vorticity transformation in high Karlovitz number premixed flames. *Phys. Fluids*, 28, 015101 (2016). http://dx.doi.org/10.1063/1.4937947.

http://scitation.aip.org/content/aip/journal/pof2/28/1/10.1063/1.4937947.

# Contents

# List of Figures

# List of Tables

# Chapter 1

# Introduction

## 1.1 Background

### 1.1.1 Motivation

Combustion is a central component of energy production in our world today. Its important role in supporting the activities of society is demonstrated in the annual report of the U.S. Energy Information Administration [114]. Among the different energy sources, eighty-percent of all energy currently consumed in the U.S. comes from combustion. Furthermore, the U.S. Energy Information Administration predicts that combustion based energy sources will continue to supply this same large fraction of energy into the foreseeable future (Fig. 1.1). The near ubiquitous use of combustion can be explained by its advantageous characteristics: the ease of accessing combustion fuels (wood, oil, coal, *etc.*), the relative abundance of these fuels, the ability to store and transport these fuels, the simple process by which the internal energy is released, and the legacy of previous technologies for converting the energy into useful work.

The use of combustion as an energy source is, however, not without dangers and disadvantages. Some of these include the danger of uncontrolled combustion, limited fuel resources, detrimental health and environmental effects of soot and $NO_x$, emission of green-house gases, and high temperatures constraining engineering design. Because of the extensive use of combustion, each of these drawbacks deserves the attention of scientific research and creative engineering to eliminate or mitigate their detrimental effects.
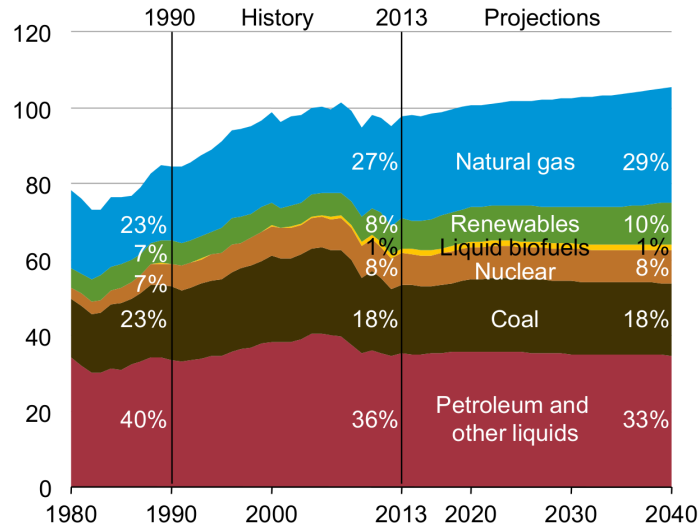
Figure 1.1: U.S. primary energy usage by fuel with projections to 2040 in quadrillion Btu. Figure adapted from Ref. [114].

As a relevant example, energy consumption by transportation accounts for one-quarter of all energy usage in the US. Aircrafts alone are responsible for nearly 10% of this energy production, and this fraction is predicted to increase [114]. To address the detrimental effects of combustion, aircraft engines are under strict emission requirements based on their noise and chemical exhaust products, including $NO_x$ [30] and possibly $CO_2$ in the future [29]. In order to meet these increasingly stringent emissions requirements and improve performance and efficiency, aircraft combustor design is moving towards lean premixed combustion at highly turbulent conditions [39].

Engine development requires a significant amount of engineering and design testing. This often comes with substantial costs of time and resources due to construction of prototypes and the difficulty of predicting the complex turbulent combustion processes occurring in these highly turbulent engines. To minimize these costs and support engineering advancement, computational modeling of engines is increasingly a central part of the design cycle. The purpose of this thesis is to further understand the fundamental processes in premixed turbulent combustion to support improved modeling efforts of practical devices like aircraft combustors.

The large eddy simulation (LES) framework [97, 82] is a promising numerical tool for the purpose of obtaining accurate engine performance information at a reasonable computational cost. This
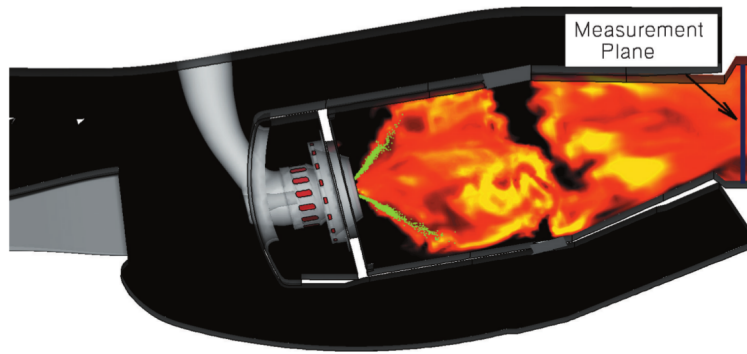
Figure 1.2: LES of a Pratt and Whitney gas turbine combustor. Figure adapted from Ref. [62].

modeling tool has been used previously for numerical simulations of aircraft engines, as shown in Fig. 1.2. LES, in its basic form, resolves the large scale flow features in space and time, called the resolved scales. By applying a spatial filter over the smaller flow features, called subfilter scales, these scales are unresolved and their effects are modeled. While various models have been developed for the subfilter scales in homogeneous isotropic turbulence [21, 107, 89], LES of turbulent combustion remains an active area of research.

More precisely, LES of premixed turbulent combustion requires further development and model validation. For instance, models applied within premixed turbulent combustion [79, 48, 108, 68] were often developed for homogeneous isotropic turbulence and use the Kolmogorov hypotheses within the model. The three Kolmogorov hypotheses include the hypothesis of local isotropy, first similarity hypothesis, and second similarity hypothesis. The first two hypotheses relate to small scale turbulence. They state that the smallest turbulence scales are isotropic, and they depend only on the viscous dissipation rate, $\epsilon$, and the kinematic viscosity, $\nu$, respectively [53, 87]. It is not clear if these two hypotheses are still valid in premixed turbulent combustion, where the density and viscosity vary significantly and the flame introduces specific length and velocity scales [79]. To develop accurate LES models for turbulent combustion, testing these two hypotheses and characterizing the behavior of the smallest turbulent scales are particularly relevant as these scales are smaller than the filer width, $\Delta$, and must be modeled.

## 1.1.2 Combustion Regimes

Turbulent combustion involves the two-way coupling between turbulence and chemistry [121, 25, 85, 3]. This includes the individual yet connected processes of turbulence impacting the flame structure [79, 3, 101, 83, 105] and the flame altering the turbulence characteristics [58, 73, 14, 38]; each process is integral to understanding and predicting the behavior of turbulent combustion [58]. In premixed turbulent combustion, the coupling of the flame and turbulence has been qualitatively described by the commonly used premixed turbulent combustion regime diagram [79, 3, 101, 38, 16]. This diagram, presented in Fig. 1.3, delineates different qualitative modes of combustion by the relation of the flame time scale ($\tau_F$) to that of the smallest turbulent eddies ($\tau_\eta$), defined as the Karlovitz number ($Ka$),

$$Ka = \frac{\tau_F}{\tau_\eta}, \tag{1.1}$$

with $\tau_\eta$ being the Kolmogorov time scale

$$\tau_\eta \equiv \left(\frac{\nu}{\epsilon}\right)^{1/2}, \tag{1.2}$$

where $\nu$ is the kinematic viscosity and $\epsilon$ is the dissipation rate. $\tau_F$ is evaluated as

$$\tau_F = \frac{l_F}{S_L}, \tag{1.3}$$

with $S_L$ being the laminar flame speed and $l_F$ being the laminar flame thickness. The laminar flame thickness is defined here as the thermal width, $l_F = (T_b - T_u)/|\nabla T|_{max}$, where subscripts $b$ and $u$ represent quantities evaluated in the burnt products and unburnt reactants, respectively.

By defining the turbulence integral length scale as $l = u_o^3/\epsilon$ (where $u_o$ is the integral velocity scale), assuming $D = S_L l_F$ (where D is the molecular diffusivity), and assuming unity Schmidt number ($Sc \equiv \nu/D = 1$), the Karlovitz number may be written as

$$Ka^* = \left(\frac{l_F u_o^3}{l_o S_L^3}\right)^{1/2}. \tag{1.4}$$
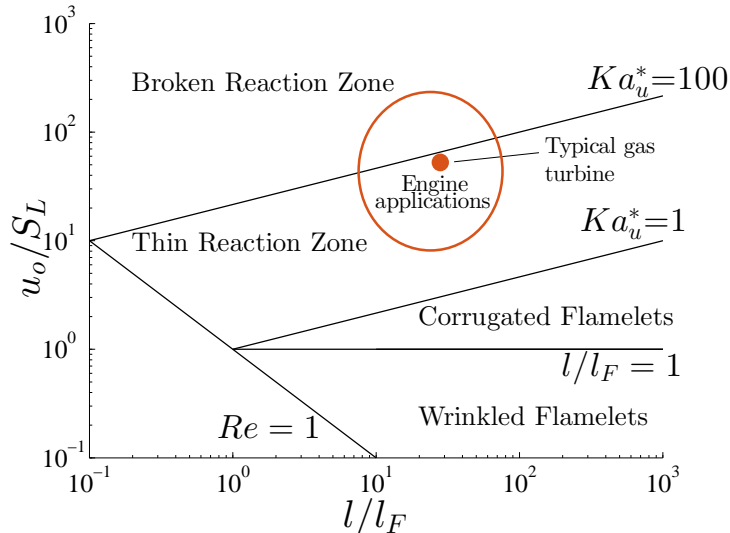
Figure 1.3: Peters' regime diagram of premixed turbulent combustion [79] with the location of a typical gas turbine [24] superimposed on the diagram. The Reynolds number is defined as $Re = u_o l / \nu$.

This form of the Karlovitz number allows the different modes of combustion to be distinguished based on integral properties of the flow, as shown in Fig. 1.3, and is often used for reporting experimental and numerical results [79]. It is common to evaluate the Karlovitz number using the turbulence characteristics in the unburnt flow; this quantity is referred to here as the unburnt Karlovitz number $(Ka_u^*)$.

When the smallest turbulent time scale is larger than the flame time scale, the turbulence is only able to alter the large scale geometry of the flame surface, which corresponds to the wrinkled and corrugated flamelet regimes $(Ka_u^* < 1)$. The turbulence is able to manipulate the flame geometry to a greater extent in the corrugated flamelet versus the wrinkled flamelet regime. When $\tau_\eta$ is smaller than $\tau_F$, the turbulence is expected to penetrate and alter the internal structure of the flame $(Ka_u^* > 1)$. The behavior at higher Karlovitz numbers is separated into two regimes: the thin and broken reaction zone regimes. Between $1 < Ka_u^* < 100$, the turbulence is expected to only alter the preheat zone, leaving the reaction zone unaltered. This is called the thin reaction zone. In this regime, the chemical structure of the flame is expected to resemble its laminar counterpart. As the turbulent eddies become smaller, they are eventually able to penetrate the interior reaction zone and alter its chemical structure. This is called the broken reaction zone and is estimated to occur

for $Ka_u > 100$.

Relevant engine applications are at high Karlovitz numbers, such as a typical gas turbine engine, which resides at the border between the thin and broken reaction zone regimes [24]. Other applications, such as scramjet combustors, extend to even higher Karlovitz numbers [90]. These regimes are less well studied both experimentally and numerically than lower Karlovitz number regimes.

Previous studies have also shown the importance of the local Karlovitz number, $Ka$, (as opposed to $Ka_u$) in determining the internal flame structure [55]. As the Karlovitz number is controlled by the smallest turbulent scales, it is important to describe the behavior of these turbulent scales within the flame to better understand the effects on the flame by turbulence. More fundamentally, the significance of $\tau_\eta$ within the definition of the Karlovitz number relies on the assumption that the smallest turbulent scales depend on $\nu$ and $\epsilon$ alone (Eq. 1.2, Kolmogorov's first similarity hypothesis), which, as mentioned previously, has not been tested within premixed flames.

Considering the above, the focus of this thesis is on the behavior of the smallest turbulent scales within high Karlovitz number premixed flames. To reiterate, investigating the smallest turbulent scales is particularly important as they must be modeled in LES [82, 70], their behavior relates to two of the Kolmogorov hypotheses (the first similarity hypothesis, and local isotropy [53, 87]), and they are responsible for altering the internal structure of the flame [3, 85, 103, 102, 55].

## 1.1.3  Vorticity

To study the effects of the flame on the incoming turbulence, previous studies have considered various quantities. Many focused on quantities related to the turbulent kinetic energy (TKE) transport equation, often for modeling purposes [9, 127, 77, 15, 16]. Though studying the TKE provides valuable insight into the integral scales, it does not describe the behavior of the smallest scales. Other studies focused on the rate of strain tensor,

$$S = \frac{1}{2}(\nabla \boldsymbol{u} + \nabla \boldsymbol{u}^T), \tag{1.5}$$

for its relevance to the transport equation of the reaction progress variable scalar dissipation rate [17] and is found to be related to flame stretch [17, 18, 109, 110]. The rate of strain tensor has been studied for the alignment of its principle axes with various quantities such as the flame normal and vorticity [110, 38, 14]. Used in this way, the rate of strain tensor provides detailed information on the dynamics of the flame-turbulence interaction, but does not directly provide information about the smallest turbulence scales. Study of the smallest turbulent scales can be accomplished through the energy spectrum [52]; however, evaluating the energy spectrum along a line in physical space, which crosses different regions (for instance burnt and unburnt) of a curved, turbulent flame, does not precisely measure the evolution of the energy spectrum as a function of progress through the flame.

In order to study the behavior of the smallest turbulent scales, the vorticity vector,

$$\boldsymbol{\omega} = \nabla \times \boldsymbol{u}, \tag{1.6}$$

and the terms in its transport equation may be investigated. Vorticity, like dissipation, has been shown to scale with the smallest turbulent scales in homogeneous, isotropic turbulence [46, 72, 88, 113]. Previous studies focused on the vorticity for the importance of the vortex-stretching mechanism in the energy cascade and its appearance in the scalar gradient transport equation [38, 37, 14, 59]. It is advantageous to consider vorticity, as it may be evaluated locally in physical space without the use of Fourier transforms (which require periodicity), and it may be projected onto various coordinate systems, such as the eigenframe of the strain-rate tensor, providing insights into the local flame-turbulence dynamics. Furthermore, vorticity has a known transport equation, and the terms in its transport equation may be readily related to physical processes. For these reasons, vorticity provides insight into the behavior of the smallest turbulent scales along with the processes affecting their behavior. Thus, vorticity is used in this work to study the smallest turbulent scales.

Both the magnitude and individual components of the vorticity vector provide useful insight into the behavior of the smallest turbulent scales. In homogeneous isotropic turbulence, the vorticity

magnitude scales with $1/\tau_\eta$. As $\tau_\eta$ is a function of the dissipation rate and kinematic viscosity alone, the relationship $|\omega| \propto 1/\tau_\eta$ is simply a restatement of Kolmogorov's first similarity hypothesis. Therefore, by studying enstrophy,

$$\omega^2 = \boldsymbol{\omega} \cdot \boldsymbol{\omega}, \tag{1.7}$$

it is possible to assess the validity of this hypothesis in premixed flames. By comparison of the three components of the vorticity vector, it is possible to assess the effects of the flame on the small scale isotropy, which relates the Kolmogorov's hypothesis of local isotropy.

The goal of this thesis is to characterize the transport of the vorticity magnitude and isotropy in high Karlovitz number premixed flames. The evolution of these quantities is studied by considering their transport equations. The vorticity transport equation is derived from the momentum equation and written as

$$\frac{D\boldsymbol{\omega}}{Dt} = S \cdot \boldsymbol{\omega} - \boldsymbol{\omega}\left(\nabla \cdot \boldsymbol{u}\right) + \frac{1}{\rho^2}\left(\nabla\rho \times \nabla P\right) + \nabla \times \left(\frac{1}{\rho}\nabla \cdot \tau\right), \tag{1.8}$$

where $D/Dt$ is the material or total derivative, $\rho$ is the density, $\boldsymbol{u}$ is the velocity vector, $P$ is the pressure, and $\tau$ is the viscous stress tensor. Equation 1.8 represents a set of three equations, one for each component of the vorticity vector. Each term on the right hand side is associated with a specific physical process: production/vortex stretching, dilatation, baroclinic torque, and viscous diffusion, respectively. Production and viscous diffusion are active even when density is constant, while dilatation and baroclinic torque arise here only due to the presence of the flame. The change in fluid properties (such as density and viscosity) within a premixed flame alters the vorticity of the incoming turbulence through these terms. The enstrophy transport equation is obtained by taking the dot product of vorticity with this set of equations.

Previous DNS studies at low Karlovitz numbers found the turbulence characteristics within the flame to be significantly different than in homogeneous isotropic turbulence. For example, Lipatnikov et al. [59] observed that large density ratios resulted in an average production of vorticity in the flame and that dilatation and baroclinic torque played a significant role in the transport of enstrophy. Additionally, Kolla et al. [52] showed a collapse of the viscous scales in the turbulent kinetic energy

spectrum when normalizing using the flame thickness. At high Kalovitz number, the behavior of the vorticity transport terms is largely unclear, but these previous results suggest the possibility that baroclinic torque and dilatation (absent in homogeneous isotropic turbulence) may dominate or dramatically alter the behavior of vorticity in the flame from that of homogeneous isotropic turbulence.

## 1.2 Previous work

### 1.2.1 Vortex-flame interaction

The interaction of a two-dimensional (2D) vortex with a laminar flame is a unique test problem because it captures many aspects of the coupling of the fluid mechanics and the chemistry while remaining laminar. For instance, the vortex-flame interaction may be used to investigate the effects of the flame on the fluid mechanics as, analogous to turbulence, vorticity and velocity structures cross the flame. It may also be studied for the effects of the fluid mechanics on the flame, as it contains a combination of hydrodynamic effects such as positive curvature, negative curvature, strain, and unsteady dynamics [123, 26]. Through this, changes in the flame structure may be examined [5, 115]. Additionally, the vortex-flame interaction has application to practical situations in which vortices interact directly with a flame [71]. These vortices are often large scale coherent structures within a turbulent flow.

Furthermore, the vortex-flame interaction has been also used as a model for premixed turbulent combustion, as turbulence has been considered as a collection of vortices. Arguments based on associating turbulent length and velocity scales as individual eddies interacting with a flame extend back to the Klimov-Williams criterion [49, 121] as well as the Gibson scale [78], where premixed turbulent combustion behavior has been inferred based on these individual interactions.

This idea was applied by Poinsot *et al.* [83] and a regime diagram was constructed based on vortex-flame simulations. Using numerical simulations, they investigated a dipole vortex interacting with a planar flame and focused on local flame extinction. These results were later used as support

for the premixed turbulent combustion regime diagram by Peters [79]. Here, again, various eddies within a turbulent flow were modeled by the behavior of an individual vortex of the same length and velocity scale. This has been used less as a reduced order model in application, like in LES, but more as a means to explain and predict qualitative behavior. Considering these applications, the vortex-flame interaction provides a computationally, analytically, and experimentally approachable test problem which captures multiple aspects of the chemistry and fluid mechanics present in turbulent combustion. A review of additional previous studies on the vortex-flame interaction follows.

Rutland and Ferziger [95] investigated the interaction of a monopole vortex with a premixed flame. They furthered the work of Poinsot $et$ $al.$ [83] showing that different sizes and strengths of vortices resulted in different effects on both the flame and vortex. Their analysis produced different regimes of qualitatively unique behavior based on the Damköhler number, defined as the ratio of the vortex time scale, $\tau_v = l_v/u_v$ (where $l_v$ and $u_v$ are the vortex characteristic length and velocity scales), to the flame time scale. They used a single-step Arrhenius reaction rate to model the chemistry.

Roberts $et$ $al.$ [93] carried out experiments with analysis similar to Poinsot $et$ $al.$ [83], presenting modifications to the boundaries in their regime diagram along with additional Lewis number ($Le$) effects. Their experiments covered a range of vortex to flame length scale ratios, $l_v/l_F = 1 - 5.3$, and velocity scale ratios, $u_v/S_L = 9.3 - 20$.

Mueller $et$ $al.$ [73] studied experimentally the vortex-flame interaction using vortex rings at a fixed length ratio, $l_v/l_F \simeq 10$ but with three velocity ratios, $u_v/S_L = 1.4, 3.6, 10.1$. They reported that the survival or destruction of the vortex varied with the three velocity ratios tested. Louch and Bray [60] performed a numerical study of one of these experimental cases, $u_v/S_L = 1.4$. They compared their simulation results against those of Mueller $et$ $al.$ [73] and also proposed three regimes describing whether the vortex survived past the flame. However, the regimes are based upon the value of the flame heat release and the mean pressure gradient. Their simulations relied on a one-step reaction with an Arrhenius reaction rate and constant viscosity and thermal diffusivity throughout the simulation. More recently, Moeck $et$ $al.$ [71] considered the interaction of a helical precessing

vortex core and a flame with relevance to swirl burners. A more complete review of vortex-flame interaction studies has been done by Renard *et al.* [92].

Despite the relevance of the vortex flame interaction, the effect of the flame on the vortex is not well characterized and this interaction has not been explored with analytical techniques. For instance, various parameters have been suggested to alter the resulting behavior of the vortex. However, a suitable analysis has not been performed to characterize the relative importance of the terms in the vorticity equation based on the size and velocity of the initial vortex. This lack of understanding of how the vorticity is modified by the flame is referenced in the review article covering the effects of a flame on turbulence by Lipatnikov and Chomiak [58]. Additionally, to the knowledge of the author, little information has been reported on the vortex characteristics after passing through the flame (beyond its survival or destruction). This information would be useful for the study of premixed turbulent combustion as it provides a foundation for understanding how the flame alters the vorticity through the terms in the vorticity transport equation and under what conditions each term is important.

## 1.2.2   Small scale turbulence

High Karlovitz number premixed flames have been the subject of relatively few previous studies [86, 2, 4, 102, 38, 84]. The reason for this is the difficulty of producing high Karlovitz number flames both numerically and experimentally. Furthermore, a larger portion of these studies has focused on the internal flame structure [86, 2, 4, 102, 55, 99] rather than the behavior of the turbulence [38, 37]. Examples of studies which focused on the flame include Aspden *et al.* [3], who investigated distributed burning in lean hydrogen flames, and Poludnenko and Oran [85, 86], who studied the mechanisms impacting the turbulent flame speed. A review of relevant studies on the behavior of the small turbulent scales follows.

### 1.2.2.1 Enstrophy

Several relevant conclusions have been made in previous work with respect to the evolution of vorticity in premixed flames [38, 59, 14, 84]. Chakraborty [14] analyzed data from direct numerical simulations (DNS) using one-step chemistry with $Ka_u^*$ up to 13 for the alignment of vorticity with the principle axes of the local strain rate tensor. It was found that the vortex-stretching term is on average positive even with different flame density ratios and Lewis numbers. Lipatnikov *et al.* [59] considered DNS at low unburnt Karlovitz numbers ($Ka_u^* = .2 - .3$). They found that dilatation and baroclinic torque are important in the transport of enstrophy and observed that large density ratios resulted in an average production of vorticity in the flame.

The only relevant study at high Karlovitz number is attributed to Hamlington *et al.* [38] who performed several simulations of high $Ka_u$ ($Ka_u^* = 3 - 125$) premixed $H_2$-air flames varying the turbulence intensity at a single value of $l/l_F$ and flame density ratio. These simulations relied on numerical viscosity using an implicit large eddy simulation (ILES) framework [35] and employed one-step chemistry with unity Lewis number assumption. In their work, the vorticity magnitude was observed to be reduced by heat release for low turbulence intensities, while at high turbulence intensities the flame weakly affected the vorticity magnitude. Recently, Poludnenko [84] discussed the magnitude of terms in the vorticity equation for moderately high values of the Karlovitz number ($Ka_u = 7 - 30$) from simulations of $H_2$-air premixed turbulent flames also relying on numerical viscosity in an ILES framework and using one-step chemistry with unity Lewis number assumption. It was observed that for the higher value of $Ka_u$ ($Ka_u = 30$), vorticity production had a similar magnitude through the flame as in the reactants. As viscosity is critical to the behavior of the smallest turbulent scales, it is relevant to consider if these observations of enstrophy in simulations relying on numerical viscosity are impacted by temperature dependent molecular viscosity, which increases through a flame.

Despite these previous contributions, it remains unclear how the flame affects enstrophy at high $Ka_u$, in what manner do terms in the enstrophy transport equation vary with parameters such as $Ka_u$ and the flame density ratio, and under what conditions Kolmogorov's first similarity hypothesis

is valid within premixed turbulent flames. Lastly, as viscosity is critical to the behavior of the smallest turbulent scales, it is unclear if these scales are accurately represented by a ILES framework which relies on numerical viscosity.

### 1.2.2.2 Vorticity Isotropy

Previous relevant studies on small scale isotropy within premixed flames also include those of Lipatnikov *et al.* [59], Poludnenko[84], and Hamlington *et al.*[38]. At low unburnt Karlovitz numbers, Lipatnikov *et al.* [59] found anisotropy in vorticity and related this primarily to the effects of baroclinic torque. Vortex stretching was found to be unimportant in these low $Ka_u^*$ simulations. At their lower Karlovitz number tested ($Ka_u = 7$), Poludnenko [84] found that the total production of vorticity was anisotropic, due to the significant role of dilatation and baroclinic torque. However, at the higher value of $Ka_u$ ($Ka_u = 30$), the total production of vorticity was largely isotropic. The only relevant study at higher Karlovitz numbers is again by Hamlington *et al.* [38, 37] ($Ka_u^* = 3 - 125$). In their work, they observed that anisotropy decreased as the turbulence intensity increased, and offered a possible explanation for anisotropy involving vortex stretching and the local alignment of vorticity and the flame. The effect of baroclinic torque and viscous dissipation on isotropy was not considered in their analysis.

Despite this previous work, it is still unclear if and when the smallest turbulent scales are isotropic within the flame. Additionally, it is uncertain what mechanism is responsible for producing small scale anisotropy and how this is impacted by different flow parameters.

### 1.2.3 Chemical and transport model effects

Previous DNS performed to the study the behavior of the flame at high Karlovitz numbers have largely employed finite-rate chemical models and non-unity Lewis number transport [2, 4, 102, 55, 99]. This is because the internal flame structure is altered by the turbulence at these conditions and different transport and chemical models result in different behavior of the flame. For example, Savard and Blanquart [102] found that with non-unity Lewis number transport (compared with

unity Lewis number transport) the fuel chemical consumption rate exhibited more local extinctions and its mean value was reduced by 40%. This variation in the fuel source term was found to significantly reduce the turbulent flame speed ($S_T/S_L$) compared to the unity Lewis number flame.

However, in previous numerical studies which focus on the turbulence behavior, DNS were often performed with simplified models for the chemistry and species transport. The relevant studies of Chakraborty [14], Lipatnikov *et al.* [59], Poludnenko [84], Hamlington *et al.* [38] all consider one-step chemical models with unity Lewis number transport. As noted by Chakraborty [14], it is unclear if the chemical and transport models impact the observed behavior of the turbulence. For example, one-step chemical models assume a single chemical pathway, whereas many engine-relevant applications use complex hydrocarbon fuels with many chemical pathways. At high $Ka_u$, when the turbulence is expected to disrupt the complex internal structure of the flame, the need to retain this structure in order to capture accurately the effects of the flame on the turbulence has not been studied. This knowledge is critical as it would support selecting models with minimal yet sufficient detail in order to numerically investigate the effects of the flame on turbulence accurately and efficiently.

## 1.3    Objective and outline

The primary goal of this thesis is to better characterize the behavior of the smallest turbulent scales in high Karlovitz number premixed flames through the study of vorticity. For this, three specific objectives are addressed. The first goal is to study how an individual vortex is altered by a premixed flame through the terms in the vorticity transport equation. The second goal is to characterize the behavior of enstrophy and its evolution through the turbulent flame. The final goal is to assess the isotropy of vorticity within the flame. The resulting conclusions are employed to assess Kolmogorov's first similarity hypothesis and hypothesis of local isotropy in high Karlovitz number premixed flames. The outline of this thesis is discussed subsequently.

To accomplish the above goals, we consider the low Mach number reacting flow equations used in combination with finite-rate, tabulated, or one-step chemistry models. These equations are presented

in chapter 2 along with the numerical solver used for the simulations performed in this work.

In chapter 3, the 2D vortex-flame interaction is investigated as a simplified test case for premixed turbulent combustion. The purpose of this chapter is to understand how the flame alters the vortex through the terms in the vorticity transport equation and when these terms are important given the initial size and strength of the vortex. This is accomplished by investigating the limiting behaviors of the vortex based on the ratios $u_v/S_L$ and $l_v/l_F$ through numerical and analytical techniques. Five different limiting behaviors are identified along with the dominant term in the vorticity transport equation in each case. The resulting effects on vorticity are characterized. This provides a qualitative framework for understanding the mechanisms by which the flame impacts vorticity.

To study premixed turbulent flames, a series of DNS with varying Karlovitz numbers, Reynolds numbers, and flame density ratios are performed and discussed in chapter 4. The simulations are of slightly lean $n$-heptane/air flames modeled with a finite-rate chemical model and constant non-unity Lewis numbers. This fuel is chosen as larger hydrocarbon fuels are often used in engine applications. Several additional DNS are performed, varying the chemical model and species Lewis numbers to investigate the effects of these modeling simplifications.

The second primary goal is to understand the transport of enstrophy through the flame (chapter 5). This is accomplished by deriving theoretical scaling estimates for each term of the enstrophy transport equation to explain their variation through the flame. Predictions from this analysis are tested using results from the present DNS. A normalized enstrophy transport equation is proposed which involves a small set of parameters so that the relative magnitude of vortex stretching, dilatation, baroclinic torque, and viscous dissipation may be predicted as a function of the Karlovitz number and flame conditions. This information is used to characterize the transport of ensrophy at high Karlovitz numbers and assess Kolmogorovs first similarity hypothesis, *i.e.* whether the small turbulent scales depend on $\epsilon$ and $\nu$ alone.

The third goal of this thesis is to characterize vorticity isotropy (chapter 6). Within this goal, the objectives are first to determine if the smallest turbulent scales are isotropic; and second, to isolate the processes which are primarily responsible for the production of small scale anisotropy in

high Karlovitz number premixed flames. Lastly, the final objective is to determine how different parameters (such as $Ka_u$ and $l/l_F$) impact small scale anisotropy.

Finally, the conclusions are summarized in chapter 7 and several points of application are made. While the development of subgrid scale models is beyond the scope of this present work, the above results are used to suggest directions for modeling these flames using LES.

# Chapter 2

# Governing equations and numerical solver[1]

In this chapter, the governing equations used throughout this work are discussed. This includes equations for the conservation of mass, conservation of momentum, species transport, and temperature. This is followed by an overview of the three different chemical models used. The numerical solver employed in this thesis is then described.

## 2.1 Governing equations

The reacting flows which are of interest to this work have a relatively low Mach number ($M_a$), with a value typically below 0.3 [23, 106, 103]. With this value of $M_a$, acoustic waves can be neglected and the pressure field may be separated into a fluctuating hydrodynamic pressure and spatially-invariant, but (potentially) time-dependent component, $P_o(t)$, $P(x,t)$ [23, 106, 122, 79], with

$$\frac{P(x,t)}{P_o(t)} = O\left(Ma_a^2\right).$$

(2.1)

To simplify the numerical algorithm, Soret and Dufour effects, body forces, and radiative heat transfer are ignored [76, 50, 106, 28]. The species molecular diffusion is assumed to be described by the Fickian law [76, 50, 106, 122, 79]. Under these assumptions, the evolution of the system is

---

[1]This chapter is based in large part on the publication [104]: B. Savard, Y. Xuan, B. Bobbitt, and G. Blanquart. A computationally-efficient, semi-implicit, iterative method for the time-integration of reacting flows with stiff chemistry. *J. Comput. Physics*, 295:740 − 769, 2015.

governed by the following low-Mach number reacting flow equations [64, 65], which include equations

for the conservation of mass, conservation of momentum, species transport, and temperature:

$$\frac{\partial \rho}{\partial t} + \nabla \cdot (\rho \boldsymbol{u}) = 0, \tag{2.2}$$

$$\frac{\partial \rho \boldsymbol{u}}{\partial t} + \nabla \cdot (\rho \boldsymbol{u} \otimes \boldsymbol{u}) = -\nabla P + \nabla \cdot \tau, \tag{2.3}$$

$$\frac{\partial \rho Y_i}{\partial t} + \nabla \cdot (\rho \boldsymbol{u} Y_i) = -\nabla \cdot \boldsymbol{j}_i + \dot{\omega}_i, \tag{2.4}$$

$$\frac{\partial \rho T}{\partial t} + \nabla \cdot (\rho \boldsymbol{u} T) = \nabla \cdot (\rho \alpha \nabla T) + \dot{\omega}_T - \frac{1}{c_P} \sum_i c_{p,i} \boldsymbol{j}_i \cdot \nabla T + \frac{\rho \alpha}{c_p} \nabla c_p \cdot \nabla T. \tag{2.5}$$

In these equations, $\rho$ is the density, $\boldsymbol{u}$ is the velocity vector, and $P$ is the hydrodynamic pressure.

Bold symbols are used to denote vectors. The viscous stress tensor is defined as

$$\tau = 2\mu \left( S - \frac{1}{3} (\nabla \cdot \boldsymbol{u}) I \right), \tag{2.6}$$

where $\mu$ is the mixture dynamic viscosity, and $I$ is the identity tensor. In the species equations, $Y_i$ is

the mass fraction of species $i$, $\dot{\omega}_i$ is the species chemical source term, and $\boldsymbol{j}_i$ is the species diffusion

mass flux vector defined as

$$\boldsymbol{j}_i = -\rho D_i \frac{Y_i}{X_i} \nabla X_i - \rho Y_i \boldsymbol{u}_c, \tag{2.7}$$

where

$$\boldsymbol{u}_c = -\sum D_i \frac{Y_i}{X_i} \nabla X_i \tag{2.8}$$

is the correction velocity, $X_i$ is the species mole fraction, and $D_i$ is the species molecular diffusivity.

In the temperature equation, $T$ is the temperature, $\dot{\omega}_T$ is the heat source term defined as $\dot{\omega}_T = \frac{-1}{c_p} \sum h_i \dot{\omega}_i$, where $h_i(T)$ is the species enthalpy, $c_{p,i}$ is the species heat capacity, $c_p$ is the mixture

heat capacity, $\alpha$ is the mixture thermal diffusivity, given by $\alpha = \lambda/(\rho c_p)$, and $\lambda$ is the mixture

thermal conductivity. These equations are combined with the ideal gas law as the equation of state,

$$\rho = P_o W / RT, \tag{2.9}$$

with $1/W = \sum Y_i/W_i$. Here, R is the universal gas constant, $W_i$ is the species molecular weight, and $P_o$ is the thermodynamic pressure.

The species molecular viscosities are calculated using standard kinetic theory [44]. The mixture molecular viscosity, $\mu$, is computed using a modified form of Wilke's formula [120, 55] and the mixture thermal conductivity, $\lambda$, is calculated following Mather *et al.* [67]. The individual species thermal conductivities are obtained using Euken's formula [31], and the individual species molecular diffusivities, $D_i$, are calculated through the relation $D_i = \alpha/Le_i$, where $Le_i$ are the species Lewis numbers. As differential diffusion is not the primary focus of this thesis, constant Lewis numbers (unity and non-unity) are employed in order to reduce computational cost [10].

## 2.2   Chemical models

Three different chemical models are used in this thesis. The majority of simulations are performed using finite-rate chemistry, while tabulated and one-step chemistry are employed to test the effects of using simplified chemical models.

### 2.2.1   Finite-rate chemistry

In finite-rate chemistry, the mixture is assumed to be composed of $N$ species and with a total of $K$ chemical reaction (forward and backward reactions counted separately). The species chemical source term of species $i$, $\dot{\omega}_i$, in Eq. 2.4 may be separated into a production term, $\dot{\omega}_i^+$, and a consumption term, $\dot{\omega}_i^-$, as

$$\dot{\omega}_i = \dot{\omega}_i^+ - \dot{\omega}_i^-. \tag{2.10}$$

With this definition, both the production term, $\dot{\omega}_i^+$, and the consumption term, $\dot{\omega}_i^-$, take positive values.

The production rate of species $i$, $\dot{\omega}_i^+$, is given by the sum of the contributions from all elementary

chemical reactions leading to the formation of this species

$$\dot{\omega}_i^+ = W_i \sum_{\substack{j=1 \\ \nu_{ji}>0}}^{r} \left[ \nu_{ji} k_j \prod_{\substack{s=1 \\ \nu_{js}<0}}^{N} \left( \frac{\rho Y_s}{W_s} \right)^{-\nu_{js}} \right], \tag{2.11}$$

where $r$ is the total number of chemical reactions and $\nu_{js}$ is the stoichiometric coefficient of species $s$ in reaction $j$ (negative for reactants and positive for products). The rate constant of reaction $j$ is $k_j$, and is given by the Arrhenius form, $k_j(T) = A_j T^{b_j} \exp^{-T_{a,j}/T}$, where $T_{a,j}$ is the activation temperature for this reaction. Similarly, the consumption rate of species $i$, $\dot{\omega}_i^-$, is given by the sum of the contributions from all elementary chemical reactions leading to the destruction of this species

$$\dot{\omega}_i^- = -W_i \sum_{\substack{j=1 \\ \nu_{ji}<0}}^{r} \left[ \nu_{ji} k_j \prod_{\substack{s=1 \\ \nu_{js}<0}}^{N} \left( \frac{\rho Y_s}{W_s} \right)^{-\nu_{js}} \right]. \tag{2.12}$$

## 2.2.2 Tabulated Chemistry

Flamelet generated manifolds (FGM), or tabulated chemistry [51, 33, 116, 91], may be used in place of finite-rate chemistry to reduce the computational cost. In tabulated chemistry the flame is modeled through a single progress variable, $C$, against which all fluid properties (including the chemical source term) are tabulated. Tabulation is performed here with the solution of a 1D unstretched flame using a finite-rate chemical model. The progress variable is often defined as the sum of several species mass fractions [69] and is governed by the transport equation

$$\frac{\partial \rho C}{\partial t} + \nabla \cdot (\rho \boldsymbol{u} C) = \nabla \cdot (\rho D \nabla C) + \dot{\omega}. \tag{2.13}$$

In tabulated chemistry, the transport equation for $C$ is used in place of the temperature and species transport equations. The use of tabulated chemistry relaxes the computational cost compared to finite-rate chemistry as a single scalar must be transported.

### 2.2.3 One-step chemistry

This thesis also considers one-step chemistry, where only the global reactants and products are transported. The chemical source terms are determined through a single irreversible, one-step reaction, written generally as

$$\nu_{\mathrm{F}}\mathrm{F} + \nu_{\mathrm{O}}\mathrm{O} \rightarrow \nu_{\mathrm{P}_1}\mathrm{P}_1 + \nu_{\mathrm{P}_2}\mathrm{P}_2, \tag{2.14}$$

where F is the fuel species, O is the oxidizer, $P_i$ are the products, and $\nu_i$ are their respective stoichiometric coefficients. The reaction rate is determined through a second-order Arrhenius kinetics,

$$\omega_{\mathrm{i}} = \nu_{\mathrm{i}}[\mathrm{F}][\mathrm{O}]\mathrm{A}\exp(-\mathrm{T_a/T}). \tag{2.15}$$

The rate constant, $A$, and activation temperature, $T_a$, are chosen here so that the 1D unstretched laminar flame speed ($S_L$) and thickness ($l_F$) closely match those of the respective finite-rate mechanism. One-step chemistry requires less computation resources compared to finite-rate chemistry as fewer species must be transported.

## 2.3 Numerical solver

The governing equations are solved using the multiphysics and multi-scale, low-Mach number, finite difference, reacting flow solver NGA [23]. The NGA code allows for accurate, robust, and flexible numerical simulations of both laminar and turbulent flows [124, 125, 126], constant and variable density flows [23, 11, 118], as well as LES [125, 74] and DNS [6, 118, 12]. This numerical solver has been shown to conserve discretely mass, momentum, and kinetic energy, with arbitrarily high order spatial discretization [23].

Variables in NGA are staggered in both space and time [23]. All scalar quantities ($\rho$, $T$, $Y_i$, $P$) are stored at the cell centers while the velocity components are each stored on the respective cell faces. The variables are advanced in time using the second-order semi-implicit Crank-Nicolson scheme of Pierce and Moin [80].

This numerical scheme employs an iterative procedure to fully cover the non-linearities in the Navier-Stokes equations. This iterative procedure has been found of critical importance for stability and accuracy considerations [23, 106, 80]. Three to four sub-iterations are often used to provide the sufficient accuracy with the highest level of efficiency. The sequence of the numerical algorithm through one time step is subsequently described, where a uniform time step $\Delta t$ is employed. The density, pressure, and scalar fields are advanced from time level $t^{n+1/2}$ to $t^{n+3/2}$, and the velocity fields are advanced from time level $t^n$ to $t^{n+1}$. The total number of sub-iterations for one time step is denoted as $Q$. The chemical source terms are integrated explicitly in the following for the purpose of clarity.

0.  Upon convergence of the previous time step, the density, $\rho^{n+1/2}$, pressure, $P^{n+1/2}$, velocity fields, $\boldsymbol{u}^n$, and scalar fields, $\boldsymbol{Y}^{n+1/2}$, are stored, where $\boldsymbol{Y}$ represents the vector of species mass fractions $(Y_1, ..., Y_N)$. The solutions for pressure, species mass fractions, and momentum (from the previous time step) are used as initial best guesses for the forthcoming iterative procedure,

$$P_0^{n+3/2} = P^{n+1/2}, \quad \boldsymbol{Y}_0^{n+3/2} = \boldsymbol{Y}^{n+1/2}, \quad \text{and} \quad (\rho\boldsymbol{u})_0^{n+1} = (\rho\boldsymbol{u})^n, \qquad (2.16)$$

where the subscript indicates the index of the sub-iteration. The Adams-Bashforth prediction is used for the initial density evaluation,

$$\rho_0^{n+3/2} = 2\rho^{n+1/2} - \rho^{n-1/2}. \qquad (2.17)$$

This ensures that the continuity equation is discretely satisfied at the beginning of the iterative procedure. The vector of chemical source terms is denoted by $\boldsymbol{\Omega} = (\dot{\omega}_1, ..., \dot{\omega}_N)$, and $\boldsymbol{\Omega}_0^{n+3/2}$ is evaluated using the thermochemical quantities obtained at the conclusion of the previous time step (explicit prediction).

For the sub-iteration $k = 1, ..., Q$

1.  The scalar fields are advanced in time using the semi-implicit Crank-Nicolson method [23, 80]

for the convective and diffusive terms, and explicit integration for the chemical source terms,

$$\boldsymbol{Y}_k^* = \frac{\boldsymbol{Y}^{n+1/2} + \boldsymbol{Y}_k^{n+3/2}}{2}, \tag{2.18}$$

$$\rho_k^{n+3/2}\boldsymbol{Y}_{k+1}^{n+3/2} = \rho^{n+1/2}\boldsymbol{Y}^{n+1/2} + \Delta t \left[\left(\boldsymbol{C}_k^{n+1} + \boldsymbol{D}_k^{n+1}\right) \cdot \boldsymbol{Y}_k^* + \boldsymbol{\Omega}_k^*\right]$$
$$+ \frac{\Delta t}{2}\left(\frac{\partial \boldsymbol{C}}{\partial \boldsymbol{Y}} + \frac{\partial \boldsymbol{D}}{\partial \boldsymbol{Y}}\right)_k^{n+1} \cdot \left(\boldsymbol{Y}_{k+1}^{n+3/2} - \boldsymbol{Y}_k^{n+3/2}\right). \tag{2.19}$$

To simplify the discrete notations for spatial differential operators, the operators corresponding to the convective and diffusive terms in the species transport equation (Eq. 2.4) are written as $\boldsymbol{C}$ and $\boldsymbol{D}$, respectively. $\partial \boldsymbol{C}/\partial \boldsymbol{Y}$ and $\partial \boldsymbol{D}/\partial \boldsymbol{Y}$ are the Jacobian matrices corresponding to the convective and diffusive terms, respectively. $\boldsymbol{C}$ and $\partial \boldsymbol{C}/\partial \boldsymbol{Y}$ are functions of the density and velocity, while $\boldsymbol{D}$ and $\partial \boldsymbol{D}/\partial \boldsymbol{Y}$ are functions of the density and the kinematic viscosity. They are consistently updated at each subiteration. Depending on the order of discretization, these operators are generally banded diagonal matrices (*e.g.* tridiagonal for second-order discretization and pentadiagonal for third-order discretization). It is important to note that the semi-implicit Crank-Nicolson method proposed by Pierce [80] is not applied to the time-integration of the species chemical source terms, $\boldsymbol{\Omega}_k^*$. This is due to the extremely high computational cost associated with the calculation of the chemical Jacobian matrix, $(\partial \boldsymbol{\Omega}/\partial \boldsymbol{Y})_K^{n+1}$ , and the even more expensive inversion of this matrix.

The stiffness of chemically reacting flows is generally believed to be due to the stiff source terms in the species transport equations, but not due to the temperature transport equation [34, 63, 54]. An estimate for the temperature time scale in an $n$-$C_7H_{16}$ /air premixed flame (used in the DNS described in chapter 4) gives $\tau_T \sim (T_b - T_u)/(\dot{\omega}/(\rho c_p))_{\max} \sim 10^4 s$, where $T_b$ and $T_u$ are the burnt and the unburnt temperatures, respectively. This time scale is approximately an order of magnitude larger than the time step corresponding to a unity convective CFL in such a laminar flame. Therefore, the temperature equation (Eq. 2.5) is advanced in time in the exact same fashion as the species mass fractions (Eqs. 2.18 and 2.19) without any further implicit treatment. The discretized temperature equation is not shown for clarity.

2. The density field is predicted from thermodynamics using

$$\rho_{k+1}^{n+3/2} = \frac{P_0 \left( \sum_{i=1}^{N} \frac{Y_{i,k+1}^{n+3/2}}{W_i} \right)^{-1}}{RT_{k+1}^{n+3/2}}. \tag{2.20}$$

It is important to note that this density evaluation does not ensure conservation of the species densities, $\rho Y_i$, since no density rescaling, such as the one proposed by Shunn *et al.* [106], is used. However, upon convergence of the subiterations, this formulation is equivalent to the density treatment proposed by Shunn *et al.*

3. The momentum equation is advanced in time using a similar semi-implicit Crank-Nicolson method as for the scalar fields,

$$\boldsymbol{u}_k^* = \frac{\boldsymbol{u}^n + \boldsymbol{u}_k^{n+1}}{2}, \tag{2.21}$$

$$\frac{\rho^{n+1/2} + \rho_{k+1}^{n+3/2}}{2} \hat{\boldsymbol{u}}_{k+1}^{n+1} = \frac{\rho^{n-1/2} + \rho^{n+1/2}}{2} \boldsymbol{u}^n + \Delta t \left[ \left( \boldsymbol{C}_{u,k}^{n+1} + \boldsymbol{D}_{u,k}^{n+1} \right) \cdot \boldsymbol{u}_k^* + \nabla p_k^{n+3/2} \right]$$

$$+ \frac{\Delta t}{2} \left( \frac{\partial \boldsymbol{C}_u}{\partial \boldsymbol{u}} + \frac{\partial \boldsymbol{D}_u}{\partial \boldsymbol{u}} \right)_k^{n+1} \cdot \left( \hat{\boldsymbol{u}}_{k+1}^{n+1} - \boldsymbol{u}_k^{n+1} \right), \tag{2.22}$$

where $\boldsymbol{C}_u$ and $\boldsymbol{D}_u$ are discrete operators associated with the convective and the viscous terms, respectively. $\hat{\boldsymbol{u}}$ is the predicted velocity field used to compute the fluctuating hydrodynamic pressure (Step 4).

4. A Poisson equation is then solved for the fluctuating hydrodynamic pressure,

$$\nabla^2 \delta p_{k+1}^{n+3/2} = \frac{1}{\Delta t} \left[ \nabla \cdot \left( \frac{\rho^{n+1/2} + \rho_{k+1}^{n+3/2}}{2} \hat{\boldsymbol{u}}_{k+1}^{n+1} \right) + \frac{\rho_{k+1}^{n+3/2} - \rho^{n+1/2}}{\Delta t} \right]. \tag{2.23}$$

The Poisson equation is solved using the high-fidelity HYPRE package [23, 32]. The predicted velocity field is then updated through a projection step,

$$\boldsymbol{u}_{k+1}^{n+1} = \hat{\boldsymbol{u}}_{k+1}^{n+1} - \frac{2\Delta t}{\rho^{n+1/2} + \rho_{k+1}^{n+3/2}} \left( \nabla \delta p_k^{n+3/2} \right) \quad \text{and} \quad P_{k+1}^{n+3/2} = P_k^{n+3/2} + \delta p_{k+1}^{n+3/2}. \tag{2.24}$$

5. Upon convergence of the sub-iterations, the new solutions are updated,

$$\rho^{n+3/2} = \rho_Q^{n+3/2}, \quad P^{n+3/2} = P_Q^{n+3/2}, \quad \boldsymbol{Y}^{n+3/2} = \boldsymbol{Y}_Q^{n+3/2}, \quad \text{and} \quad \boldsymbol{u}^{n+1} = \boldsymbol{u}_Q^{n+1}, \quad (2.25)$$

It is important to note that the above formulation becomes equivalent to the fully-implicit Crank-Nicolson time-integration scheme upon convergence of the sub-iterations [80].

# Chapter 3

# Vortex-flame Interaction[1]

The interaction of a 2D vortex with an initially planar flame is investigated in this chapter as a simplified test case for premixed turbulent combustion. While not all aspects of three-dimensional (3D) premixed turbulent combustion are present, this test case is useful because it provides a simple framework for investigating the coupling of vorticity and the flame. It is specifically studied here to better understand how the flame alters the vortex through the terms in the vorticity transport equation and when these terms are important given the initial size and strength of the vortex. This is accomplished by investigating the limiting behaviors of the vortex based on the ratios $u_v/S_L$ and $l_v/l_F$. The results provide a foundation to understand how a flame interacts with vorticity in turbulent combustion.

The following section (section 3.1) presents an overview of the physical system and a description of the numerical configuration. In section 3.2, a theoretical analysis is performed using analytical techniques yielding leading-order solutions of the vortex and flame. The numerical and theoretical results are compared in section 3.3 to characterize the different limiting behaviors and the impact of the relevant transport terms. Lastly, in section 3.4, the conclusions presented here are compared with the results of previous studies.

---

[1]This chapter is based in large part on the following conference proceedings: Bobbitt, B., Blanquart, G., Investigation of Vortex-Premixed Flame Interaction with Detailed Chemistry, Proceedings of 8th US Combustion Meeting, Salt Lake City, Utah (2013); Bobbitt, B., Blanquart, G., Approximate Solutions of the Transformation of Vortices through a Premixed Flame using Generalized Expansions, Proceedings of Western States Section/Combustion Institute, Fort Collins, Colorado (2013)

## 3.1   Problem setup

In this section, the physical and numerical configuration of the vortex-flame simulations are discussed.

### 3.1.1   Physical setup

This study considers a two-dimensional vortex initially in front of a planar premixed flame, as shown in Fig. 3.1. A monopole vortex is chosen over a dipole because a dipole may be thought of as two monopoles and has the added effect of a self-induced convective velocity. Therefore, a monopole is simpler and more general. The monopole vortex employed is the two-dimensional Taylor vortex. The Taylor vortex has the advantage of having an analytical solution to the momentum equation and a velocity that quickly decays in space, which in turn allows for a smaller computational domain. The required size of the domain for numerical convergence is addressed in appendix A.1. The equation for the vortex is given by

$$u_\theta(r, t) = u_{\theta,max} \frac{r}{r_a} e^{\left[\frac{1}{2}\left(1 - \left(\frac{r}{r_a}\right)^2\right)\right]}, \tag{3.1}$$

where $u_{\theta,max}$ is the maximum tangential velocity, and $r_a$ is the vortex core radius defined as the location of maximum tangential velocity. The vortex core radius is a funciton of time and equal to $r_a = \sqrt{2\nu t}$. The radial profiles of the velocity, vorticity, and pressure are displayed in Fig. 3.2 normalized by the maximum velocity, the maximum vorticity, and $\rho u_{\theta,max}^2$, respectively. The pressure profile is calculated for a steady vortex. The 2D domain is periodic in the $y$ direction with an inflow and outflow at the left and right $x$ boundaries, respectively. The flame moves from right to left, but is stabilized by an inflow at the left boundary approximately equal to the laminar flame speed.

For this study, the vortex characteristic length scale is defined as twice the vortex core diameter, $l_v \equiv 4r_a$, and the vortex characteristic velocity scale is defined as the maximum velocity, $u_v \equiv u_{\theta,max}$. This length scale encompasses the region where the vortex velocity is above half its maximum. While other velocity scales such as the vortex core average velocity or average velocity over $l_v$ could be
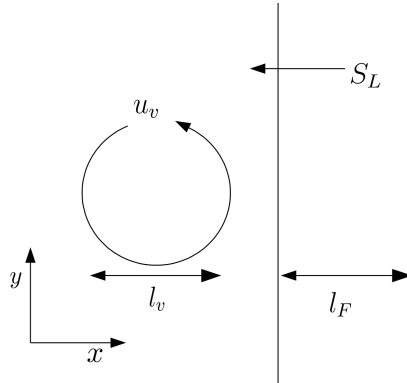
Figure 3.1: Diagram of the initial conditions and the definition of scales.

used, $u_{\theta,max}$ is preferred, as it provides easy comparison with other studies.

The reactants are that of hydrogen-air with an initial temperature of 298K and pressure of 1 atm. The equivalence ratio is equal to unity ($\phi = 1$), so that there is no limiting reactant. This fuel is chosen because hydrogen-air chemistry closely resembles a one-step reaction, removing the added effects of particular fuel chemistry. Additionally, hydrogen-air flames may be modeled using a small number of species and reactions compared to other larger hydrocarbon fuels, reducing the computational cost of simulations that use finite-rate chemistry. The chemistry is modeled by the detailed mechanism of Davis *et al.* [22], with all the species involving carbon atoms and their related reactions removed. Unity Lewis number transport is employed as the vortex-flame test case is not used to focus on the specific effects of differential diffusion. The specific impact of the transport model on vorticity in premixed turbulent combustion will be addressed in chapters 5 and 6 as the purpose of this chapter is to provide a qualitative framework for understanding the mechanisms by which the flame impacts vorticity.

The simulation is initialized with a planar flame near the center of the domain whose structure is acquired through interpolation of a one-dimensional flame solution. This one-dimensional flame solution is taken from a steadily propagating flame with the same numerical setup. The initial vortex velocity profile is added to the velocity field ahead of the flame. The separation between the vortex and flame is sufficient such that early aspects of the interaction are retained. The distance between the vortex center and where the flame temperature equals 450K is set to $3.5\,r_a$. This temperature
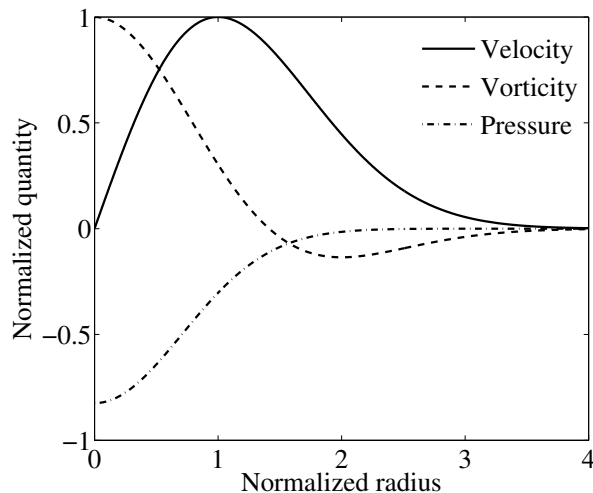
Figure 3.2: Radial profiles of the Taylor vortex with the normalized radius being $r/r_a$.

is reduced to T = 350K for the simulations with the smallest vortices tested. At $3.5\,r_a$, the vortex velocity is 1% of its maximum.

## 3.1.2 Simulations

The vortex and flame are each characterized by a length and velocity scale, providing the velocity and length scale ratios $u_v/S_L$ and $l_v/l_F$, respectively. Simulation test conditions are varied over a wide range of $u_v/S_L$ and $l_v/l_F$ so that the limiting cases based on these parameters may be probed. Specifically, the velocity ratio is varied between 0.1 to 50 and the length scale ratio is varied between 0.2 to 10. Figure 3.3 graphically displays the various initial conditions, which are also listed in table A.1 located in appendix A.3. Starting at the top left of Fig. 3.3 and going down then across, tests are referred to as run A, B, C, D, and E. Additional parameters may affect the vortex-flame interaction, such as particularities of fuel chemistry and the impact of gravity, but determining their effects are not within the scope of the current work.

The vortex-flame interaction possesses various time scales, each with a different physical significance. The length and velocity of the flame and vortex provide three important time scales,

$$\tau_1 = \frac{l_v}{u_v}, \quad \tau_2 = \frac{l_F}{S_L}, \quad \tau_3 = \frac{l_v}{S_L}. \tag{3.2}$$
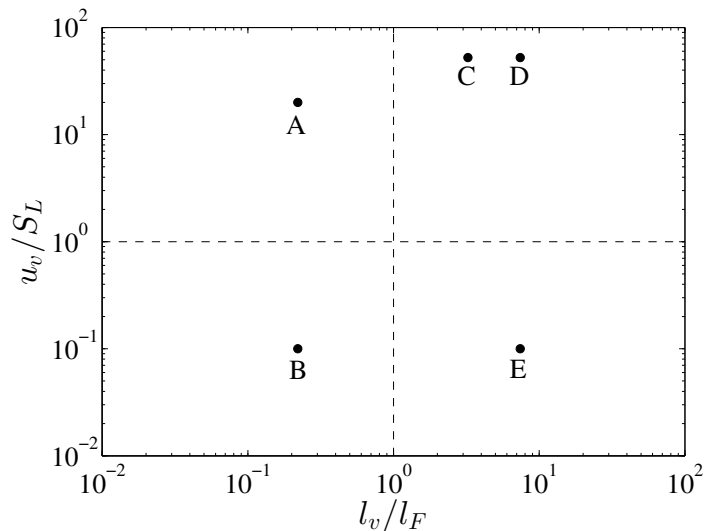
Figure 3.3: Graphical test matrix of simulations used for the analysis in section 3.3.

The first, $\tau_1$, is the time for one rotation of the vortex. The second, $\tau_2$, is often referred to as the chemical time scale. It characterizes the time for the flame to move the length of its own thickness and, consequently, for a infinitely small vortex to pass through the flame. The third, $\tau_3$, is the time for the flame to move the length of the vortex. When considering diffusion of momentum with the kinematic viscosity $\nu$, there is an additional relevant time scale, namely

$$\tau_4 = \frac{l_v^2}{\nu}. \tag{3.3}$$

This is the vortex diffusion time, and is related to the time for the vortex to decay. Indeed, the vortex core radius for the Taylor vortex (Eq. 3.1) is $r_a = \sqrt{2\nu t}$, so that the diffusion time scales as $r_a^2/(2\nu)$.

Various non-dimensional parameters may be constructed from these time scales. For example, the Damköhler number is the ratio of $\tau_1$ to $\tau_2$, and the vortex Reynolds number is the ratio of $\tau_4$ to $\tau_1$:

$$Da_v = \frac{\tau_1}{\tau_2}, \quad Re_v = \frac{\tau_4}{\tau_1}. \tag{3.4}$$

The vortex Damköhler number increases moving down and to the right in Fig. 3.3, so that run A

has the lowest value of $Da_v$. The vortex Reynolds number increases moving up and to the right in Fig. 3.3.

One other important non-dimensional parameters is the ratio of $\tau_2$, to $\tau_4$,

$$\frac{\tau_2}{\tau_4} = \frac{1}{a}\left(\frac{l_F}{l_v}\right)^2, \tag{3.5}$$

where $a$ is defined as $a \equiv l_F S_L/\nu$. This is the ratio of the time for a small vortex to pass through the flame versus the time for a vortex to diffuse. In the limit that this ratio is large, a small vortex will diffuse before passing through or even interacting with the flame. Therefore, in the limit of a small vortex, diffusion is expected to dominate the vortex-flame interaction. This behavior will be further discussed in section 3.3. In order to study how the flame alters vortices through dilatation and baroclinic torque, runs A and B are performed with a reduced value of the physical viscosity. In this way, all runs represent high Reynolds number behavior where viscous effects are small over the time of the interaction. The value of the viscosity is chosen so that the ratio of the viscous time scale to the time over which the vortex-flame interaction occurs is held constant between runs A and D. To accomplish this, $\mu$ is reduced by about a factor of 150 in runs A and B. The resulting initial vortex Reynolds numbers are listed in table A.1 located in appendix A.3.

In order to study the case where viscous effects dominate, runs A and B are performed a second time with the unaltered physical viscosity. These will be referred to as runs $A^v$ and $B^v$ and will be discussed in section 3.3.

### 3.1.3 Computational domain

The computational domain has a uniform mesh occupying the central third, which is surrounded by a stretched mesh in all directions. The central region is intended to resolve accurately the vortex and the perturbed flame while the stretched mesh provides for a larger domain size at a reduced computational cost. The maximum stretch ratio between grid points is 1.1. An example of the domain and initial conditions is displayed in Fig. 3.4.
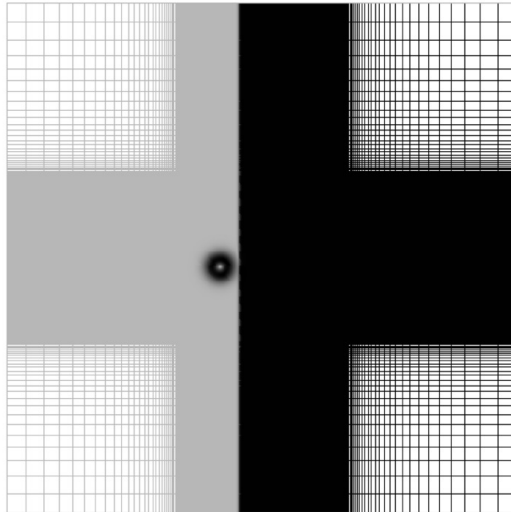
Figure 3.4: Shaded plot of velocity illustrating the grid and initial conditions of the vortex and planar flame.

| Parameter | Requirement |
|---|---|
| $n_F$: Number of points across $l_F$ | $\geq 55$ |
| $n_v$: Number of points across $l_v$ | $\geq 180$ |
| $L_y$: Length of domain in y-direction | $\geq 16\,l_v$ |
| $L_x$: Length of domain behind flame | $\geq 3\,l_F$ ; $9\,l_v$ |
| $\Delta t$: Time step | $\leq 2 \times 10^{-8}$s |

Table 3.1: Numerical requirements to resolve the relevant physics.

Efforts are taken to ensure the simulations capture all the relevant physics and are free of numerical resolution errors. Towards this goal, convergence studies are performed on a one-dimensional flame, an isolated decaying vortex, and run C. The determined resolution requirements are expressed as five criteria, namely, the number of points across the flame, $n_F$, the number of points across the vortex, $n_v$, the length of the domain in the y-direction, $L_y$, the length of the domain behind the flame, $L_x$, and the time step, $\Delta t$. A summary of these variables and their values is located in table 3.1. A detailed description of how these constraints are chosen is located in appendix A.1. As the central uniform mesh contains the vortex and perturbed flame, the requirements for $n_F$ and $n_v$ are placed on the grid in this region, while $L_y$ and $L_x$ are satisfied using the stretched mesh.

## 3.2   Theoretical analysis

Before presenting the results of the numerical simulations, it is insightful to perform a theoretical analysis to investigate the limiting behaviors of the vortex-flame interaction based on the ratios $u_v/S_L$ and $l_v/l_F$. Through this analysis, the important terms in the vorticity transport equation may be determined and the resulting impact on the vortex may be characterized either quantitatively or qualitatively in these limiting cases.

### 3.2.1   Methodology overview

This analysis seeks the leading-order solution of the vortex and flame based on the velocity and length scale ratios through generalized expansions. Using this method, higher-order equations may be derived, potentially providing further detail and insight. The theoretical analysis proceeds separately for $u_v/S_L \ll 1$, a slow vortex, and $u_v/S_L \gg 1$, a fast vortex. Each of these are further separated for $l_v/l_F \ll 1$, a small vortex and $l_v/l_F \gg 1$, a large vortex.

The present theoretical analysis considers the continuity and momentum equations (Eq. 2.2 and 2.3), as well as the vorticity and progress variable transport equations (Eq, 1.8 and 2.13). To simplify the analysis, the transport equation for the vorticity divided by density is used:

$$\rho^3 \left( \frac{\partial \omega^*}{\partial t} + \boldsymbol{u} \cdot \nabla \omega^* \right) = \nabla \rho \times \nabla P + \rho^2 \nabla \times \left( \frac{1}{\rho} \nabla \cdot \tau \right), \tag{3.6}$$

where $\omega^* = \omega/\rho$. The vorticity equation expressed using $\omega/\rho$ is derived in a similar form by Saffman [96]. Written as such, the effects of dilatation on vorticity are accounted for in the material derivative of $\omega^*$. As this problem is restricted to two-dimensions, vorticity is present only in the direction out of plane and is considered a scalar. As a result, the production/vortex stretching term is not present in Eq. 3.6 since it represents inherently three-dimensional phenomenon and is exactly equal to zero in this configuration. The present theoretical analysis assumes constant values of $\mu$, $\lambda$, and $c_P$. As used in Peters [79], the species diffusivity is equated to $S_L$ times $l_F$. To better understand the influence of the flame through dilatation and baroclinic torque, the effects of viscous

$$
\begin{array}{lcl}
\rho = \rho_F(x) & \rightarrow & \rho = \rho_u \overline{\rho}_F\left(\frac{x}{l_F}\right) \\
u = u_F(x) + u_{vort}(x,y) & \rightarrow & u = S_L \overline{u}_F\left(\frac{x}{l_F}\right) + u_v \overline{u}_{vort}\left(\frac{x}{l_v}, \frac{y}{l_v}\right) \\
v = v_{vort}(x,y) & \rightarrow & v = u_v \overline{v}_{vort}\left(\frac{x}{l_v}, \frac{y}{l_v}\right) \\
P = P_F(x) + P_{vort}(x,y) & \rightarrow & P = \rho_u S_L^2 \overline{P}_F\left(\frac{x}{l_F}\right) + \rho_u u_v^2 \overline{P}_{vort}\left(\frac{x}{l_v}, \frac{y}{l_v}\right) \\
\omega^* = \omega^*_{vort}(x,y) & \rightarrow & \omega^* = \frac{u_v}{\rho_u l_v} \overline{\omega}^*_{vort}\left(\frac{x}{l_v}, \frac{y}{l_v}\right) \\
c = c_F(x) & \rightarrow & c = c_b \overline{c}_F\left(\frac{x}{l_F}\right)
\end{array}
$$

Table 3.2: Initial conditions.

diffusion are not included in the following analysis. Viscous effects were addressed in section 3.1.2 by considering the relevant time scales and will be further discussed in section 3.3.3.

Modeling the chemistry using a detailed chemical mechanism requires an additional transport equation for each species, making this model inconducive to theoretical analysis. Tabulated chemistry, as presented in section 2.2.2, is more tractable while containing the physics necessary to investigate the effects of the flame on a vortex (simulation results support the use of this model, with additional details provided in appendix A.2). By use of the progress variable, $c$, species mass fractions and temperature are written as $Y_i = Y_i(c)$ and $T = T(c)$. As the low Mach number Navier-Stokes equations are solved, the density is related to the progress variable, here, through the function $\rho = g(c)$. The progress variable chemical source term has the form $\dot{\omega} = f(c)$, where $f$ is a continuous function.

The physical system solved in this theoretical analysis is the same as for the numerical simulations, namely a monopole vortex in front of a planar, laminar premixed flame, as shown in Fig. 3.1. The left boundary condition is an inflow condition equal to the laminar flame speed, so that an undisturbed flame remains fixed in space.

The initial conditions for the purpose of the theoretical analysis are listed in table 3.2. The vortex and flame are initially sufficiently separated so that the initial conditions are merely the sum of the two, noted by subscripts of *vort* or $F$. The initial conditions are then normalized so that each is equal to a constant times a variable with a magnitude of order one. These initial variables, signified by an over-line, are constructed so that their coordinates are divided by the physical length scale of the corresponding vortex or flame.

| $\tilde{\rho} =$ | $\overline{\rho}_F(\tilde{x})$ | $+$ | $0$ | $+$ | $0$ |
|---|---|---|---|---|---|
| $\tilde{u} =$ | $\overline{u}_F(\tilde{x})$ | $+$ | $\frac{u_v}{S_L}\overline{u}_{vort}(\frac{l_F}{l_v}\tilde{x}, \frac{l_F}{l_v}\tilde{y})$ | $+$ | $0$ |
| $\tilde{v} =$ | $0$ | $+$ | $\frac{u_v}{S_L}\overline{v}_{vort}(\frac{l_F}{l_v}\tilde{x}, \frac{l_F}{l_v}\tilde{y})$ | $+$ | $0$ |
| $\tilde{P} =$ | $\overline{P}_F(\tilde{x})$ | $+$ | $0$ | $+$ | $\left(\frac{u_v}{S_L}\right)^2 \overline{P}_{vort}(\frac{l_F}{l_v}\tilde{x}, \frac{l_F}{l_v}\tilde{y})$ |
| $\tilde{\omega}^* =$ | $0$ | $+$ | $\frac{u_v}{S_L}\frac{l_F}{l_v}\overline{\omega}^*_{vort}(\frac{l_F}{l_v}\tilde{x}, \frac{l_F}{l_v}\tilde{y})$ | $+$ | $0$ |
| $\tilde{c} =$ | $\overline{c}_F(\tilde{x})$ | $+$ | $0$ | $+$ | $0$ |

Table 3.3: Normalized initial conditions for a slow vortex, $u_v/S_L \ll 1$, separated into columns based on the order of $\epsilon$ ($u_v/S_L = \epsilon$).

## 3.2.2 Slow vortex

Equations are first derived for a slow vortex, $u_v/S_L \ll 1$, and then solutions are found individually for small, $l_v/l_F \ll 1$, and large, $l_v/l_F \gg 1$, vortices. The governing equations and initial conditions are normalized by the velocity of the flame, $S_L$, flame thickness, $l_F$, unburnt density, $\rho_u$, and the progress variable for the burnt conditions, $c_b$. As $S_L$ is larger than $u_v$, this normalization supports taking an expansion where $u_v/S_L$ is a small parameter, and is partially inspired by that of Matalon and Matkowsky [66]. Normalized variables are represented with a tilde: $u = S_L\tilde{u}$, $v = S_L\tilde{v}$, $\rho = \rho_u\tilde{\rho}$, $P = \rho_u S_L^2 \tilde{P}$, $\omega^* = S_L/(l_F\rho_u)\tilde{\omega}^*$, and $c = c_b\tilde{c}$. The progress variable chemical source term is normalized as such: $\dot{\omega} = (S_L\rho_u c_b/l_F)\tilde{\dot{\omega}}$. The normalized initial conditions are listed in table 3.3.

Taking $\epsilon$ to be a small parameter, a solution is sought of the form of a generalized expansion in $\epsilon$ (Eq. 3.7). In the limit of a slow vortex, the velocity scale ratio is defined as $u_v/S_L = \epsilon$,

$$
\left.
\begin{aligned}
\tilde{\rho} &= \tilde{\rho}_o + \epsilon\tilde{\rho}_1 + ..., \\
\tilde{u} &= \tilde{u}_o + \epsilon\tilde{u}_1 + ..., \\
\tilde{v} &= \tilde{v}_o + \epsilon\tilde{v}_1 + ..., \\
\tilde{P} &= \tilde{P}_o + \epsilon\tilde{P}_1 + ..., \\
\tilde{\omega}^* &= \tilde{\omega}^*_o + \epsilon\tilde{\omega}^*_1 + ..., \\
\tilde{c} &= \tilde{c}_o + \epsilon\tilde{c}_1 + ....
\end{aligned}
\right\}
\tag{3.7}
$$

After inserting the above expressions into the governing equations, terms are separated based on powers of $\epsilon$, with $\epsilon^0$ as zeroth-order, $\epsilon^1$ as first-order, and so forth.

### 3.2.2.1  Zeroth-order equations

The zeroth-order equations are given in Cartesian coordinates by

$$\frac{\partial \tilde{\rho}_o}{\partial \tilde{t}} + \tilde{u}_o \frac{\partial \tilde{\rho}_o}{\partial \tilde{x}} + \tilde{v}_o \frac{\partial \tilde{\rho}_o}{\partial \tilde{y}} = - \tilde{\rho}_o \left( \frac{\partial \tilde{u}_o}{\partial \tilde{x}} + \frac{\partial \tilde{v}_o}{\partial \tilde{y}} \right), \tag{3.8}$$

$$\tilde{\rho}_o \left( \frac{\partial \tilde{u}_o}{\partial \tilde{t}} + \tilde{u}_o \frac{\partial \tilde{u}_o}{\partial \tilde{x}} + \tilde{v}_o \frac{\partial \tilde{u}_o}{\partial \tilde{y}} \right) = - \frac{\partial \tilde{P}_o}{\partial \tilde{x}}, \tag{3.9}$$

$$\tilde{\rho}_o \left( \frac{\partial \tilde{v}_o}{\partial \tilde{t}} + \tilde{u}_o \frac{\partial \tilde{v}_o}{\partial \tilde{x}} + \tilde{v}_o \frac{\partial \tilde{v}_o}{\partial \tilde{y}} \right) = - \frac{\partial \tilde{P}_o}{\partial \tilde{y}}, \tag{3.10}$$

$$\tilde{\rho}_o^3 \left( \frac{\partial \tilde{\omega}_o^*}{\partial \tilde{t}} + \tilde{u}_o \frac{\partial \tilde{\omega}_o^*}{\partial \tilde{x}} + \tilde{v}_o \frac{\partial \tilde{\omega}_o^*}{\partial \tilde{y}} \right) = \frac{\partial \tilde{\rho}_o}{\partial \tilde{x}} \frac{\partial \tilde{P}_o}{\partial \tilde{y}} - \frac{\partial \tilde{\rho}_o}{\partial \tilde{y}} \frac{\partial \tilde{P}_o}{\partial \tilde{x}}, \tag{3.11}$$

$$\tilde{\rho}_o \left( \frac{\partial \tilde{c}_o}{\partial \tilde{t}} + \tilde{u}_o \frac{\partial \tilde{c}_o}{\partial \tilde{x}} + \tilde{v}_o \frac{\partial \tilde{c}_o}{\partial \tilde{y}} \right) = \left( \frac{\partial}{\partial \tilde{x}} \left( \tilde{\rho}_o \frac{\partial \tilde{c}_o}{\partial \tilde{x}} \right) + \frac{\partial}{\partial \tilde{y}} \left( \tilde{\rho}_o \frac{\partial \tilde{c}_o}{\partial \tilde{y}} \right) \right) + \tilde{\dot{\omega}}_o, \tag{3.12}$$

$$\tilde{\rho}_o = \tilde{g}(c_b \tilde{c}_o), \tag{3.13}$$

with the corresponding initial conditions provided in table 3.3. The progress variable chemical source terms is $\tilde{\dot{\omega}}_o = \tilde{f}(c_b \tilde{c}_o)$. The zeroth-order equations are the same Navier-Stokes and progress variable transport equations, but for the zeroth-order quantities only. The initial conditions correspond to an unperturbed, planar, laminar flame. By this, and including the inflow condition, the solution of the zeroth-order system of equations is a steady planar flame. The solution may be written as: $\tilde{\rho}_o = \overline{\rho}_F$, $\tilde{u}_o = \overline{u}_F$, $\tilde{v}_o = 0$, $\tilde{P}_o = \overline{P}_F$, $\tilde{\omega}_o^* = 0$, and $\tilde{c}_o = \overline{c}_F$. This is the leading-order solution for the flame and, interestingly, is uncoupled from the vortex for this case. This result is valid for both small and large vortices.

### 3.2.2.2 First-order equations

The first-order terms are listed in Eq. 3.14 - 3.19 after applying the solution of the zeroth-order quantities,

$$\left( \frac{\partial \tilde{\rho}_1}{\partial \tilde{t}} + \overline{u}_F \frac{\partial \tilde{\rho}_1}{\partial \tilde{x}} \right) + \tilde{u}_1 \frac{\partial \overline{\rho}_F}{\partial \tilde{x}} = -\tilde{\rho}_1 \frac{\partial \overline{u}_F}{\partial \tilde{x}} - \overline{\rho}_F \left( \frac{\partial \tilde{u}_1}{\partial \tilde{x}} + \frac{\partial \tilde{v}_1}{\partial \tilde{y}} \right), \tag{3.14}$$

$$\overline{\rho}_F \left( \frac{\partial \tilde{u}_1}{\partial \tilde{t}} + \overline{u}_F \frac{\partial \tilde{u}_1}{\partial \tilde{x}} \right) + \tilde{\rho}_1 \overline{u}_F \frac{\partial \overline{u}_F}{\partial \tilde{x}} + \overline{\rho}_F \tilde{u}_1 \frac{\partial \overline{u}_F}{\partial \tilde{x}} = -\frac{\partial \tilde{P}_1}{\partial \tilde{x}}, \tag{3.15}$$

$$\overline{\rho}_F \left( \frac{\partial \tilde{v}_1}{\partial \tilde{t}} + \overline{u}_F \frac{\partial \tilde{v}_1}{\partial x} \right) = -\frac{\partial \tilde{P}_1}{\partial \tilde{y}}, \tag{3.16}$$

$$\overline{\rho}_F^3 \left( \frac{\partial \tilde{\omega}_1^*}{\partial \tilde{t}} + \overline{u}_F \frac{\partial \tilde{\omega}_1^*}{\partial \tilde{x}} \right) = \frac{\partial \overline{\rho}_F}{\partial \tilde{x}} \frac{\partial \tilde{P}_1}{\partial \tilde{y}} - \frac{\partial \tilde{\rho}_1}{\partial \tilde{y}} \frac{\partial \overline{P}_F}{\partial \tilde{x}}, \tag{3.17}$$

$$\overline{\rho}_F \left( \frac{\partial \tilde{c}_1}{\partial \tilde{t}} + \overline{u}_F \frac{\partial \tilde{c}_1}{\partial \tilde{x}} \right) + \tilde{\rho}_1 \overline{u}_F \frac{\partial \overline{c}_F}{\partial \tilde{x}} + \overline{\rho}_F \tilde{u}_1 \frac{\partial \overline{c}_F}{\partial \tilde{x}} = \frac{\partial \tilde{\rho}_1}{\partial \tilde{x}} \frac{\partial \overline{c}_F}{\partial \tilde{x}} + \tilde{\rho}_1 \frac{\partial^2 \overline{c}_F}{\partial \tilde{x}^2} + \frac{\partial \overline{\rho}_F}{\partial \tilde{x}} \frac{\partial \tilde{c}_1}{\partial \tilde{x}} +$$

$$\overline{\rho}_F \left( \frac{\partial^2 \tilde{c}_1}{\partial \tilde{x}^2} + \frac{\partial^2 \tilde{c}_1}{\partial \tilde{y}^2} \right) + \tilde{\omega}_1, \tag{3.18}$$

$$\tilde{\rho}_1 = c_b \tilde{c}_1 \tilde{g}'(c_b \tilde{c}_o), \tag{3.19}$$

and the corresponding initial conditions are also provided in table 3.3. Here, the chemical source term is $\dot{\omega}_1 = c_b \tilde{c}_1 f'(c_b \tilde{c}_o)$. This system of equations corresponds to the leading-order solution of the perturbed vortex and perturbed flame. These equations are not the Navier-Stokes equations, but actually a set of equations linear in the first-order quantities. The analysis will continue separately based upon the size of the vortex.

### 3.2.2.3 Slow and small vortex

As the zeroth-order solution is a planar flame, its associated vorticity is zero. For a small vortex, its initial vorticity is relatively large, as seen by $l_F/l_v$ in the initial condition. It is therefore more appropriate to rewrite the vorticity as $\phi_1 = l_v/l_F \tilde{\omega}_1^*$. This only alters the vorticity equation,

$$\overline{\rho}_F^3 \left( \frac{\partial \phi_1}{\partial \tilde{t}} + \overline{u}_F \frac{\partial \phi_1}{\partial \tilde{x}} \right) = \frac{l_v}{l_F} \left( \frac{\partial \overline{\rho}_F}{\partial \tilde{x}} \frac{\partial \tilde{P}_1}{\partial \tilde{y}} - \frac{\partial \tilde{\rho}_1}{\partial \tilde{y}} \frac{\partial \overline{P}_F}{\partial \tilde{x}} \right), \tag{3.20}$$

and initial condition,

$$\phi_1(\tilde{x}, \tilde{y}, \tilde{t} = 0) = \overline{\omega}^*_{vort}\left(\frac{l_F}{l_v}\tilde{x}, \frac{l_F}{l_v}\tilde{y}\right). \tag{3.21}$$

Including this as the vorticity equation, a second generalized expansion is performed in $\xi$ on the first-order equations, taking $\xi = l_v/l_F$. A solution of the form of Eq. 3.22 is sought,

$$\tilde{\rho}_1 = \tilde{\rho}_{1,o} + \xi\tilde{\rho}_{1,1} + ..., \tag{3.22}$$

for $\tilde{\rho}_1$ and analogously for the remaining variables. After inserting these expressions into Eq. 3.14 - 3.19, terms are separated based on powers of $\xi$ in the same manner as before. For the sake of brevity, only the resulting leading-order vorticity equation is written, which is as follows:

$$\frac{\partial \phi_{1,o}}{\partial \tilde{t}} + \overline{u}_F \frac{\partial \phi_{1,o}}{\partial \tilde{x}} = 0, \tag{3.23}$$

along with the corresponding initial condition,

$$\phi_{1,o}(\tilde{x}, \tilde{y}, \tilde{t} = 0) = \overline{\omega}^*_{vort}\left(\frac{l_F}{l_v}\tilde{x}, \frac{l_F}{l_v}\tilde{y}\right). \tag{3.24}$$

It is important to recall that dilatation is accounted for in the left hand side of Eq. 3.23. This equation may be solved explicitly as it is uncoupled from the rest of the system. It is an advection equation; the vorticity of the vortex is merely advected by the flame velocity, $\overline{u}_F$. The solution is given by

$$\omega_{1,o}(\tilde{x}, \tilde{y}, \tilde{t}) = \frac{\overline{\rho}_F(\tilde{x})}{\overline{\rho}_F(\tilde{x}_o)}\omega_{vort}(\tilde{x}_o, \tilde{y}), \tag{3.25}$$

where the value of $\tilde{x}_o$ is solved through the Lagrangian equation $\int_{\tilde{x}_o}^{\tilde{x}(\tilde{t})} 1/\overline{u}_F(x')dx' = \tilde{t}$. This provides the relation between the initial location, $x_o$, the current location, $x$, and time. As $\overline{u}_F$ increases with $x$, this results in the vortex lengthening in the flame normal direction. In this solution, the circulation is of the vortex is conserved.

Equation 3.25 is the leading-order solution for the transformation of a vortex across the flame in

the limit that $u_v/S_L \ll 1$ and $l_v/l_F \ll 1$. In this limit, the vortex is dampened with the ratio of the local to initial density and stretched in the normal direction to the flame by the inverse of the same ratio due to the effects of dilatation.

### 3.2.2.4  Slow and large vortex

Starting from Eq. 3.14 - 3.19, a generalized expansion is taken again in $\xi$, here equated as $\xi = l_F/l_v$. Similar to before, a solution of the form below is sought,

$$\tilde{\rho}_1 = \tilde{\rho}_{1,o} + \xi\tilde{\rho}_{1,1} + ..., \tag{3.26}$$

for $\tilde{\rho}_1$ and analogously for the remaining variables. After inserting the above expressions into Eq. 3.14 - 3.19, terms are separated based on powers of $\xi$. Again, only the resulting leading-order vorticity equation is written, which is given by

$$\frac{\partial \tilde{\omega}^*_{1,o}}{\partial \tilde{t}} + \overline{u}_F \frac{\partial \tilde{\omega}^*_{1,o}}{\partial \tilde{x}} = \frac{1}{\overline{\rho}_F^3} \left( \frac{\partial \overline{\rho}_F}{\partial \tilde{x}} \frac{\partial \tilde{P}_{1,o}}{\partial \tilde{y}} - \frac{\partial \tilde{\rho}_{1,o}}{\partial \tilde{y}} \frac{\partial \overline{P}_F}{\partial \tilde{x}} \right), \tag{3.27}$$

along with the initial condition,

$$\tilde{\omega}^*_{1,o}(\tilde{x}, \tilde{y}, \tilde{t} = 0) = 0. \tag{3.28}$$

The resulting system of equations contains the leading-order solution of a slow and large vortex and the perturbation to the flame. The leading-order vorticity equation is different from the small vortex in that the terms of baroclinic torque, $(\nabla\rho \times \nabla P)$, are retained and the vorticity initial condition is zero (the initial condition $\overline{\omega}^*_{vort}$ has been pushed to higher-orders in $\xi$). Equation 3.27 is coupled to the other equations in the system, and though an analytical solution is not derived, a qualitative description is possible. The baroclinic torque is non-zero and the corresponding production of vorticity is significantly larger than the initial vorticity of the vortex. Combined with the leading-order solution for the flame, the behavior in the limit of a large and slow vortex is predicted as a planar flame with minor perturbations and a significantly altered vortex through the

action of baroclinic torque.

### 3.2.3 Fast vortex

In the limit of a fast vortex, $u_v/S_L \gg 1$, a similar analysis could be performed as above. If this is done, the equations and initial conditions are normalized once again, this time using $u_v$ in place of $S_L$. A solution of the form of a generalized expansion, Eq. 3.7, is sought with $\zeta = S_L/u_v$ being the small parameter, and terms of the governing equations are separated based on powers of $\zeta$. The zeroth-order equations in two-dimensional Cartesian coordinates are given by

$$\frac{\partial \tilde{\rho}_o}{\partial \tilde{t}} + \tilde{u}_o \frac{\partial \tilde{\rho}_o}{\partial \tilde{x}} + \tilde{v}_o \frac{\partial \tilde{\rho}_o}{\partial \tilde{y}} = -\tilde{\rho}_o \left( \frac{\partial \tilde{u}_o}{\partial \tilde{x}} + \frac{\partial \tilde{v}_o}{\partial \tilde{y}} \right), \tag{3.29}$$

$$\tilde{\rho}_o \left( \frac{\partial \tilde{u}_o}{\partial \tilde{t}} + \tilde{u}_o \frac{\partial \tilde{u}_o}{\partial \tilde{x}} + \tilde{v}_o \frac{\partial \tilde{u}_o}{\partial \tilde{y}} \right) = -\frac{\partial \tilde{P}_o}{\partial \tilde{x}}, \tag{3.30}$$

$$\tilde{\rho}_o \left( \frac{\partial \tilde{v}_o}{\partial \tilde{t}} + \tilde{u}_o \frac{\partial \tilde{v}_o}{\partial \tilde{x}} + \tilde{v}_o \frac{\partial \tilde{v}_o}{\partial \tilde{y}} \right) = -\frac{\partial \tilde{P}_o}{\partial \tilde{y}}, \tag{3.31}$$

$$\tilde{\rho}_o^3 \left( \frac{\partial \tilde{\omega}_o^*}{\partial \tilde{t}} + \tilde{u}_o \frac{\partial \tilde{\omega}_o^*}{\partial \tilde{x}} + \tilde{v}_o \frac{\partial \tilde{\omega}_o^*}{\partial \tilde{y}} \right) = \left( \frac{\partial \tilde{\rho}_o}{\partial \tilde{x}} \frac{\partial \tilde{P}_o}{\partial \tilde{y}} - \frac{\partial \tilde{\rho}_o}{\partial \tilde{y}} \frac{\partial \tilde{P}_o}{\partial \tilde{x}} \right), \tag{3.32}$$

$$\tilde{\rho}_o \left( \frac{\partial \tilde{c}_o}{\partial \tilde{t}} + \tilde{u}_o \frac{\partial \tilde{c}_o}{\partial \tilde{x}} + \tilde{v}_o \frac{\partial \tilde{c}_o}{\partial \tilde{y}} \right) = 0, \tag{3.33}$$

$$\tilde{\rho}_o = \tilde{g}(c_b \tilde{c}_o), \tag{3.34}$$

along with the initial conditions

$$\left. \begin{aligned} &\tilde{\rho}_o(\tilde{x}, \tilde{y}, \tilde{t} = 0) = \overline{\rho}_F(\tilde{x}), \\ &\tilde{u}_o(\tilde{x}, \tilde{y}, \tilde{t} = 0) = \overline{u}_{vort}(\tfrac{l_F}{l_v}\tilde{x}, \tfrac{l_F}{l_v}\tilde{y}), \\ &\tilde{v}_o(\tilde{x}, \tilde{y}, \tilde{t} = 0) = \overline{v}_{vort}(\tfrac{l_F}{l_v}\tilde{x}, \tfrac{l_F}{l_v}\tilde{y}), \\ &\tilde{P}_o(\tilde{x}, \tilde{y}, \tilde{t} = 0) = \overline{P}_{vort}(\tfrac{l_F}{l_v}\tilde{x}, \tfrac{l_F}{l_v}\tilde{y}), \\ &\tilde{\omega}_o^*(\tilde{x}, \tilde{y}, \tilde{t} = 0) = \tfrac{l_F}{l_v}\overline{\omega}_{vort}^*(\tfrac{l_F}{l_v}\tilde{x}, \tfrac{l_F}{l_v}\tilde{y}), \\ &\tilde{c}_o(\tilde{x}, \tilde{y}, \tilde{t} = 0) = \overline{c}_F(\tilde{x}). \end{aligned} \right\} \tag{3.35}$$

Unfortunately, both the vortex and flame quantities are represented in the initial conditions,

suggesting that, to a larger extent, the behaviors of the vortex and the flame are intrinsically coupled. For this reason, a different approach is used in order to obtain an analytical solution for the case of a small and fast vortex.

### 3.2.3.1 Fast and small vortex

In the limit of a fast, $u_v/S_L \gg 1$, and small, $l_v/l_F \ll 1$, vortex, the equations are derived in a different manner and the analysis involves two separate stages.

First, the behavior of the flame evolution is investigated. As done for the slow and small vortex (section 3.2.2.3), the governing equations are normalized by $S_L$, $l_F$, $\rho_u$, and $c_b$. It is important to note that the coordinate system is centered on the initial vortex. A generalized expansion is performed, taking $\xi$ to be a small parameter such that $\xi = l_v/l_F$, and seeking a solution of the following form,

$$\tilde{\rho}_o = \tilde{\rho}_o + \xi \tilde{\rho}_1 + ..., \tag{3.36}$$

for each of the variables. After separating the terms based on powers of $\xi$, the zeroth-order equations written in Cartesian coordinates are as follows,

$$\frac{\partial \tilde{\rho}_o}{\partial \tilde{t}} + \tilde{u}_o \frac{\partial \tilde{\rho}_o}{\partial \tilde{x}} + \tilde{v}_o \frac{\partial \tilde{\rho}_o}{\partial \tilde{y}} = -\tilde{\rho}_o \left( \frac{\partial \tilde{u}_o}{\partial \tilde{x}} + \frac{\partial \tilde{v}_o}{\partial \tilde{y}} \right), \tag{3.37}$$

$$\tilde{\rho}_o \left( \frac{\partial \tilde{u}_o}{\partial \tilde{t}} + \tilde{u}_o \frac{\partial \tilde{u}_o}{\partial \tilde{x}} + \tilde{v}_o \frac{\partial \tilde{u}_o}{\partial \tilde{y}} \right) = -\frac{\partial \tilde{P}_o}{\partial \tilde{x}}, \tag{3.38}$$

$$\tilde{\rho}_o \left( \frac{\partial \tilde{v}_o}{\partial \tilde{t}} + \tilde{u}_o \frac{\partial \tilde{v}_o}{\partial \tilde{x}} + \tilde{v}_o \frac{\partial \tilde{v}_o}{\partial \tilde{y}} \right) = -\frac{\partial \tilde{P}_o}{\partial \tilde{y}}, \tag{3.39}$$

$$\tilde{\rho}_o \left( \frac{\partial \tilde{c}_o}{\partial \tilde{t}} + \tilde{u}_o \frac{\partial \tilde{c}_o}{\partial \tilde{x}} + \tilde{v}_o \frac{\partial \tilde{c}_o}{\partial \tilde{y}} \right) = \frac{\partial}{\partial \tilde{x}} \left( \tilde{\rho}_o \frac{\partial \tilde{c}_o}{\partial \tilde{x}} \right) + \frac{\partial}{\partial \tilde{y}} \left( \tilde{\rho}_o \frac{\partial \tilde{c}_o}{\partial \tilde{y}} \right) + \tilde{\omega}_o, \tag{3.40}$$

$$\tilde{\rho}_o = \tilde{g}(c_b \tilde{c}_o), \tag{3.41}$$

with the initial conditions,

$$
\left.\begin{aligned}
\tilde{\rho}_o(\tilde{x}, \tilde{y}, \tilde{t}=0) &= \overline{\rho}_F(\tilde{x}), \\
\tilde{u}_o(\tilde{x}, \tilde{y}, \tilde{t}=0) &= \overline{u}_F(\tilde{x}) + \tfrac{u_v}{S_L}\overline{u}_{vort}(\xi^{-1}\tilde{x}, \xi^{-1}\tilde{y}), \\
\tilde{v}_o(\tilde{x}, \tilde{y}, \tilde{t}=0) &= \tfrac{u_v}{S_L}\overline{v}_{vort}(\xi^{-1}\tilde{x}, \xi^{-1}\tilde{y}), \\
\tilde{P}_o(\tilde{x}, \tilde{y}, \tilde{t}=0) &= \overline{P}_F(\tilde{x}) + \left(\tfrac{u_v}{S_L}\right)^2 \overline{P}_{vort}(\xi^{-1}\tilde{x}, \xi^{-1}\tilde{y}), \\
\tilde{c}_o(\tilde{x}, \tilde{y}, \tilde{t}=0) &= \overline{c}_F(\tilde{x}).
\end{aligned}\right\}
\tag{3.42}
$$

This zeroth-order system represents the solution as $\xi$ approaches zero ($\xi = l_v/l_F \to 0$). As the coordinates of the vortex initial conditions are multiplied by $\xi^{-1}$, this limit creates a "jump condition:" if $\tilde{x} > 0$, then $\xi^{-1}\tilde{x} \to \infty$ and if $\tilde{x} < 0$, then $\xi^{-1}\tilde{x} \to -\infty$. Both correspond to locations far away from the vortex where its initial conditions equal zero. Only at $\tilde{x}, \tilde{y} = 0$ are the initial conditions for the vortex non-zero.

In these equations the vortex may be considered as infinitely thin and provides a jump discontinuity, though no variables have jumps in their values. By this, it is concluded that the initially planar flame is perturbed only at a single *point* and the progress variable, $c_o$, does not vary over the area of the vortex. Taking this limit, the initial conditions then become

$$
\left.\begin{aligned}
\tilde{\rho}_o(\tilde{x}, \tilde{y}, \tilde{t}=0) &= \overline{\rho}_F(\tilde{x}), \\
\tilde{u}_o(\tilde{x}, \tilde{y}, \tilde{t}=0) &= \overline{u}_F(\tilde{x}), \\
\tilde{v}_o(\tilde{x}, \tilde{y}, \tilde{t}=0) &= 0, \\
\tilde{P}_o(\tilde{x}, \tilde{y}, \tilde{t}=0) &= \overline{P}_F(\tilde{x}), \\
\tilde{c}_o(\tilde{x}, \tilde{y}, \tilde{t}=0) &= \overline{c}_F(\tilde{x}).
\end{aligned}\right\}
\tag{3.43}
$$

Once again, these initial conditions and the associated equations (Eq. 3.37-3.41) correspond to that of a one-dimensional planar flame. In summary, this zeroth-order solution for a small vortex is a planar unperturbed flame.

In this second stage, and in order to gain insight into the transformation of the vortex through the flame, the governing equations are normalized instead by $u_v$, $l_v$, $\rho_u$, and $c_b$. It is important to

remember that the coordinate system is centered on the initial vortex. Using the above results, the progress variable is assumed constant in space over the area of the vortex, changing in time from the unburnt to burnt quantities, $\tilde{c} = \tilde{c}(t)$, as the vortex passes through the flame. Expanding again in $\xi = l_v / l_F$, the zeroth-order equations become as follows,

$$\frac{\partial \tilde{\rho}_o}{\partial \tilde{t}} + \tilde{u}_o \frac{\partial \tilde{\rho}_o}{\partial \tilde{x}} + \tilde{v}_o \frac{\partial \tilde{\rho}_o}{\partial \tilde{y}} = -\tilde{\rho}_o \left( \frac{\partial \tilde{u}_o}{\partial \tilde{x}} + \frac{\partial \tilde{v}_o}{\partial \tilde{y}} \right), \tag{3.44}$$

$$\tilde{\rho}_o \left( \frac{\partial \tilde{u}_o}{\partial \tilde{t}} + \tilde{u}_o \frac{\partial \tilde{u}_o}{\partial \tilde{x}} + \tilde{v}_o \frac{\partial \tilde{u}_o}{\partial \tilde{y}} \right) = -\frac{\partial \tilde{P}_o}{\partial \tilde{x}}, \tag{3.45}$$

$$\tilde{\rho}_o \left( \frac{\partial \tilde{v}_o}{\partial \tilde{t}} + \tilde{u}_o \frac{\partial \tilde{v}_o}{\partial \tilde{x}} + \tilde{v}_o \frac{\partial \tilde{v}_o}{\partial \tilde{y}} \right) = -\frac{\partial \tilde{P}_o}{\partial \tilde{y}}, \tag{3.46}$$

$$\tilde{\rho}_o^3 \left( \frac{\partial \tilde{\omega}_o^*}{\partial \tilde{t}} + \tilde{u}_o \frac{\partial \tilde{\omega}_o^*}{\partial \tilde{x}} + \tilde{v}_o \frac{\partial \tilde{\omega}_o^*}{\partial \tilde{y}} \right) = \left( \frac{\partial \tilde{\rho}_o}{\partial \tilde{x}} \frac{\partial \tilde{P}_o}{\partial \tilde{y}} - \frac{\partial \tilde{\rho}_o}{\partial \tilde{y}} \frac{\partial \tilde{P}_o}{\partial \tilde{x}} \right), \tag{3.47}$$

$$\tilde{\rho}_o = \tilde{g}(c_b \tilde{c}(t)), \tag{3.48}$$

with the initial conditions,

$$\left. \begin{array}{l} \tilde{\rho}_o(\tilde{x}, \tilde{y}, \tilde{t} = 0) = \overline{\rho}_F(0), \\[2mm] \tilde{u}_o(\tilde{x}, \tilde{y}, \tilde{t} = 0) = \frac{S_L}{u_v} \overline{u}_F(0) + \overline{u}_{vort}(\tilde{x}, \tilde{y}), \\[2mm] \tilde{v}_o(\tilde{x}, \tilde{y}, \tilde{t} = 0) = \overline{v}_{vort}(\tilde{x}, \tilde{y}), \\[2mm] \tilde{P}_o(\tilde{x}, \tilde{y}, \tilde{t} = 0) = \left( \frac{S_L}{u_v} \right)^2 \overline{P}_F(0) + \overline{P}_{vort}(\tilde{x}, \tilde{y}), \\[2mm] \tilde{\omega}_o^*(\tilde{x}, \tilde{y}, \tilde{t} = 0) = \overline{\omega}_{vort}^*(\tilde{x}, \tilde{y}). \end{array} \right\} \tag{3.49}$$

As a result of assuming $\tilde{c}$ is constant in space, $\tilde{\rho}_o$ is constant in space through 3.48, but again changes in time from the unburnt to burnt quantities. This is also reflected in the initial conditions. After applying this result, a second generalized expansion is performed in $\zeta$, taking $\zeta = S_L / u_v$, limiting the solution to a fast vortex. A solution of the form of Eq. 3.50 is sought,

$$\tilde{u}_o = \tilde{u}_{o,o} + \zeta \tilde{u}_{o,1} + ..., \tag{3.50}$$

for $\tilde{u}_o$ and similarly for the remaining variables. In the same manner as previously performed, terms

are separated based on powers of $\zeta$. The leading-order equations are as follows, written in cylindrical coordinates centered on the initial vortex,

$$\frac{\partial \tilde{\rho}_o}{\partial \tilde{t}} + \frac{\tilde{\rho}_o}{r}\left(\frac{\partial(\tilde{u}_{r;o,o}r)}{\partial \tilde{r}} + \frac{\partial \tilde{u}_{\theta;o,o}}{\partial \tilde{\theta}}\right) = 0, \tag{3.51}$$

$$\frac{\partial \tilde{u}_{r;o,o}}{\partial \tilde{t}} + \tilde{u}_{r;o,o}\frac{\partial \tilde{u}_{r;o,o}}{\partial \tilde{r}} + \frac{\tilde{u}_{\theta;o,o}}{r}\frac{\partial \tilde{u}_{r;o,o}}{\partial \tilde{\theta}} - \frac{\tilde{u}_{\theta;o,o}^2}{r} = -\frac{1}{\tilde{\rho}_o}\frac{\partial \tilde{P}_{o,o}}{\partial \tilde{r}}, \tag{3.52}$$

$$\frac{\partial \tilde{u}_{\theta;o,o}}{\partial \tilde{t}} + \tilde{u}_{r;o,o}\frac{\partial \tilde{u}_{\theta;o,o}}{\partial \tilde{r}} + \frac{\tilde{u}_{\theta;o,o}}{r}\frac{\partial \tilde{u}_{\theta;o,o}}{\partial \tilde{\theta}} + \frac{\tilde{u}_{\theta;o,o}\tilde{u}_{r;o,o}}{r} = -\frac{1}{\tilde{\rho}_o r}\frac{\partial \tilde{P}_{o,o}}{\partial \tilde{\theta}}, \tag{3.53}$$

$$\frac{\partial \tilde{\omega}_{o,o}}{\partial \tilde{t}} + \tilde{u}_{r;o,o}\frac{\partial \tilde{\omega}_{o,o}}{\partial \tilde{r}} + \frac{\tilde{u}_{\theta;o,o}}{r}\frac{\partial \tilde{\omega}_{o,o}}{\partial \tilde{\theta}} = 0, \tag{3.54}$$

with the initial conditions,

$$\left.\begin{aligned} \tilde{u}_{r;o,o}(\tilde{r},\theta,\tilde{t}=0) &= 0, \\ \tilde{u}_{\theta;o,o}(\tilde{r},\theta,\tilde{t}=0) &= \overline{u}_{vort}(\tilde{r}), \\ \tilde{P}_{o,o}(\tilde{r},\theta,\tilde{t}=0) &= \overline{P}_{vort}(\tilde{r}), \\ \tilde{\omega}_{o,o}^*(\tilde{r},\theta,\tilde{t}=0) &= \overline{\omega}_{vort}^*(\tilde{r}). \end{aligned}\right\} \tag{3.55}$$

Note that in these equations the vortex center does not move in time as the flame velocity does not appear here. As the initial conditions and $\tilde{\rho}_o$ have no $\theta$ dependence, there is no dependence on $\theta$ through time. Therefore, the vorticity and velocity remain axisymmetric, providing for the reduction of the continuity and vorticity equations into their final simplified form.

$$\frac{r}{\tilde{\rho}_o}\frac{\partial \tilde{\rho}_o}{\partial \tilde{t}} + \frac{\partial(\tilde{u}_{r;o,o}r)}{\partial \tilde{r}} = 0, \tag{3.56}$$

$$\frac{\partial \tilde{\omega}_{o,o}}{\partial \tilde{t}} + \tilde{u}_{r;o,o}\frac{\partial \tilde{\omega}_{o,o}}{\partial \tilde{r}} = 0. \tag{3.57}$$

The radial velocity, $\tilde{u}_{r,o,o}$, induced by the density change is solved and substituted into the vorticity equation. Like the case of a slow, small vortex, this is again an advection equation, but here the vorticity is advected radially. The solution is given by

$$\tilde{\omega}_{o,o}(\tilde{r},\tilde{t}) = \frac{\tilde{\rho}_o(t)}{\overline{\rho}_F}\overline{\omega}_{vort}\left(\tilde{r}\sqrt{\frac{\tilde{\rho}_o(t)}{\overline{\rho}_F}}\right). \tag{3.58}$$

The density in Eq. 3.58 is evaluated at the vortex. This is the solution for the leading-order transformation the vortex across the flame in the limit of a fast and small vortex, $u_v/S_L \gg 1$ and $l_v/l_F \ll 1$. In this solution, the vortex is dampened by the local to initial density ratio and expanded radially by the square root of the same ratio due to the effects of dilatation. The circulation of the vortex is conserved. This solution is very similar to the slow, small vortex, but the vortex expands radially rather than normal to the flame front.

### 3.2.3.2  Fast and large vortex

For the case of a fast $(u_v/S_L \gg 1)$ and large $(l_v/l_F \gg 1)$ vortex, the analysis begins with the zeroth-order equations in $\zeta$, Eq. 3.29 - 3.34. These are further expanded in $\xi$, equating $\xi = l_F/l_v$. The leading-order continuity and vorticity equations are given by,

$$\frac{\partial \tilde{\rho}_{o,o}}{\partial \tilde{t}} + \tilde{u}_{o,o}\frac{\partial \tilde{\rho}_{o,o}}{\partial \tilde{x}} + \tilde{v}_{o,o}\frac{\partial \tilde{\rho}_{o,o}}{\partial \tilde{y}} = -\tilde{\rho}_{o,o}\left(\frac{\partial \tilde{u}_{o,o}}{\partial \tilde{x}} + \frac{\partial \tilde{v}_{o,o}}{\partial \tilde{y}}\right), \tag{3.59}$$

$$\tilde{\rho}_{o,o}^3\left(\frac{\partial \tilde{\omega}_{o,o}^*}{\partial \tilde{t}} + \tilde{u}_{o,o}\frac{\partial \tilde{\omega}_{o,o}^*}{\partial \tilde{x}} + \tilde{v}_{o,o}\frac{\partial \tilde{\omega}_{o,o}^*}{\partial \tilde{y}}\right) = \left(\frac{\partial \tilde{\rho}_{o,o}}{\partial \tilde{x}}\frac{\partial \tilde{P}_{o,o}}{\partial \tilde{y}} - \frac{\partial \tilde{\rho}_{o,o}}{\partial \tilde{y}}\frac{\partial \tilde{P}_{o,o}}{\partial \tilde{x}}\right), \tag{3.60}$$

along with the initial conditions,

$$\left.\begin{aligned}
\tilde{\rho}_{o,o}(\tilde{x}, \tilde{y}, \tilde{t}=0) &= \overline{\rho}_F(\tilde{x}), \\
\tilde{u}_{o,o}(\tilde{x}, \tilde{y}, \tilde{t}=0) &= \overline{u}_{vort}(\tfrac{l_F}{l_v}\tilde{x}, \tfrac{l_F}{l_v}\tilde{y}), \\
\tilde{v}_{o,o}(\tilde{x}, \tilde{y}, \tilde{t}=0) &= \overline{v}_{vort}(\tfrac{l_F}{l_v}\tilde{x}, \tfrac{l_F}{l_v}\tilde{y}), \\
\tilde{P}_{o,o}(\tilde{x}, \tilde{y}, \tilde{t}=0) &= \overline{P}_{vort}(\tfrac{l_F}{l_v}\tilde{x}, \tfrac{l_F}{l_v}\tilde{y}), \\
\tilde{\omega}_{o,o}^*(\tilde{x}, \tilde{y}, \tilde{t}=0) &= 0, \\
\tilde{c}_{o,o}(\tilde{x}, \tilde{y}, \tilde{t}=0) &= \overline{c}_F(\tilde{x}).
\end{aligned}\right\} \tag{3.61}$$

These equations are the leading-order solution for the vortex and flame. The presence of both vortex and flame quantities in the initial conditions suggests their strong intrinsic coupling. Like the case of the slow and large vortex, the terms of baroclinic torque, $(\nabla\rho \times \nabla P)$, are retained and the initial condition of the vortex vorticity, $\overline{\omega}_{vort}^*$, has been pushed to higher-orders in $\xi$. However,
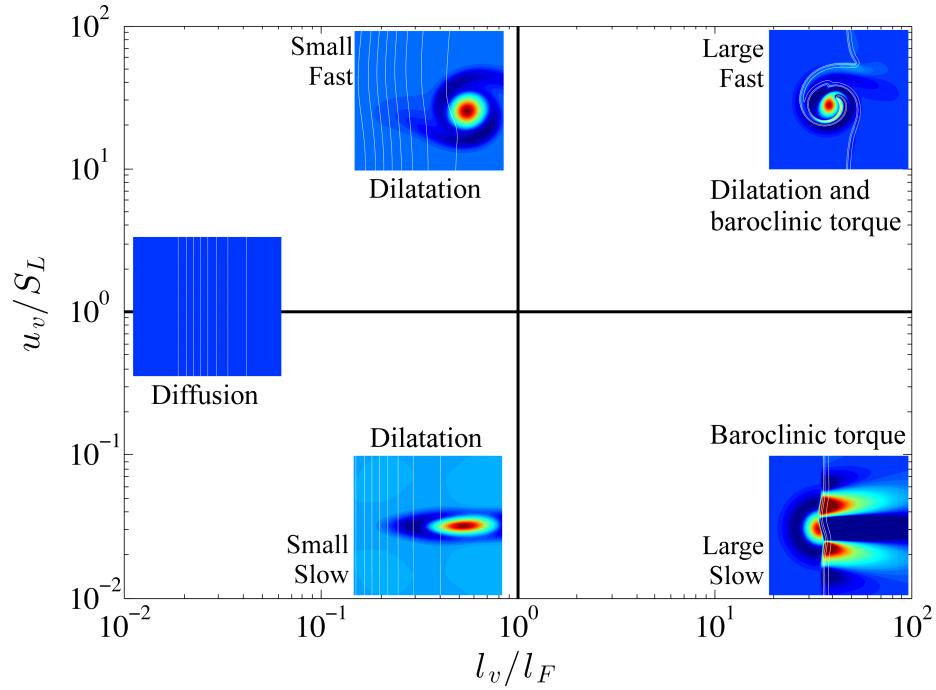
Figure 3.5: Graphical illustration of the limiting behaviors of the vortex-flame interaction and the corresponding dominant term(s) in the vorticity transport equation based on the ratios $u_v/S_L$ and $l_v/l_F$.

there is no zeroth-order solution of an unperturbed flame. Again, a qualitative solution is provided of vorticity production through baroclinic torque which significantly alters the vortex. In summary, the behavior in the limit that $u_v/S_L \gg 1$ and $l_v/l_F \gg 1$ is predicted here as a significantly altered flame and vortex.

## 3.3   Numerical results

In this section, the different limiting behaviors of vorticity transformation found in the theoretical analysis are compared to the numerical results. The results are summarized graphically in Fig. 3.5. The dominant terms and the impact on vorticity are subsequently described based on the initial size and strength of the vortex.

### 3.3.1 Slow vortices

For relatively slow vortices, $u_v/S_L \ll 1$, the time for the flame front to pass over the vortex, $\tau_3$, is much smaller than the time for the vortex to make one rotation, $\tau_1$. As a result, the relative distortion of the flame by the vortex is small. From the theoretical analysis, the leading-order solution is an unperturbed planar flame. Therefore, for all slow vortices, it may be expected that the flame is only slightly perturbed. Higher-order terms include perturbations to the planar flame as well as the perturbations to the vortex.

#### 3.3.1.1 Small and slow vortex

For a small, slow vortex ($u_v/S_L \ll 1$ and $l_v/l_F \ll 1$) when viscous effects do not dominate, the series of plots in Fig. 3.6 illustrates the behavior of this case, taken from simulation B. In this limit, vortices transform as a function of the density ratio, and are too small and too weak to generate any significant curvature of the flame.

The vortex is initially circular (Fig. 3.6a) but is stretched normal to the flame and dampened (*i.e.* its maximum vorticity decreases) (Fig. 3.6b) The magnitude of the stretching and dampening increases as it passes through the flame. During the interaction, the flame remains planar and the density and temperature fields remain largely fixed (Fig. 3.6c). After passing through the flame, the vortex is greatly weakened and strongly stretched (Fig. 3.6e). At this stage, the vortex for run B is not identified as a vortex by the $\lambda_{ci}$ criterion [19]. This suggests that the vortex may be considered destroyed and transformed merely into a streak of vorticity.

The explanation for this behavior is as follows. The pressure and density gradients are controlled almost entirely by the leading-order solution, which is a planar flame. As such, they remain virtually fixed in space and occur over a distance much larger than the size of the vortex. Under these conditions, the interaction exhibits negligible amounts of baroclinic torque. As the velocity due to the flame is much larger than the vortex, the vorticity is merely advected and dilated through the flame, described by the leading-order solution of the vortex (Eq. 3.25). These results are summarized

$(a)$ 0.040ms $\quad$ $(b)$ 0.060ms $\quad$ $(c)$ 0.080ms $\quad$ $(d)$ 0.100ms $\quad$ $(e)$ 0.125ms
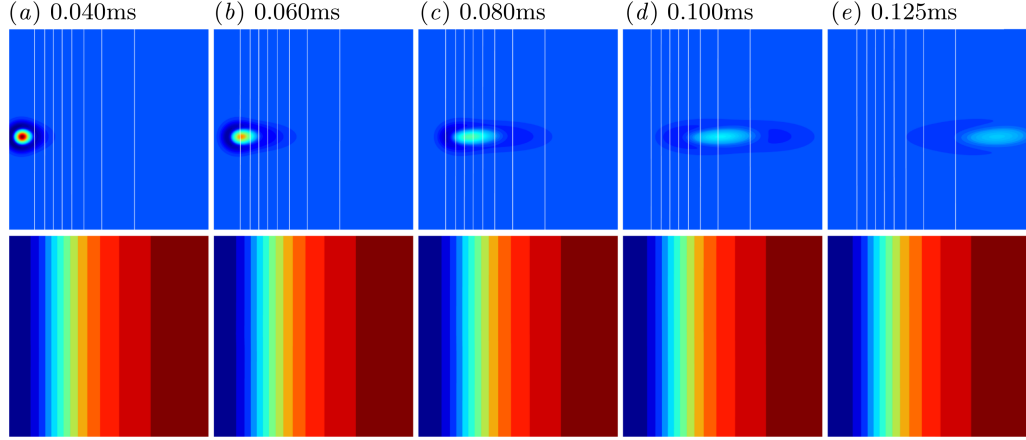


Figure 3.6: Results of run B, demonstrating the behavior of this limiting case. Top figures are shaded contours of vorticity with lines of constant temperature superimposed and bottom figures are shaded contours of temperature.

through the following relations describing the transformation of the vortex,

$$\text{Vorticity: } \frac{\omega_{max}(t)}{\omega_{max,o}} = \frac{\rho(t)}{\rho_o} \tag{3.62}$$

$$\text{Circulation: } \Gamma = \text{constant} \tag{3.63}$$

$$\text{Area: } \frac{A(t)}{A_o} = \frac{\rho_o}{\rho(t)} \tag{3.64}$$

$$\text{Radius: } \frac{r_x(t)}{r_{x,o}} = \frac{\rho_o}{\rho(t)} \tag{3.65}$$

$$\text{Minor Radius: } r_y(t) = \text{constant,} \tag{3.66}$$

where the naught subscript signifies the initial conditions. These are all derived from Eq. 3.25 and are all merely a function of the density ratio.

These relations are compared against the results of the simulation B in Fig. 3.7. There is excellent agreement for the maximum vorticity and vortex core radii. The differences are likely due to the effects of viscosity. In summary, the vortex stretches in the flame normal direction and its peak vorticity decreases proportional to the density ratio due to the effects of dilatation. The density ratio is of central importance, as it has a direct effect on the transformation of the vortex. The flame is negligibly perturbed.
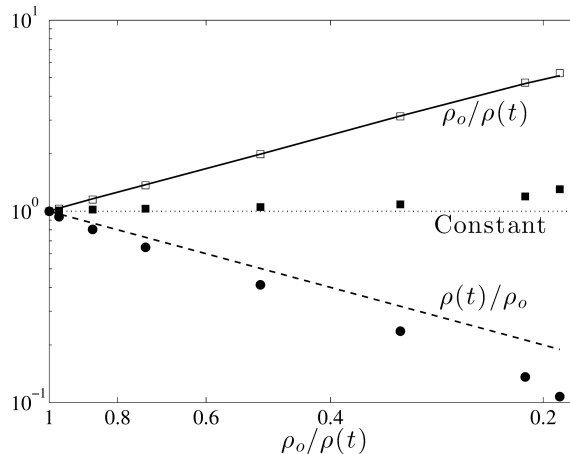
Figure 3.7: Results of run B compared against the theoretical relations of a small, slow vortex. $\square$ $r_x(t)/r_{x,o}$, $\blacksquare$ $r_y(t)/r_{y,o}$, $\bullet$ $\omega_{max}(t)/\omega_{max,o}$.

### 3.3.1.2  Large and slow vortex

For a large, slow vortex ($u_v/S_L \ll 1$ and $l_v/l_F \gg 1$), located in the bottom right corner of Fig. 3.5, the series of plots in Fig. 3.8 illustrates the behavior of the vortex-flame interaction. In this limit, the vortices are too weak to disrupt much of the planar symmetry of the flame but large enough to generate slight curvature.

The interaction begins as the incoming vortex perturbs the perfect planar symmetry of the flame. The vortex velocity into the flame pushes the flame back while the other side of the vortex pulls it forward, causing the flame to curve over the length of the vortex (Fig. 3.8b and c). This induced curvature results in the production of vorticity within the flame. This vorticity is then convected downstream (Fig. 3.8c). As the curvature increases, so does the vorticity produced, which eventually reaches a magnitude greater than that of the incoming vortex (Fig. 3.8d). At this point, the vortex is destroyed, leaving only streaks of positive and negative vorticity behind the flame (Fig. 3.8e).

This behavior is explained by the leading-order equation for the vortex (Eq. 3.27). As mentioned in section 3.2, the right hand size of this equation contains the terms of baroclinic torque. The baroclinic torque is predicted to alter significantly the incoming vortex because the initial conditions of the vortex vorticity are accounted for only in higher-order terms. In the numerical results, the vortex is indeed destroyed by vorticity produced through baroclinic torque in the flame. During the

$(a)$ 0.00ms     $(b)$ 0.60ms     $(c)$ 0.90ms     $(d)$ 1.20 ms     $(e)$ 1.40ms

Figure 3.8: Results of run E, demonstrating the limiting case of a large, slow vortex. Top figures are shaded contours of vorticity with lines of constant temperature superimposed and bottom figures are shaded contours of temperature.
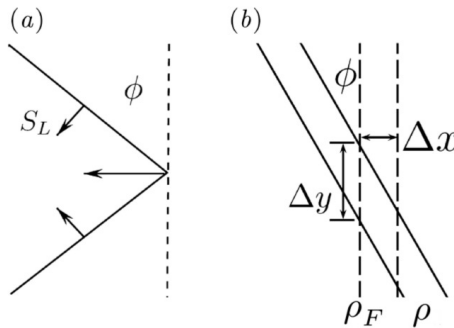


Figure 3.9: $(a)$ Diagram of a flame cusp and $(b)$ illustration of terms in Eq. 3.67.

interaction, the vortex perturbs the flame, possibly exciting the Darrieus-Landau instability, but this aspect and the possible production of vorticity by the flame after the interaction is beyond the scope of this work.

A simple model may be constructed to estimate the magnitude of the vorticity produced through baroclinic torque, $\omega_B$, relative to that of the incoming vortex. In this way, the conditions under which the initial vortex is destroyed may be predicted. A flame cusp (shown in Fig. 3.9a) is the point where two laminar flames intersect, and propagates at a rate of $S_L/\cos\phi$, with $\phi$ defined in Fig. 3.9a. Observing that a flame cusp occurs near the location of the vortex peak velocity into the flame, Fig. 3.8d, the angle $\phi$ is estimated as $\cos\phi = S_L/(u_v + S_L)$.

The baroclinic torque is modeled using the expression from the generalized expansion (Eq. 3.27). The gradients are evaluated as jumps across the flame, providing an equation for the magnitude of

vorticity produced,

$$\omega_B = \frac{\Delta t}{\rho_u^2} \left( \frac{\Delta \rho_F}{\Delta x} \frac{\Delta P_1}{\Delta y} - \frac{\Delta P_F}{\Delta x} \frac{\Delta \rho_1}{\Delta y} \right). \tag{3.67}$$

Each of these terms can be evaluated with respect to the flame cusp. Analogous to the theoretical solution, $\rho_F$ and $P_F$ are the flame initial conditions and $\rho_1$ and $P_1$ are deviations from a planar flame. It is observed in run E that the pressure field remains largely unchanged and therefore $P_1$ is taken to be zero and $\Delta P_F$ is estimated as $\rho_u S_L^2 - \rho_b (\rho_u/\rho_b S_L)^2$. As shown in Fig. 3.9b, the jump in $x$ is the flame thickness and $\Delta y = l_F/\sin\phi$. Integrating over the time to cross the flame, $\Delta t = \tau_2$, and using $\omega_{vort} = a\, u_v/l_v$ where from the Taylor vortex equation $a = 8e^{1/2}$, the resulting equation for the ratio of the vorticity magnitudes is given by

$$\left| \frac{\omega_{vort}}{\omega_B} \right| = \left[ \frac{u_v}{S_L} \frac{l_F}{l_v} \right] \frac{a\, \rho_u/\rho_b}{(\rho_u/\rho_b - 1)^2 \sqrt{1 - (S_L/(S_L + u_v))^2}}. \tag{3.68}$$

When this ratio is small, the vorticity produced by the flame is much greater than that of the vortex, which is then likely destroyed. A comparison with run E when the vortex is nearly centered on the flame shows qualitative agreement as the simulation and model give values of 0.32 and 0.10, respectively. This simple model provides a scaling relationship for a large, slow vortex, showing that the ratio $\omega_{vort}/\omega_B$ approaches zero if $u_v/S_L \to 0$ or $l_F/l_v \to 0$. This supports that indeed for all values satisfying $u_v/S_L \ll 1$ and $l_v/l_F \gg 1$, the vorticity produced by the flame dominates that of the incoming vortex. In summary, the numerical and theoretical results corroborate to support that in the limit of $u_v/S_L \ll 1$ and $l_v/l_F \gg 1$, the incoming vortex is destroyed by the production of vorticity through baroclinic torque.

### 3.3.2 Fast vortices

#### 3.3.2.1 Small and fast vortex

For a small, fast vortex ($u_v/S_L \gg 1$, $l_v/l_F \ll 1$) when viscous effects do not dominate, the series of plots in Fig. 3.10 illustrate the behavior. In this limit, vortices transform as a function of the density ratio while generating curvature in the flame over the vortex length.
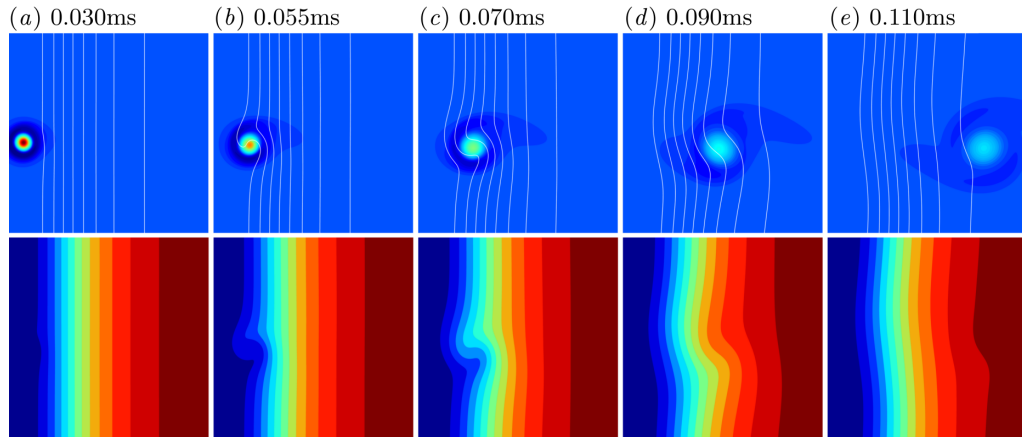
Figure 3.10: Results of run A, demonstrating the behavior of this limiting case. Top figures are shaded contours of vorticity with lines of constant temperature superimposed and bottom figures are shaded contours of temperature.

In this case, the vortex pulls consecutive layers of the flame around the exterior of the vortex (Fig. 3.10a - c). During this process, the flame experiences curvature only over the area of the vortex. In the limit of a small vortex, the temperature and density vary negligibly across the area of the vortex and little baroclinic torque is produced. As the interaction proceeds, the vortex grows in size and decreases in velocity (Fig. 3.10d). As a result of the decrease in velocity, the induced curvature of the flame also becomes less significant through the flame. The vortex survives passing through the flame, maintaining its original structure but expanding nearly uniformly in size and decreasing in strength (Fig. 3.10e).

The behavior of this case is understood through the leading-order solution for the vortex, derived in section 3.2 and listed in Eq. 3.58. In the limit of $l_v/l_F \ll 1$, the gradients due to the flame are small across the vortex, so that little baroclinic torque is produced. Due to the large velocity of the vortex, the velocity from the flame is negligible and the vortex expands radially. As the vortex expands, it loses strength, decreasing the velocity magnitude due to the effects of dilatation. The results are summarized through the following relations derived from Eq. 3.58 and, notably, are all
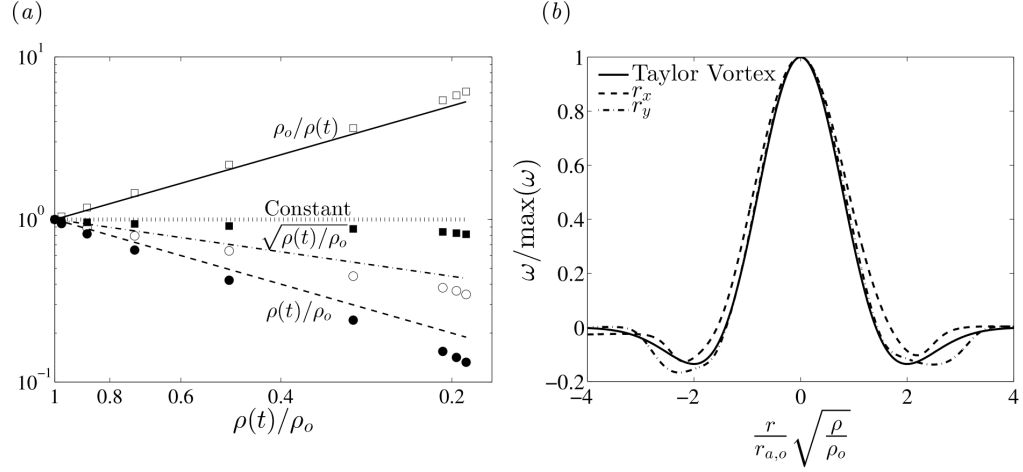
Figure 3.11: (a) Results of run A compared against the theoretical solution. □ $A(t)/A_o$, ■ $\Gamma(t)/\Gamma_o$, ○ $U_{max}(t)/U_{max,o}$, ● $\omega_{max}(t)/\omega_{max,o}$. (b) Run A final vortex vorticity in two directions compared to the initial profile rescaled according to Eq. 3.73$d$ and normalized to the same maximum vorticity.

a function of the density ratio,

$$\text{Vorticity:} \quad \frac{\omega_{max}(t)}{\omega_{max,o}} = \frac{\rho(t)}{\rho_o} \tag{3.69}$$

$$\text{Circulation:} \quad \Gamma = \text{constant} \tag{3.70}$$

$$\text{Area:} \quad \frac{A(t)}{A_o} = \frac{\rho_o}{\rho(t)} \tag{3.71}$$

$$\text{Radius:} \quad \frac{r_a(t)}{r_{a,o}} = \sqrt{\frac{\rho_o}{\rho(t)}} \tag{3.72}$$

$$\text{Velocity:} \quad \frac{U_{max}(t)}{U_{max,o}} = \sqrt{\frac{\rho(t)}{\rho_o}}, \tag{3.73}$$

where the naught subscript signifies the initial conditions.

The above theoretical relations are compared against the numerical results in Fig. 3.11a. The vortex core circulation, core area, peak velocity, and peak vorticity in the simulation show excellent agreement with the theoretical predictions throughout the flame thickness. Once again, differences may be attributed to viscous dissipation. In this limiting case, the vortex maintains its original structure. To demonstrate this, the final vortex vorticity profile is plotted against the initial profile rescaled according to Eq. 3.73 and normalized to the same maximum vorticity, as shown in Fig. 3.11b. The vortex in the numerical solution retains its structure well, again supporting the validity

of the relations in Eq. 3.69 - 3.73.

In summary, the numerical and theoretical results support that in the limit of a small and fast vortex when viscous effects do not dominate, the vortex expands radially while decreasing in strength. This is due to dilatation, and the changes in the vortex are only a function of the density ratio.

### 3.3.2.2  Large and fast vortex

For a fast and large vortex ($u_v/S_L \gg 1$, $l_v/l_F \gg 1$), the series of plots in Fig. 3.12 illustrate the vortex-flame interaction. In this limit, vortices are large enough to affect the entire flame thickness simultaneously and fast enough to break the planar symmetry.

In the initial stage of the interaction, a portion of the flame is pulled into the exterior of the vortex (Fig. 3.12a). The flame remains continuous and the out shoot is referred to here as a flame peninsula (Fig. 3.12b). The tip of the flame peninsula is referred to as the crown. The flame peninsula is further pulled by the vortex until it is wrapped potentially multiple times around the vortex (Fig. 3.12c), forming a continuous spiral separated by unburnt reactants. As the flame is wrapped, the flame crown moves towards the center of the vortex. The largest values of baroclinic torque are present in the flame crown, which acts like a wedge, breaking into the vortex and disrupting its original structure. At this stage, the competing time scales are evident as the vortex attempts to wrap the flame before the flame consumes the entire vortex area. Once the crown approaches the vortex core, the spiral structure and vortex break up, forming pockets of unburnt reactants and small regions of positive and negative vorticity (Fig. 3.12d). The interaction completes as these pockets are consumed and the individual regions of vorticity reform into a new vortex (Fig. 3.12e). As the vorticity passes through the flame, its magnitude decreases by the effects of dilatation. The size and velocity of the resulting vortex are significantly different from those of the initial vortex. Despite the complicated wrapping process and the significant role of baroclinic torque, in run C and D the characteristics of this new vortex are well approximated by the same relations derived for a small, fast vortex in the absence of viscous dissipation (Eq. 3.69 - 3.73).
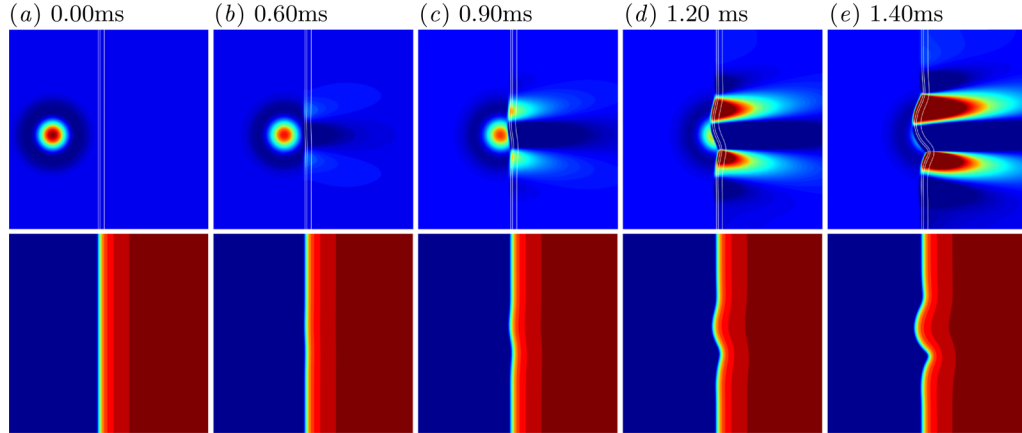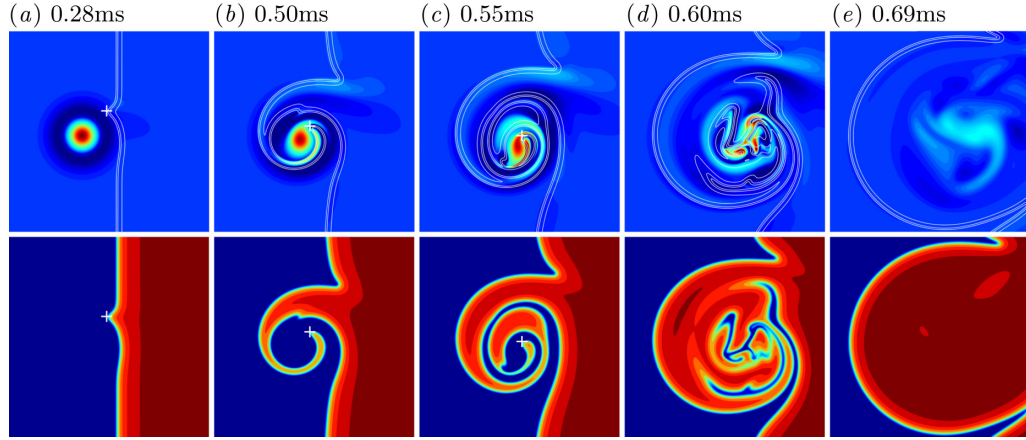
Figure 3.12: Results of run D demonstrating the limiting case of a large, fast vortex. Top figures are shaded contours of vorticity with lines of constant temperature superimposed and bottom figures are shaded contours of temperature. The cross indicates the location of the flame crown.
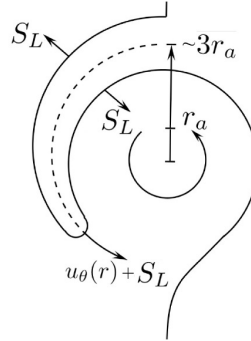


Figure 3.13: Schematic diagram of the flame behavior for a large, fast vortex.

The wrapping process and the peninsula are depicted in Fig. 3.13. It is observed in run D that the peninsula begins near $3r_a$. This figure shows that the flame propagates normal to itself while advected by the local vortex velocity. As a result, the flame crown moves towards radii of higher angular velocity, which, for a Taylor vortex, is towards the center of the vortex. This creates the spiral structure.

Additional important facets of this regime include flame curvature, baroclinic torque, and flame strain within the flame peninsula. As the peninsula is wrapped around the exterior of the vortex, the majority of the flame peninsula experiences curvature with a length scale of $l_v$. The flame crown, however, experiences curvature with a length scale of the flame thickness, $l_F$. The leading-order vorticity equation for this regime, Eq. 3.60, retains the terms of baroclinic torque, suggesting its importance. The simulations confirm that significant values of baroclinic torque are present in the

flame peninsula, with the largest values located in the flame crown where the flame curvature is largest. The vorticity produced through baroclinic torque in run D is of similar magnitude to that of the vortex, as shown in Fig. 3.12c. The entire peninsula predominantly experiences positive stretch. As the flame peninsula remains continuous in run D, the flame stretch was not large enough to cause local extinction.

The boundaries of this regime may be estimated by defining at least one full rotation of the flame peninsula as within this regime. It is observed in run D that the vortex breaks up as the flame reaches the core. Since the peninsula has a minimum thickness of $2l_F$, the smallest vortex within this regime is approximately $l_v/l_F = 6$. The minimum vortex velocity to exhibit this behavior is estimated through the following simple model.

The location of the flame front is modeled by each point propagating towards the center of the vortex with the speed $S_L$ while advected (tangential to the vortex) by the local vortex velocity, similar in concept to the G-equation [79]. Considering an initially planar flame and the Taylor vortex, each point on the flame front is given by

$$r(t) = r_o - S_L t, \tag{3.74}$$

$$\theta(t) = \frac{u_v}{S_L} \sqrt{\frac{e\pi}{2}} \left( \mathrm{erf}\left[ \frac{r_o}{\sqrt{2}r_a} \right] - \mathrm{erf}\left[ \frac{r(t)}{\sqrt{2}r_a} \right] \right) + \theta_o, \tag{3.75}$$

where $r$ is the distance from the center of the vortex, $\theta$ is the angle from the horizontal, $r_o$ is the initial distance from the vortex, $\theta_o$ is $\theta$ at $t = 0$, and erf is the error function. The slowest vortex to produce one full rotation of the flame peninsula before it reaches the vortex core ($\theta = 2\pi$), is approximately $u_v/S_L = 10$. Interestingly, the number of times the flame is wrapped around the vortex is linearly proportional to $u_v/S_L$.

To summarize, the vortex wraps the flame into a spiral structure and the curvature of the flame leads to vorticity production through baroclinic torque. This vorticity mixes with the initial vortex which is acted upon by dilatation. The original structure of the vortex is destroyed, leaving a vortex of different strength and size from the incoming vortex. While the vortex was observed to

$(a)$ 0.00ms $\quad$ $(b)$ 0.055ms $\quad$ $(c)$ 0.070ms $\quad$ $(d)$ 0.090ms
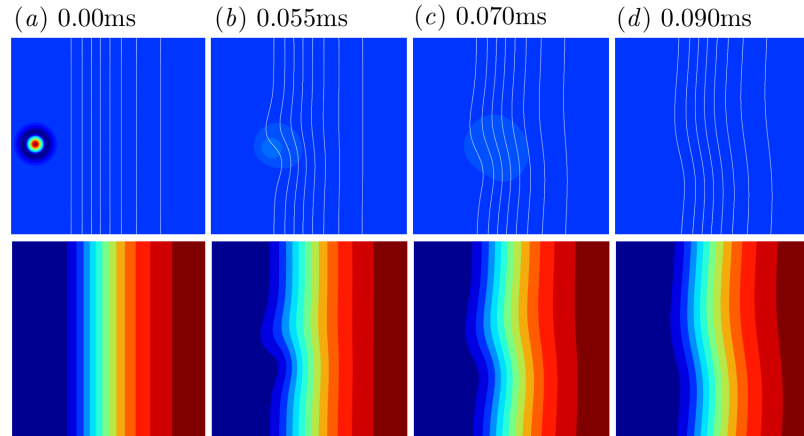
Figure 3.14: Results of run A$^v$ with unaltered viscosity, demonstrating the behavior when diffusion dominates. Top figures are shaded contours of vorticity with lines of constant temperature superimposed and bottom figures are shaded contours of temperature.

transform approximately according the to Eq. 3.73, the flame produces significant amounts of both dilatation and baroclinic torque. The bounds within which this behavior is expected to be observed is approximately $u_v/S_L > 10$ and $l_v/l_F > 6$.

### 3.3.3 Viscous dissipation

In the limit of a small vortex, the time for a vortex to decay (due to viscous effects) is much smaller than the time to pass through the flame, as discussed in section 3.1.2. This is supported by the results of the smallest vortices tested with the unaltered viscosity, runs A$^v$ and B$^v$. These simulations have lower vortex Reynolds numbers than runs A and B, so that viscous effects are relatively more important. Results from run A$^v$ are illustrated in Fig. 3.14. The initial vortex vorticity is presented in Fig. 3.14a, which is the same initial condition as run A. At first, the vortex creates curvature of the flame front as it begins to decay (Fig. 3.14b). However, the diffusion of vorticity is fast, such that the vortex is unrecognizable before passing through the flame (Fig. 3.14c and d). In this way, the only term in the vorticity equation which is relevant in the limit of a small vortex is that of viscous diffusion.

By the simple time scale analysis in section 3.1.2, the largest vortex for which viscous effects will dominate depends on the parameter $a$ (Eq 3.5), which is equal to 23 in the unburnt flow of the

present $H_2$-air configuration. This parameter will vary based on the reactant conditions, so that the onset of the viscous dominated regime is expected to vary as well.

## 3.4    Discussion

In this section, the conclusions presented here are compared with results of previous studies.

Mueller *et al.* [73] performed experiments using vortex rings of almost the same size, $l_v/l_F \simeq 10$ but three different velocities, $u_v/S_L = 1.4, 3.6, 10.1$. These values fall near or within large, slow vortices or large, fast vortices as described above. In the case of the slowest vortex, $u_v/S_L = 1.4$, the vortex was destroyed by the creation of vorticity in the flame, which matches the description of the large, slow vortices. The second case exhibited characteristics of both the large, slow and large, fast vortices, possibly representing an intermediate case between these two limits. In the case of their fastest vortex, $u_v/S_L = 10.1$, the vortex survived through the flame, which agrees with the description of large, fast vortices provided here. However, in this case they observed local extinction of the flame through stretching, but this difference is likely due to the high stretch rate at the leading edge not present in a monopole vortex.

Louch and Bray [60] simulated vortices of only one size and velocity, $l_v/l_F \simeq 10$ and $u_v/S_L = 1.4$, which is a large, and relatively slow vortex. They proposed three regimes that depended on the heat release of the flame and mean pressure gradient, stressing the importance of baroclinic torque. Their regimes progress from low to high heat release and bear resemblance to the description provided here of a small, slow vortex, and a large, slow vortex, respectively. This relates to the results of this study as the magnitude of heat release determines the magnitude of the density gradient across the flame, and is, therefore, related to the magnitude of vorticity produced through baroclinic torque. In other words, reducing the heat release is comparable to reducing the size of the vortex as both result in lower levels of $\partial \tilde{\rho}_o/\partial \tilde{x}$ and baroclinic torque. Given this, the magnitude of the heat release may vary the transition between the limiting behavior of a small, slow and large, slow vortex.

Rutland and Ferziger [95] proposed regimes based upon the Damköhler number which they defined as the ratio of the vortex time scale to the flame time scale, $\tau_1$ to $\tau_2$. Their description of the

low Damköhler regime resembles that of a large, fast vortex provided here and their high Damköhler regime resembles a small, slow vortex described in this work. While the descriptions resemble results presented here, the demarcations between the regimes do not. Relating their definition of the Damköhler number to $l_v/l_F$ and $u_v/S_L$ results in

$$Da = \frac{e^{-0.5}}{4} \frac{l_v}{l_F} \left(\frac{u_v}{S_L}\right)^{-1}, \tag{3.76}$$

demonstrating that lines of constant Damköhler have positive slope in the Fig. 3.5. For example, small, slow vortices can have the same Damköhler number as large, fast vortices. Since their simulations and analysis were performed in a narrower band of $l_v/l_F$ ($4 < l_v/l_F < 20$), defining the regimes based on the Damköhler number sufficiently described their results. However, when conducting analysis with a wider range of size ratios, it is apparent that the Damköhler number does not accurately delineate regimes of behavior of vortex-flame interaction. For example, run B has a Damköhler number of 0.3, which fits into their low Damköhler regime, but clearly behaves like their high Damköhler regime.

## 3.5   Summary and conclusions

In this chapter, the 2D vortex-flame interaction was studied. Numerical simulations with detailed chemistry were performed across three orders of magnitude in $u_v/S_L$ and two orders of magnitude in $l_v/l_F$. Additionally, generalized expansions applied to the governing equations were used to derive leading-order solutions for the vortex and the flame. These methods were used to understand how the flame alters the vorticity through the different terms in the vorticity transport equation and when these terms are important given the initial size and strength of the vortex. Comparison of the analytical and numerical results found five different qualitative behaviors of the vortex-flame interaction. Each regime possesses a dominate term (or terms) in the vorticity transport equation. The resulting effects on vorticity were characterized. Excellent agreement was found between the numerical and theoretical results.

Large ($l_v/l_F \gg 1$) and slow ($u_v/S_L \ll 1$) vortices are able to generate large scale flame curvature which results in the creation of baroclinic torque. The resulting vorticity production destroys the initial vortex. A small ($l_v/l_F \ll 1$) and fast ($u_v/S_L \gg 1$) vortex, when viscous effects do not dominate, is altered only by the effects of dilatation. As a result, the vortex is dampened and expands radially with the density change. A fast and large vortex generates significant distortions to the flame front geometry. Both dilatation and baroclinic torque are important in this case. Though altered, the vortex survives through the flame. A small and slow vortex does not generate any significant effects on the flame. In this case, the vortex is dampened and lengthened normal to the flame due to dilatation when viscous effects do not dominate. In the limit of an infinitely small vortex, viscous effects dominate the transport of vorticity. As a result, the vortex is destroyed before even interacting with the flame.

This study of the vortex-flame interaction yielded a qualitative understanding of how and when the flame effects vorticity through the terms in the vorticity transport equation. Specifically, dilatation acts to reduce vorticity and expand the vorticity in space. This term is primarily important for small vortices when viscous effects do not dominate. Baroclinic torque was active for large vortices and its production was mainly associated with flame curvature. Lastly, viscous effects are important for very small vortices. This qualitative description provides a foundation for investigating vorticity in turbulent combustion, though not all aspects of turbulent combustion are present in the vortex-flame interaction. The results of the current chapter are informative for the following investigation of high Karlovitz number premixed flames and are connected to vorticity transport in turbulent combustion in sections 5.4 and 6.3.

# Chapter 4

# Three dimensional direct numerical simulations[1]

In order to study vorticity within high Karlovitz number premixed flames, a series of direct numerical simulations are performed and analyzed in this thesis. The physical and numerical configuration of these simulations are described within this chapter. A preliminary analysis is performed to verify the turbulent kinetic energy, integral length scale, dissipation rate, and global flame properties are produced as expected. The method of conditional averaging used throughout the subsequent analysis is also introduced here.

## 4.1 Configuration of direct numerical simulations

The physical and numerical configuration of the DNS is described in this section. This simulation configuration is primarily based on the work of Savard *et al.* [103] and Lapointe *et al.* [55].

### 4.1.1 Physical Configuration

The present study considers statistically-stationary, statistically-planar premixed turbulent $n$-heptane/air flames at a slightly lean equivalence ratio ($\phi = 0.9$) and atmospheric pressure. This fuel is chosen as larger hydrocarbon fuels are often used in engine applications. The three-dimensional domain has an inflow and outflow at the left and right $x$ boundaries, respectively, and periodic boundary conditions

---

[1]This chapter is based in large part on the publication [8]: Brock Bobbitt, Simon Lapointe, and Guillaume Blanquart. Vorticity transformation in high Karlovitz number premixed flames. *Phys. Fluids*, 28, 015101 (2016).
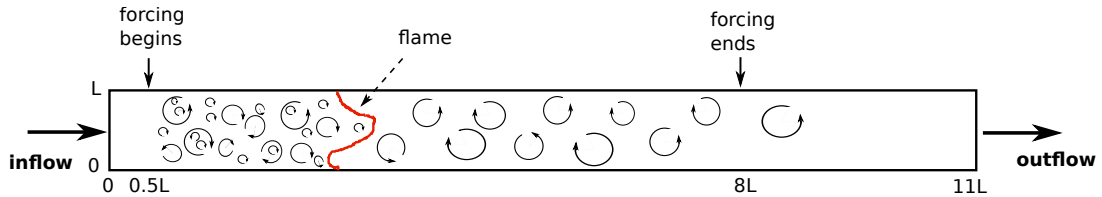
Figure 4.1: Computational domain demonstrating the approximate location of the flame and region of forcing. Diagram taken from Ref. [103].

in the $y$ and $z$ directions (Fig. 4.1). The height and width of the channel are equal and denoted as $L$, while the length, $L_x$, is equal to $11L$. Based on previous studies [94, 11], the turbulence integral length scale is expected to be proportional to the domain width, specifically $l_o = 0.19L$, which is used for the values in Table 4.1 and 4.2 and further discussed in section 4.1.4. Table 4.1 and 4.2 also provide the length scale $\mathcal{L}$, defined as

$$\mathcal{L} = \frac{\pi}{2u'^2} \int_0^\infty \frac{E(\kappa)}{\kappa} d\kappa,$$ (4.1)

which yields similar values as $l_o$. Here, $\kappa$ is the wavenumber and $E(\kappa)$ is the two-dimensional three-component velocity spectrum calculated in the unburnt gas using a single $y$-$z$ plane and averaged over time. A separate DNS is performed of relatively weak, homogeneous, isotropic, triply-periodic box turbulence and is used to generate the inflow condition. The mean inflow velocity is a constant and set to a value that approximates the turbulent flame speed in each case, allowing for an arbitrary long run-time. This configuration was designed to have no mean shear so that the effects of the flame on the turbulence may be studied in isolation.

The turbulence and temperature in the reactants are varied between simulations to investigate the effects of the unburnt Karlovitz number, integral length scale, and flame density ratio. All necessary information about the different simulations is provided in Table 4.1 and 4.2, where $Re_{t,u} = u'l_o/\nu$, $u'$, and $\eta_u$ are the turbulent Reynolds number, rms velocity fluctuation, and Kolmogorov length scale, respectively, all calculated in the unburnt gas. The cases in this study are based on the previous work of Savard $et$ $al.$ [103] and Lapointe $et$ $al.$ [55]. Specifically, cases B and $B_1$ are based on the simulations performed by Savard $et$ $al.$ [103] while cases A, C, C', and D are based on the

|  | A | B | C | C$'$ | C* | D |
|---|---|---|---|---|---|---|
| $T_u$ [K] | 298 | 298 | 800 | 500 | 298 | 800 |
| $\rho_u/\rho_b$ | 7.8 | 7.8 | 3.3 | 4.9 | 7.8 | 3.3 |
| $L_x$[mm] | 25.6 | 25.6 | 16.8 | 18.7 | 25.6 | 16.8 |
| $L$ [mm] | 2.33 | 2.33 | 1.53 | 1.70 | 2.33 | 1.53 |
| Grid | $11 \times 128^3$ | $11 \times 128^3$ | $11 \times 128^3$ | $11 \times 146^3$ | $11 \times 240^3$ | $11 \times 220^3$ |
| $Re_{t,u}$ | 83 | 190 | 170 | 290 | 390 | 380 |
| $Ka_u$ | 70 | 220 | 200 | 650 | 640 | 750 |
| $u'/S_L$ | 9 | 18 | 19 | 38 | 37 | 45 |
| $l_o/l_F$ | 1.1 | 1.1 | 1.2 | 1.0 | 1.1 | 1.2 |
| $\mathcal{L}/l_F$ | 1.3 | 1.2 | 1.3 | 1.0 | 1.1 | 1.2 |
| $\eta_u[\mu\mathrm{m}]$ | 16 | 9 | 7 | 4.6 | 5.1 | 3.5 |
| $S_L$[m/s] | 0.36 | 0.36 | 2.3 | 0.86 | 0.36 | 2.3 |
| $l_F$[mm] | 0.39 | 0.39 | 0.25 | 0.32 | 0.39 | 0.25 |

Table 4.1: Physical and numerical parameters of the DNS which employ finite-rate chemistry and non-unity Lewis number transport.

simulations of Lapointe *et al.* [55]. These simulations are performed in this study with a slightly modified turbulence forcing method, discussed in section 4.1.3. Cases C*, $B_{\mathrm{Tab},1}$, $B_{\mathrm{Tab},1}^4$, and $B_{\mathrm{OS},1}$ are new to this work. Cases $B_1$, $B_{\mathrm{Tab},1}$, $B_{\mathrm{OS},1}$, and $B_{\mathrm{Tab},1}^4$ are performed to test the effects of the transport models, chemical models, and integral length scale, and use the same method described here unless specifically stated otherwise in sections 5.2 or 5.3.1 where they are discussed.

Between the cases studied, the unburnt Karlovitz number and turbulent Reynolds number each vary by an order of magnitude ($Ka_u$=70 - 750, $Re_{t,u}$=83 - 1150). These conditions are chosen so that the Karlovitz number is comparable to those found in a typical gas turbine combustor, which lies on the border of the thin and broken/distributed reaction zone regimes (Fig. 1.3). The unburnt temperature spans conditions of practical relevance ($T_u$=298 - 800$K$) as the reactants in a typical gas turbine may be significantly preheated over atmospheric temperatures [24]. The resulting density ratio across the flames are typical of hydrocarbon fuels near stoichiometric conditions. Cases A, B, and C* have the same density ratio and are used to test the effects of $Ka_u$ independently, while the pairs B, C and C*, C$'$ have the same $Ka_u$ and are used to test the density ratio independently. Case $B_{\mathrm{Tab},1}^4$ has the same Karlovitz number as case B, but an integral length scale which is four times larger. The difference in domain size is demonstrated in Fig, 4.2 which presents instantaneous contour plots of the progress variable from $B_{\mathrm{Tab},1}$ and $B_{\mathrm{Tab},1}^4$. Figure 4.3 shows $Ka_u$ and the density

| | $B_1$ | $B_{Tab,1}$ | $B_{OS,1}$ | $B_{Tab,1}^4$ |
|---|---|---|---|---|
| $T_u$ [K] | 298 | 298 | 298 | 298 |
| $\rho_u/\rho_b$ | 7.8 | 7.8 | 7.3 | 7.8 |
| $L_x$[mm] | 25.6 | 25.6 | 25.6 | 60.6 |
| $L$ [mm] | 2.33 | 2.33 | 2.33 | 9.32 |
| Grid | $11 \times 128^3$ | $11 \times 128^3$ | $11 \times 128^3$ | $2574 \times 512^2$ |
| $Re_t$ | 190 | 190 | 190 | 1150 |
| $Ka_u$ | 280 | 280 | 250 | 280 |
| $u'/S_L$ | 21 | 21 | 22 | 33 |
| $l_o/l_F$ | 1.0 | 1.0 | 1.2 | 4 |
| $\mathcal{L}/l_F$ | 1.0 | 1.0 | 1.2 | 3.7 |
| $\eta_u[\mu m]$ | 9 | 9 | 9 | 9 |
| $S_L[m/s]$ | 0.29 | 0.29 | 0.27 | 0.29 |
| $l_F[m]$ | 0.43 | 0.43 | 0.36 | 0.43 |

Table 4.2: Physical and numerical parameters of additional DNS that vary the transport and chemical models. Subscripts 1, Tab, and OS correspond to simulations using unity Lewis number transport, tabulated chemistry, and one-step chemistry, respectively. Superscript of 4 corresponds to $l_o/l_F = 4$.

ratio for each case as well as their location on the Peters' regime diagram. These conditions span the transition from the thin to broken/distributed reaction zone regimes.

To ensure a statistical steady-state, each case is run initially for at least 13 eddy turnover times ($\tau_o = k/\epsilon$, where $k$ is the TKE) to remove any initial transient effects. After this period, data is collected for over $25\tau_o$ in order to provide sufficient statistical samples. During the simulation, data is collected at a constant rate of approximately $0.5\tau_o$, in order for each data file to represent an independent statistical sample. Further specifications of the simulation conditions are listed in Table 4.1 and 4.2.

## 4.1.2 Governing equations

In this study, we solve the low-Mach number reacting flow equations as outlined in Chapter 2.1. To these equation, a forcing term is added to the momentum equation,

$$\frac{\partial \rho \boldsymbol{u}}{\partial t} + \nabla \cdot (\rho \boldsymbol{u} \otimes \boldsymbol{u}) = -\nabla P + \nabla \cdot \tau + \boldsymbol{f}, \tag{4.2}$$

where $\boldsymbol{f}$ is the applied forcing term. The form of this term will be discussed subsequently.

(a) case $B_{Tab,1}$



(b) case $B_{Tab,1}^4$
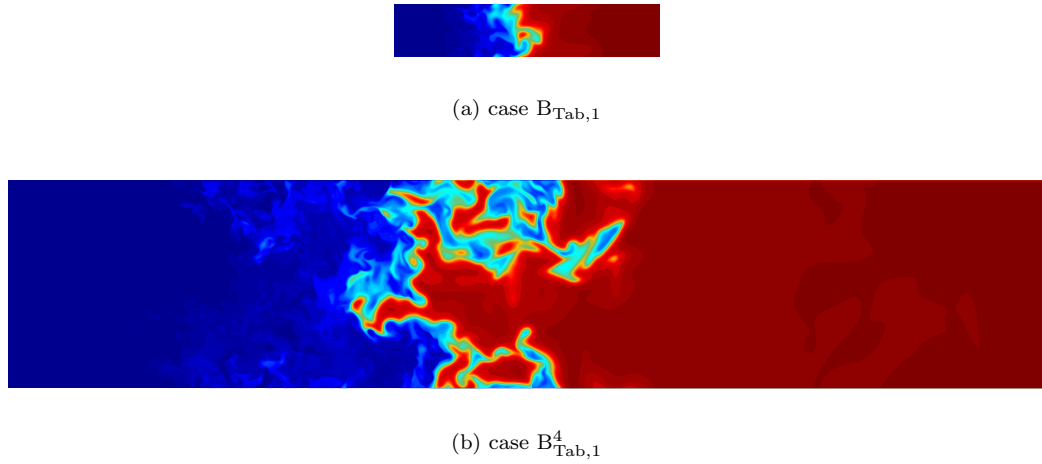
Figure 4.2: Two-dimensional slices of the progress variable $C$ from cases $B_{Tab,1}$ and $B_{Tab,1}^4$. The form of the progress variable is defined section 5.2.2. Each figure represents a region of size $L \times 5L$ and both are scaled to match physical length scales.



(a) Karlovitz numbers and density ratios.

(b) Peters regime diagram [79].
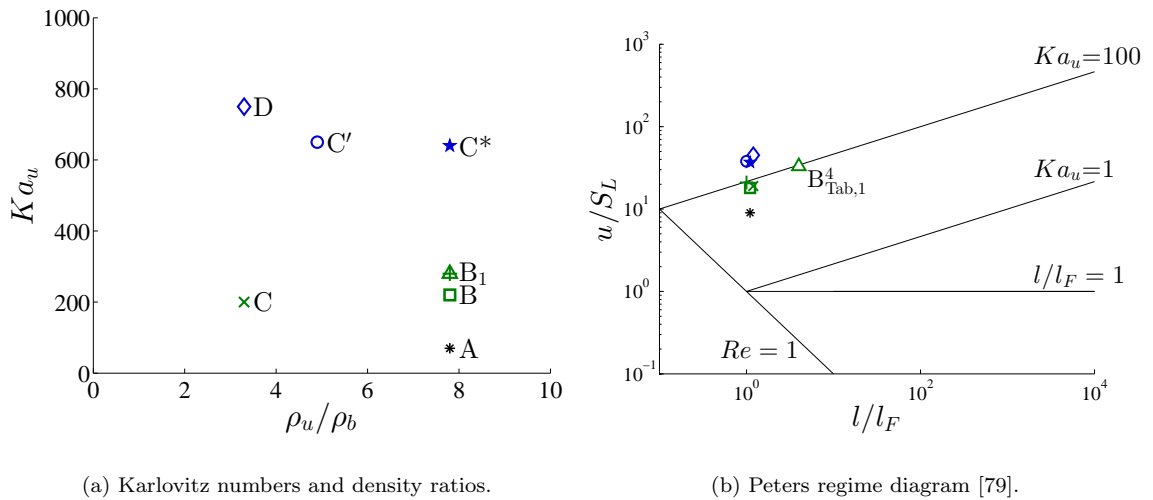
Figure 4.3: Conditions in the unburnt flow of performed simulation. Symbols on the left plot correspond to the same simulations on the right.

The $n$-heptane/air chemistry was modeled with a reduced finite-rate chemical model containing 35 species and 217 reactions (forward and backward counted separately) [6, 103]. An additional reduction of the mechanism from Ref. [6] was performed removing aromatic species, justified by the slightly lean conditions. Constant non-unity Lewis numbers are employed [10], determined as the Lewis numbers of each species in the burnt region in a one-dimensional unstretched premixed flame simulation using full transport. The species Lewis numbers used in these simulations are the same as those listed in the work of Savard and Blanquart [102]. This chemical and transport model has been tested against experimental data and numerical results using full transport (mixture-averaged formulation). Good agreement was found for species mass fractions, species chemical source terms, as well as laminar flame speeds across a wide range of equivalence ratios [102].

The governing equations are solved using the low-Mach, variable density, reacting flow solver NGA [23], discussed in section 2.3. The chemical source term time integration is performed using a recently developed iterative, semi-implicit method that allows numerical time steps limited here only by the convective CFL, while remaining second-order accurate in time and free of lagging errors [100, 104]. The integration uses an approximation of the diagonal of the chemical Jacobian as the preconditioner, which is calculated at negligible computational cost. The overall scheme is second-order accurate in space and time while discretely conserving kinetic energy [23]. Scalar transport is performed with the Bounded QUICK scheme, BQUICK [57, 41]. The numerical resolution is designed to resolve all relevant physical length scales of the turbulence and flame, given by the criteria $\kappa_{max}\eta > 1.5$ [87] and a minimum of 20 grid points per $l_F$ [104]. Additional numerical parameters are also provided in Table 4.1 and 4.2.

### 4.1.3   Turbulence forcing

A variety of configurations have been used in DNS of premixed flames such as V-flames [27], slot Bunsen flames [98, 99], statistically-planar flames with decaying turbulence [77, 16], and statistically-planar flames with forced turbulence [85, 102, 3, 38]. In order isolate the effects of the flame on the turbulence and to reach high Karlovitz numbers, the DNS performed here consider a statistically-

planar flame and use turbulence forcing to prevent the decay of turbulence. Applying the chosen forcing method results in the correct characteristics of the large and small turbulence scales as it mimics the production of turbulence by mean shear. In this section, the alternative approaches are discussed along with the rationale and advantages of the selected configuration. This is followed by a description of the current implementation of the forcing method.

### 4.1.3.1  Shear flow

In one approach, mean shear is present in the flow which generates turbulence through the flame. For example, Sankaran *et al.* [98, 99] studied slot Bunsen flames, which develop downstream of the burner exit, while being statistically-stationary. Dunstan *et al.* [27] investigated V-flames, again, with spatially developing statistics while being statistically-stationary. Lastly, Kolla *et al.* [52] simulated rectangular slot-jet premixed flames which are statistically homogeneous in the plane of the flame, while developing in time. For the purpose of the current study, these configurations present two drawbacks. First, they require directing computational resources towards large domains to contain the mean shear, which limits the highest attainable Karlovitz number for given computational resources. Second, these flows develop in space or time which increases the complexity of isolating the effects of the flame on turbulence.

### 4.1.3.2  Spatially decaying turbulence

To alleviate the difficulties of simulated shear driven turbulence, several studies have considered another class of configurations, where a statistically-planar, statistically-steady flame interacts with decaying homogeneous isotropic turbulence. This was used, for example, in the work of Lipatnikov *et al.* [59] and Chakraborty *et al.* [16] at low to moderate $Ka_u$ ($Ka_u^* = 0.2 - 0.3$ and $Ka_u^* = 0.5 - 13$, respectively).

To assess the feasibility of this configuration for high Karlovitz number flames, it is insightful to consider the limiting, simpler case of non-reacting decaying grid turbulence. Under homogeneous and isotropic conditions, the TKE equation simplifies to $dk/dt = -\epsilon$, and the turbulent eddy turn

(a) Reynolds number.
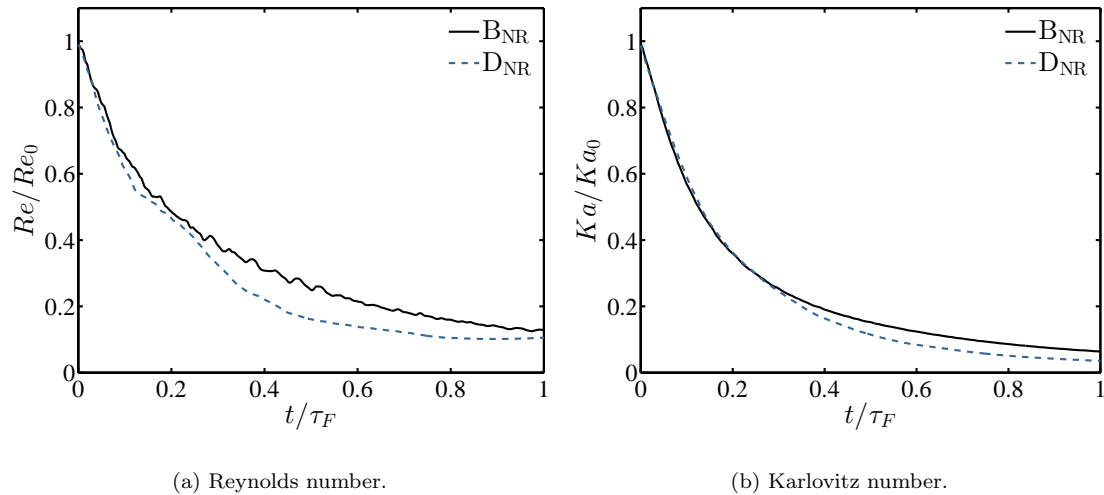
(b) Karlovitz number.

Figure 4.4: Local turbulent Reynolds and Karlovitz numbers for spatially decaying turbulence cases $B_{NR}$ and $D_{NR}$. The Reynolds number is calculated as $Re = (2k/3)^2/(\epsilon\nu)$. The spatial coordinate, $x$, is transformed to time through the bulk flow velocity, $t = x/U_o$. The quantities $Re_0$ and $Ka_0$ are the initial Reynolds and Karlovitz numbers.

over time, $\tau_o = k/\epsilon$, is a measure of the decay rate of the TKE. This time scale should be compared to the time necessary for any flow features to traverse the flame, $\tau_F = l_F/S_L$. The ratio of these two quantities is nothing more than the Damköhler number, $Da = \tau_o/\tau_F$. For low $Da$ number flames, turbulence decays significantly before crossing the flame. For reference, Fig. 4.4 shows the evolution of the local Karlovitz number and Reynolds number for one $\tau_F$ in the unburnt gas for cases B ($Da = 0.1$) and D ($Da = 0.04$), if the forcing is removed. These additional non-reacting simulations are labeled $B_{NR}$ and $D_{NR}$, respectively. As evident from this figure, the decay is such that not only are the Karlovitz numbers no longer high after this time, but the flow is barely turbulent, preventing the study of high Karlovitz number flames. The fast decay can be mitigated by increasing the Damköhler number (or equivalently the integral length scale). While the required larger domain size may be experimentally obtainable, the computational cost is currently prohibitive.

### 4.1.3.3   Forced turbulence

Due to the above considerations, most direct numerical simulations of high Karlovitz number premixed flames considered a statistically planar flame and used turbulence forcing to prevent the decay of TKE. This configuration is similar to that of Lipatnikov *et al.* [59] and Chakraborty *et al.* [16], but

the decay of turbulence is prevented. Various researchers have used this configuration to investigate both the dynamics of the flame [86, 2, 4, 103, 102, 55] and that of the turbulence [38, 37, 84]. For instance, Aspden *et al.* [3] investigated distributed burning in lean hydrogen flames, Poludnenko and Oran [85] studied the mechanisms impacting the turbulent flame speed, and Hamlington *et al.* [37] studied the intermittency of enstrophy.

#### 4.1.3.4 Current implementation

The present study takes a similar approach while selecting linear forcing over spectral forcing. It is relevant here to summarize the analysis of Lundgren [61] on the origins and benefits of linear forcing. By applying a Reynolds decomposition of velocity to the momentum equation, namely, $\boldsymbol{u} = \boldsymbol{u}' + \langle \boldsymbol{u} \rangle$, where $\langle \boldsymbol{u} \rangle$ denotes the ensemble average, the transport equation for the fluctuating velocity, $\boldsymbol{u}'$, may be derived. This equation contains the term $\nabla \langle \boldsymbol{u} \rangle \cdot \boldsymbol{u}'$, which drives the fluctuating velocity as a result of mean shear. In the TKE transport equation, this term becomes $\langle \boldsymbol{u}' \cdot \nabla \langle \boldsymbol{u} \rangle \cdot \boldsymbol{u}' \rangle$, and represents the energy transfer from mean shear into turbulent kinetic energy. It is important to highlight that in practical turbulent reacting flows, the mean shear term is non-zero throughout the flame. In other words, energy production occurs in the preheat zone as well as on the burnt side and throughout the flame. Following this analysis, linear forcing in its basic form appends the term, $A\boldsymbol{u}'$, to the momentum equation. Momentum is thus injected across all wavenumbers and in proportion to the local velocity, just as in shear flows, with production primarily occurring at the large scales [94] (Carroll and Blanquart [12] show that the production spectrum peaks at the large scales). In experimentally obtainable shear flows, produciton is also primarily at the large scales.

Even though some energy (albeit very small) is injected at the small scales, linear forcing has been found to maintain the correct dynamics of these small turbulent scales [94]. As shown by Carroll and Blanquart [12], all forcing techniques (spectral or linear) produce the exact same small scales behavior as characterized by the second order structure function, namely,

$$B_{II}(r) = \frac{\epsilon}{15\nu} r^2 + O(r^4). \tag{4.3}$$

Equation 4.3 was derived analytically by considering a Taylor expansion of the forced Karman-Howarth equation and did not presume any form of the forcing term. This theoretical behavior was also confirmed by numerical simulations, as shown in the same paper. Rosales and Meneveau [94] also concluded that linear forcing leaves the small scale behavior essentially unaltered. The specific forcing method has little impact on the small scale turbulence behavior since these scales are independent of the large scales where the energy is primarily produced.

Appropriate large scale characteristics are also observed. It is important to note that linear forcing does not impose isotropy nor enforces any arbitrary energy spectrum ($\kappa^{-5/3}$ or otherwise) and allows these characteristics to evolve naturally. As a result, the decay rate of the energy spectrum, *i.e.* the $n$ in $E(\kappa) \propto \kappa^{-n}$, was found to be smaller than 5/3 and to depend on the Reynolds number, a result consistent with a large body of experimental studies [12, 75]. This is shown in Fig. 4.5, which presents the two-dimensional three component velocity spectra in the unburnt gas for each of the present cases, calculated in a single $y - z$ plane (at $x = 1.5L$) and averaged over time. Superimposed are the energy spectrum decay rates measured experimentally in decaying grid turbulence [75] for the high Reynolds number limit, $\kappa^{-5/3}$, and for a comparable $Re_\lambda$ of case C*, $\kappa^{-1.35}$. Agreement with the latter demonstrates that the current simulations present the correct scaling of the energy spectrum and capture accurately the energy cascade at the large scales. Therefore, the current forcing method results in the accurate production of both the large and small turbulent scales. This result supports that the turbulence characteristics are correctly represented in the current configuration.

In the current simulations, linear forcing, modified from the work of Carroll and Blanquart [11] by subtracting the Favre average velocity, is employed by appending the following term to the momentum equation,

$$\boldsymbol{f} = A \frac{k_o \rho}{k(x, t)} \left(\boldsymbol{u} - \tilde{\boldsymbol{u}}\right). \tag{4.4}$$

The definition of $\boldsymbol{f}$ differs from Savard *et al.* [103] and Lapointe *et al.* [55] by only using the instantaneous local density, not the planar average. This simplifies the TKE and enstrophy budget
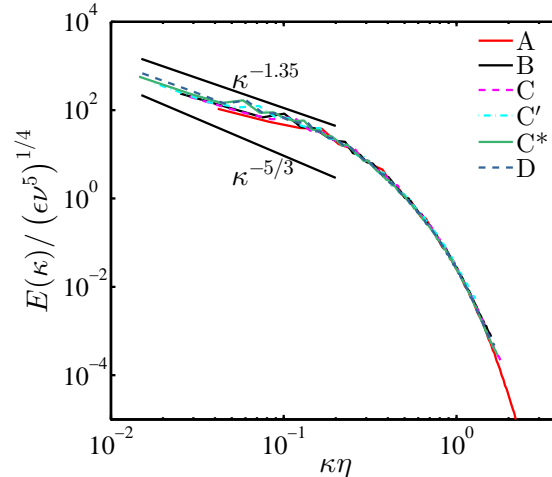
Figure 4.5: The normalized energy spectrum in the unburnt gas for each case. Solid black lines provide the decay rate of the energy spectrum for arbitrarily high $Re_\lambda$ ($\kappa^{-5/3}$) and for $Re_\lambda = 70$ ($\kappa^{-1.35}$) from experimental decaying grid turbulence [75].

analysis, but does not alter the results. Here $A$ is the forcing parameter and is equal to

$$A = 1/(2\tau_o), \tag{4.5}$$

$k_o$ is the target TKE given by the expression

$$k_o = (27/2)l_o^2 A^2, \tag{4.6}$$

and $k(x,t)$ is the instantaneous Favre $y$-$z$ planar averaged TKE, defined as $k(x,t) = \widetilde{\boldsymbol{u}'' \cdot \boldsymbol{u}''}/2$. The planar Favre average for an arbitrary field $\psi$ is defined as $\tilde{\psi} = \overline{(\rho\psi)}/\overline{\rho}$ with $\psi'' = \psi - \tilde{\psi}$, where $\overline{\psi}$ here is the standard planar average,

$$\overline{\psi}(x,t) = \frac{1}{L_y L_z} \int \psi(x,y,z,t)dydz, \tag{4.7}$$

with $\psi' = \psi - \overline{\psi}$. In order to avoid negative velocities at the inflow and outflow, forcing is not applied near these boundaries but within the range $0.5L$ to $8L$ (Fig. 4.1).

Further justification for the present forced approach is provided in section 5.3.2, where the current DNS results are compared to the recent high Karlovitz number slot Bunsen flames of Sankaran *et*

*al.* [99]

## 4.1.4 Forcing analysis

The implemented method of turbulence forcing intends to maintain a constant TKE throughout domain (where the forcing is applied). Figure 4.6a displays the planar averaged TKE for case B, which, as expected, is nearly constant in the region of forcing. The TKE shows a slight dip near the location of the flame and then returns to the imposed value behind the flame. This decrease, though small, is in line with the experimental results of Cheng *et al.* [20] which contain a similar trend.

Next we consider the planar averaged dissipation rate, defined as $\bar{\epsilon} = \overline{\tau' : S''}/\bar{\rho}$ [56]. Figure 4.6b shows that this quantity is constant in the region of forcing. This may be explained through the TKE transport equation for the case of statistical stationarity and homogeneity in the $y$ and $z$ directions,

$$\tilde{u}\frac{\partial k}{\partial x} = -\bar{\epsilon} + 2Ak_o - \widetilde{u''u''}\frac{\partial \tilde{u}}{\partial x} \tag{4.8}$$

$$+ \frac{1}{\bar{\rho}}\frac{\partial}{\partial x}\left(\overline{e_x \cdot \tau \cdot u''} + \frac{1}{2}\overline{u''\rho(u'' \cdot u'')} - \overline{P'u''}\right) - \frac{1}{\bar{\rho}}\overline{\tau} : \overline{S''} - \frac{\overline{u''}}{\bar{\rho}}\frac{\partial \overline{P}}{\partial x} + \frac{1}{\bar{\rho}}\overline{P'\nabla \cdot u''}, \tag{4.9}$$

where $u$ is the velocity in the $x$ direction and $e_x$ is the unit vector in the $x$ direction. The first four terms in this equation, namely the left hand side (LHS), dissipation, forcing, and dilatation, respectively, are plotted in Fig. 4.6c along with the residual, which represents the cumulative magnitude of all the remaining terms. Within the region where the forcing is active, dissipation and forcing are the dominant terms, even through the flame. Therefore, the TKE transport equation reduces to the balance: $\bar{\epsilon} = 2Ak_o$, which is indeed the value obtained by $\bar{\epsilon}$ in Fig. 4.6b.

Previous studies in 3D periodic homogeneous, isotropic turbulence found that linear forcing results in an integral length scale, $l = (2k/3)^{3/2}/\bar{\epsilon}$, which is proportional to the domain size [11], namely about $0.19L$. The integral length scale for the present configuration is fairly constant through the domain and acquires a value of approximately $0.16L$ (Fig. 4.6d). It is important to note that the effective integral length scale, $l$, differs only slightly from the *a priori* integral length scale, $l_o$,

(a) Turbulent kinetic energy.

(b) Dissipation rate.

(c) TKE budget.

(d) Integral length scale.
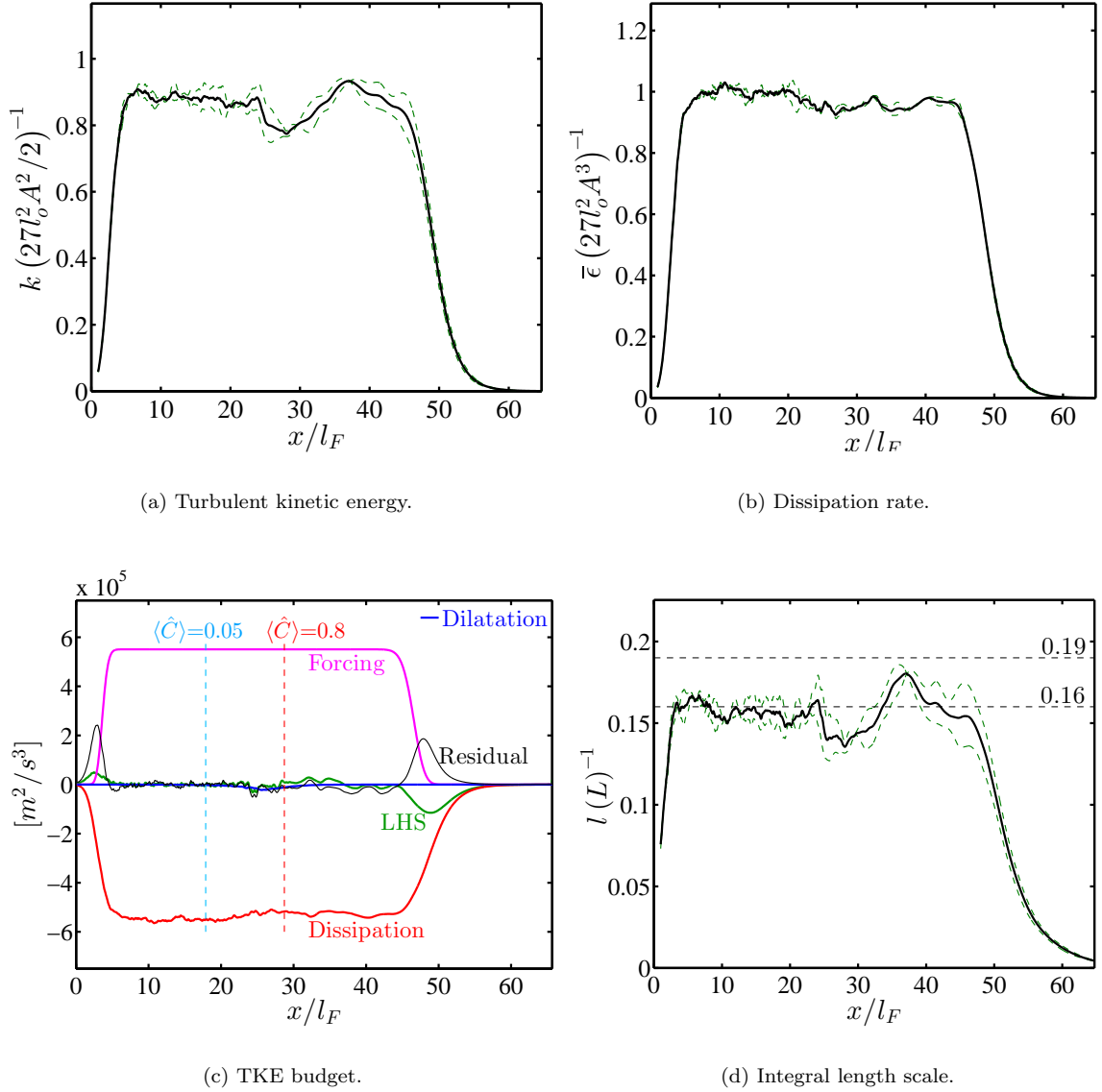
Figure 4.6: Planar and temporal average of turbulent kinetic energy, dissipation rate, and terms in the TKE transport equation, and integral length scale for case B. Green dashed lines correspond to averages when either the first or second half of the data is used; they are indicative of the statistical uncertainty in the computed averages. $\langle \hat{C} \rangle$=0.05 and $\langle \hat{C} \rangle$=0.8 demarcate the extents of the turbulence flame brush ($\hat{C}$ is defined in section 4.3). In (d), 0.19 denotes the approximate size of the integral length scale obtained in previous studies of homogeneous isotropic turbulence with linear forcing [94, 11].

used in setting up the simulations (see section 4.1.1). The difference is the result of a slightly smaller TKE in the present work than observed for homogeneous, isotropic turbulence.

## 4.2 Global flame properties

Two of the most important quantities to characterize a turbulent flame are the turbulent flame speed, $S_T$ and brush thickness, $l_T$, which are reported here. The time-dependent turbulent flame speed, $S_T$ and brush thickness, $l_T$, are presented in Fig. 4.7. The turbulent flame speed is defined as,

$$S_T = \frac{1}{(\rho Y_F)_u L^2} \int_V \rho \dot{\omega}_F dV, \tag{4.10}$$

where $\dot{\omega}_F$ is the fuel source term and the subscript $u$ indicates quantities evaluated in the unburnt gas. The flame brush is defined as the volume of fluid for which the normalized progress variable is between $\hat{C} = 0.05$ and $\hat{C} = 0.8$ divided by the cross-sectional area,

$$l_T = \frac{\text{Vol}(0.05 \leq \hat{C} \leq 0.8)}{L^2}. \tag{4.11}$$

This definition applied to the laminar flames under consideration produces nearly the same flame thickness as the thermal width used above, $l_F = (T_b - T_u)/|\nabla T|_{max}$. As shown in Fig. 4.7, the turbulent flame speed and flame brush thickness change in time, but are statistically constant. This supports that the any initial transient behavior in the simulations has passed. All simulations have been performed for at least $25\tau_o$, but several were run for a longer period of time. Table 4.3 summarizes the time averaged turbulent flame speeds and brush thicknesses. As the Karlovitz number increases, these quantities increase as well. Lapointe *et al.* [55] further investigated the behavior of these quantities (for a fixed ratio of integral length scale to flame thickness), specifically showing that they vary with the reaction zone Karlovitz number. While employing a different definition of the turbulent flame speed and flame brush thickness, Sankaran *et al.* [99] also observed an increase in these quantities with the Karlovitz number.

|         | A   | B   | C    | C′   | C*   | D    |
|---------|-----|-----|------|------|------|------|
| $S_T/S_L$ | 1.5 | 2.0 | 3.3  | 3.3  | 2.6  | 4.8  |
| $l_T/l_F$ | 6.1 | 9.1 | 10.2 | 11.2 | 11.5 | 14.5 |

Table 4.3: Turbulent flame speed and flame brush thickness normalized by their respective laminar quantities.



(a) Turbulent flame speed.



(b) Flame brush thickness.
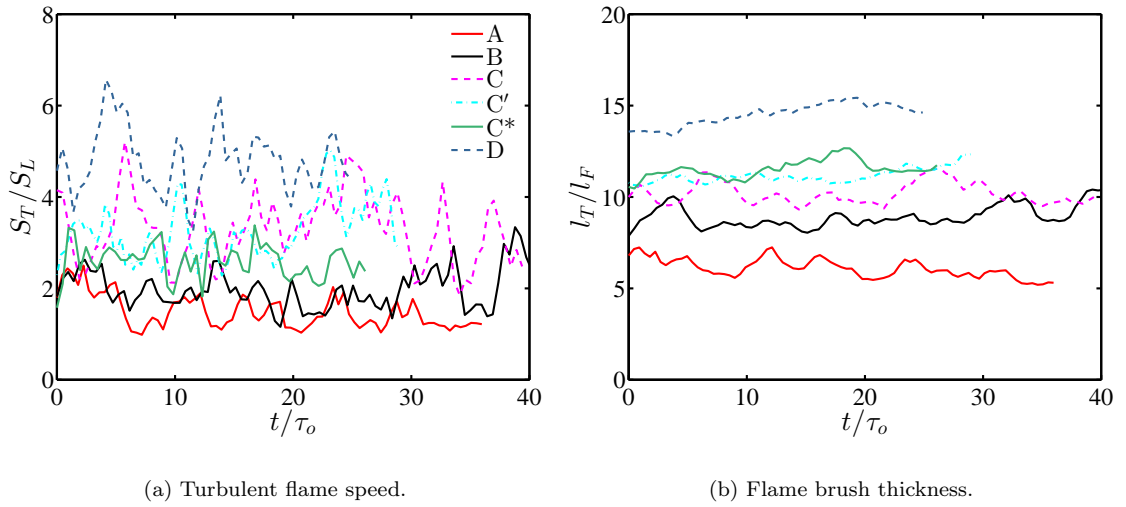
Figure 4.7: Instantaneous turbulent flame speed and flame brush thickness normalized by their respective laminar quantities. The time $t = 0$ corresponds to the beginning of the period over which data is collected.

## 4.3 Conditional averaging

This study reports quantities primarily through conditional averages in order to present their behavior *through* the flame. Turbulence quantities are expected to vary through the flame based upon the local thermodynamic properties of the fluid (such as density and viscosity). In a curved and transient flame, these quantities correlate better with a flame progress variable, denoted as $C$ (Fig. 4.8a), compared to the spatial coordinate $x$. For this reason, averages are conditioned on $C$ and denoted as

$$\langle \psi | C \rangle \tag{4.12}$$

for a given field $\psi$. As each fluid property (especially density) collapses to a single curve as a function of $C$, Reynolds and Favre averages are virtually identical in $C$ space. The form of the progress variable chosen is $C = Y_{H_2O} + Y_{H_2} + Y_{CO_2} + Y_{CO}$, as it tracks the flame evolution through the preheat and reaction zones. Additionally, its maximum value was found to exhibit little dependence on the unburnt temperature [69]. The progress variable range is standardized by considering

$$\hat{C} = \frac{C}{C_{max}} \tag{4.13}$$

so that 0 represents the reactants and 1 represents the products. Conditional averages are performed excluding the domain outside the region of turbulence forcing due to the presence of very weak turbulence. Figure 4.9 is provided to illustrate this averaging procedure by considering the enstrophy in case B. This figure presents the pointwise values of the enstrophy versus the progress variable at one instance in time (the local values without any averaging imposed) which includes more than $1.2 \times 10^7$ individual data points. Also plotted in this figure is the conditional average of enstrophy at this time snapshot (representing the conditional average of one data file), and the conditional average of the enstrophy over the entire simulation time (averaging over all data files). Each conditional average is performed using 50 individual bins in $C$.

By use of this conditional averaging, we define the local Kolmogorov time, length, and velocity

(a) Fluid properties.
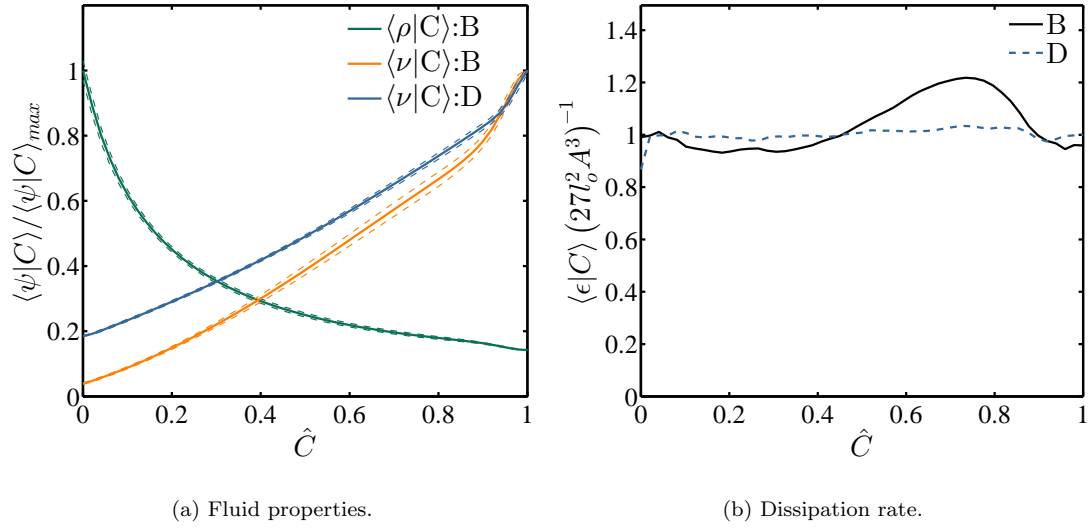
(b) Dissipation rate.

Figure 4.8: (a) Conditional average of density and viscosity; the standard deviation about the mean is represented by dashed lines. (b) Dissipation rate conditioned on the progress variable $C$ and normalized by its approximate value, $27l_o^2 A^3$, imposed by the forcing [11].
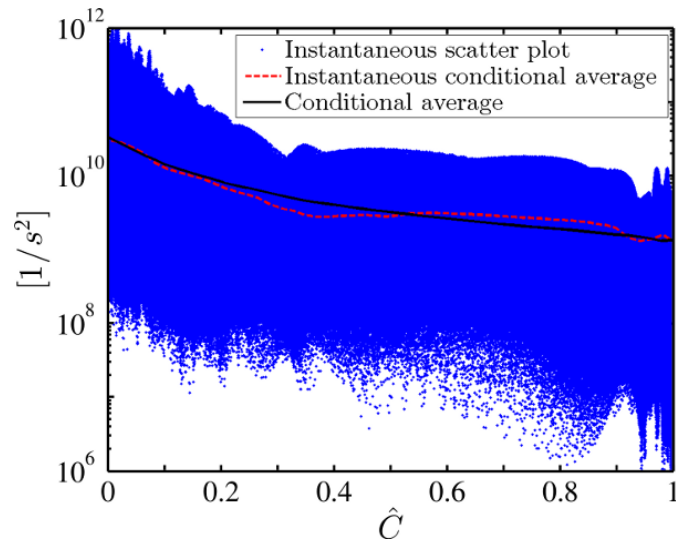


Figure 4.9: Pointwise values of the enstrophy versus the progress variable at one instance in time (blue symbols), the conditional average of enstrophy at this time snapshot (red dashed line), and the conditional average of enstrophy over the entire simulation time (solid black line) for case B to illustrate the averaging procedure used in this thesis.

scales as

$$\tau_\eta(C) = \left( \frac{\langle \nu | C \rangle}{\langle \epsilon | C \rangle} \right)^{1/2}, \tag{4.14}$$

$$\eta(C) = \left( \frac{\langle \nu | C \rangle^3}{\langle \epsilon | C \rangle} \right)^{1/4}, \tag{4.15}$$

$$u_\eta(C) = (\langle \epsilon | C \rangle \langle \nu | C \rangle)^{1/4}, \tag{4.16}$$

the local Karlovitz number as

$$Ka(C) = \tau_F / \tau_\eta(C), \tag{4.17}$$

and the dissipation rate conditioned on $C$ as

$$\langle \epsilon | C \rangle = \langle \tau' : S'' | C \rangle / \langle \rho | C \rangle. \tag{4.18}$$

Additionally, we define a quantity involving the flame density change,

$$\gamma(C) = \Delta\rho / \langle \rho | C \rangle, \tag{4.19}$$

where $\Delta\rho = \rho_u - \rho_b$, which will be used in the subsequent analysis. Further references to the Karlovitz number and the Kolmogorov scales are written as $\tau_\eta$, $\eta$, $u_\eta$, and $Ka$, where the dependence on $C$ is implicit.

It is relevant to note that conditioning on $C$ rather than $x$ can highlight aspects of the turbulence transformation. This is demonstrated through comparing the dissipation rate conditioned on $x$ and $C$ for two cases, B and D. As mentioned earlier, $\epsilon$ conditioned on $x$ is constant in the region of forcing for both cases (Fig. 4.6b). However, $\epsilon$ is able to vary as a function of $C$ within each plane, which is observed for case B, and D to a much lesser extent (Fig. 4.8b). As the Karlovitz number increases, the variation in $\langle \epsilon | C \rangle$ deceases, as shown by case D.

## 4.4 Summary and conclusions

In this chapter, the physical and numerical configurations of the DNS performed in this thesis were presented. Preliminary analysis of these high Karlovitz number premixed flames showed that the turbulent kinetic energy, integral length scale, and dissipation rate agree well with the values expected based on previous work. It was also found that the turbulence increases the turbulent flame speed and thickness over that of the respective laminar flames. This behavior is as expected given the results of comparable turbulent flames in previous studies. The DNS results are analyzed in the subsequent chapters to study the behavior enstrophy and vorticity isotropy in these flames.

# Chapter 5

# Enstrophy transport[1]

In the present chapter, the simulations described in chapter 4 are analyzed to investigate the behavior of enstrophy in high Karlovitz number premixed flames. This analysis is used to assess the validity of Kolmogorov's first similarity hypothesis within these flames. To characterize the behavior of enstrophy through the flame, the terms in the enstrophy transport equation are analyzed, and a scaling is proposed for each term. Employing these scalings, a normalized enstrophy transport equation is proposed that involves only a small set of parameters. This equation is used to characterize the behavior of enstrophy in the limit of high Karlovitz number. Comparison is then made between the behavior of enstrophy within the flame and in homogeneous isotropic turbulence.

The current simulations are performed using a statistically-planar flame with forced turbulence. To demonstrate the applicability of the present conclusions to alternative configurations, the results are compared in this chapter with the recent high Karlovitz number slot Bunsen flame of Sankaran *et al.* [99]. This case provides comparison of an unforced, shear driven, high Karlovitz number flame with the present forced, zero mean shear, high Karlovitz number flames.

The primary analysis in this chapter is performed using simulations employing a finite-rate chemical model with constant non-unity Lewis number transport. To determine the impact of simplified chemical and transport models, the results are compared with simulations using alternative models but having the same physical conditions. Lastly, the impact of the turbulent Reynolds number on the results is analyzed.

---

[1]This chapter is based in large part on the publication [8]: Brock Bobbitt, Simon Lapointe, and Guillaume Blanquart. Vorticity transformation in high Karlovitz number premixed flames. *Phys. Fluids*, 28, 015101 (2016).

## 5.1 Analysis of enstrophy transport

In this section, the results are introduced and scaling estimates for each term of the enstrophy equation, namely vortex stretching, dilatation, baroclinic torque, viscous dissipation, and forcing, are derived to explain their variation through the flame and across reactant conditions. Predictions from this analysis are tested using results from the present DNS.

### 5.1.1 Overview

The enstrophy, $\omega^2 = \boldsymbol{\omega} \cdot \boldsymbol{\omega}$, transport equation is derived from the momentum equation (Eq. 4.2) as

$$\frac{1}{2}\frac{D\omega^2}{Dt} = \boldsymbol{\omega} \cdot S \cdot \boldsymbol{\omega} - \omega^2 \left(\nabla \cdot \boldsymbol{u}\right) + \frac{\boldsymbol{\omega}}{\rho^2} \cdot \left(\nabla\rho \times \nabla P\right) + \boldsymbol{\omega} \cdot \nabla \times \left(\frac{1}{\rho}\nabla \cdot \tau\right) + \boldsymbol{\omega} \cdot \nabla \times \frac{\boldsymbol{f}}{\rho}, \qquad (5.1)$$

where $D/Dt$ is the material or total derivative. Each term on the right hand side is associated with a specific physical processes: vortex stretching, dilatation, baroclinic torque, viscous dissipation, and forcing, respectively. Vortex stretching, viscous dissipation, and forcing are active in constant density flows, while dilatation and baroclinic torque arise here only due to the presence of the flame. The change of fluid properties (such as density and viscosity) within a premixed flame alters the enstrophy of the incoming turbulence through these five terms.

To begin the discussion of enstrophy, a budget analysis of its transport equation is performed for case B (Fig. 5.1) to demonstrate behavior common to all cases tested. The other cases show similar trends, but baroclinic torque and dilatation are observed to have even smaller magnitudes relative to the other terms (with the exception of case A for which these two terms are slightly larger). Additionally, the magnitude of the forcing term relative to vortex stretching and viscous dissipation decreases from cases A, to B, to C* to D. In Fig. 5.1, the terms are conditionally averaged on $x$ specifically to illustrate the flow configuration. In order to minimize numerical errors, the calculation of each term is performed using compact finite difference stencils and minimal spatial interpolations, accounting for the spatial staggering of variables. The flow enters the domain on the left side of the figure with very weak turbulence; vortex stretching, viscous dissipation, and forcing
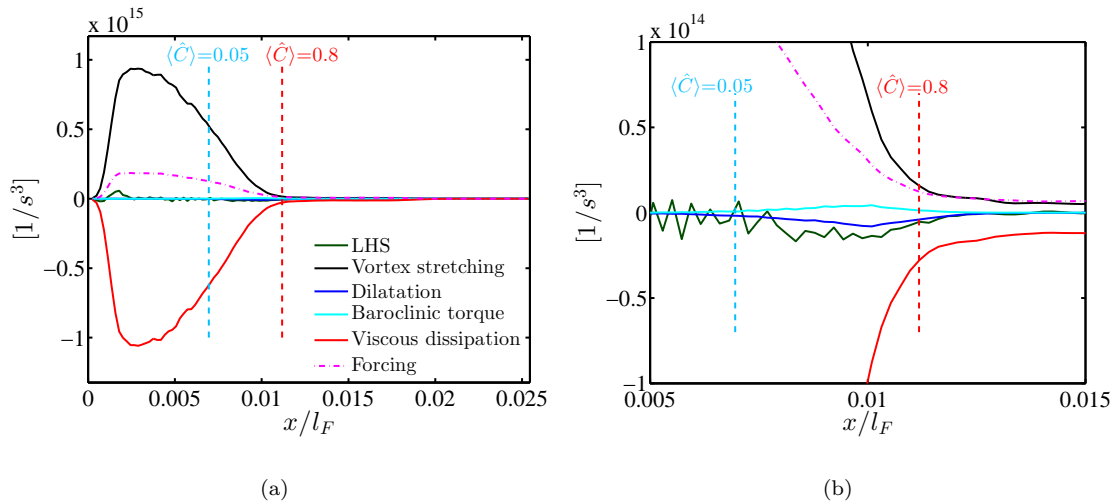
Figure 5.1: Spatially and temporally averaged terms in the enstophy budget equation of case B for (a) the entire domain and (b) the location of the flame. $\langle \hat{C} \rangle$=0.05 and $\langle \hat{C} \rangle$=0.8 demarcate the approximate extents of the turbulence flame brush.

then increase due to the onset of turbulence forcing ($x/l_F \simeq 3$). These terms maintain fairly constant values in the unburnt region, and subsequently decrease through the flame to smaller values in the burnt region. The flame location may be approximated by the peak density gradient which occurs near $x/l_F = 22$ in Fig. 5.1. Dilatation and baroclinic torque peak within the flame, but they have a smaller magnitude than the other three terms (for all the present cases). Lastly, each term approaches zero as the forcing subsides ($x/l_F \simeq 48$) prior to the outflow.

Next, the transformation of enstrophy is qualitatively observed by plotting the vorticity magnitude through the flame. Figure 5.2 displays instantaneous 2D contours of cases A, B, C, C*, and D. The change in vorticity is dramatic as the magnitude is greatly suppressed through the flame. Preliminary observation suggests the vorticity is reduced to a lesser extent in cases C and D, which have a similar $Ka_u$ as B and C*, respectively, but a higher unburnt temperature. The vorticity magnitude is significantly altered by the flame for all values of $Ka_u$ tested, in contrast to the observations of Hamlington *et al.* [38] who found the vorticity magnitude varied little through the flame at similar $Ka_u$ values. Possible reasons for these differences will become more apparent in the following and further discussed in section 7.6.
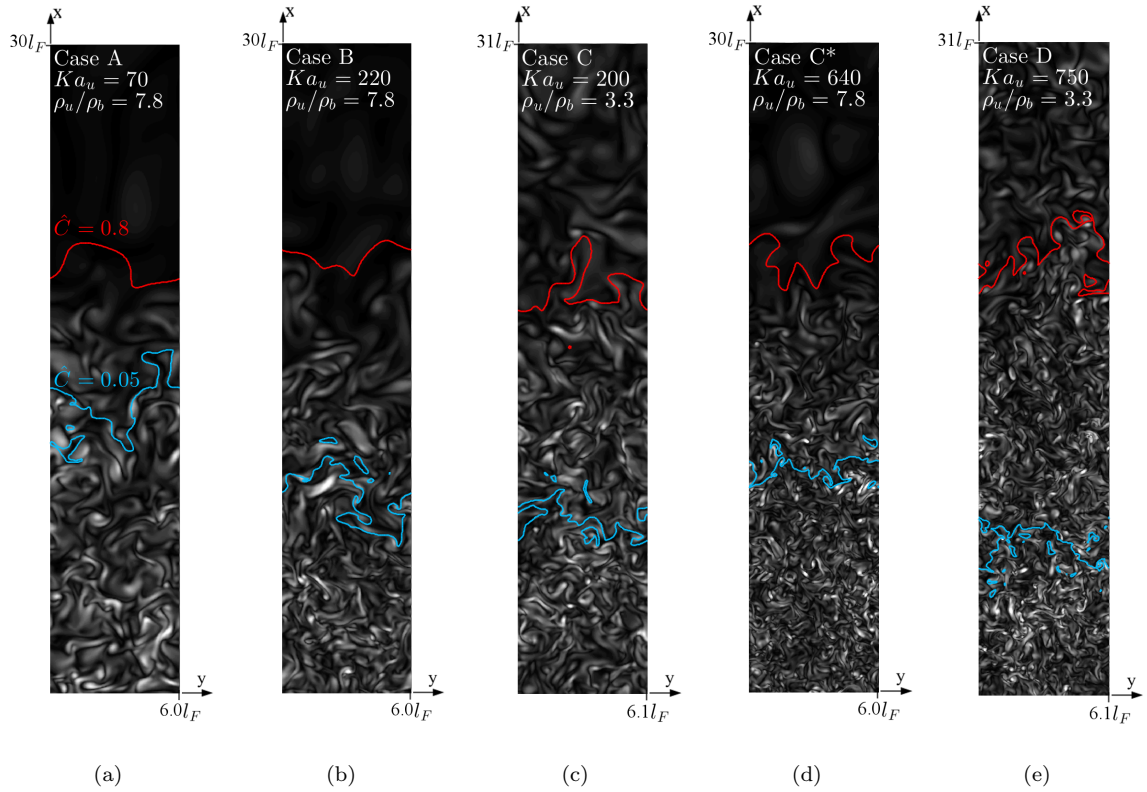
Figure 5.2: Two-dimensional slices of vorticity magnitude for cases A, B, C, C*, and D. Each figure corresponds to a region of size $L \times 5L$ and the flow direction is from bottom to top. Height and width dimensions are relative to region plotted in the figures. The contours range between $[0; 2.1e5\ s^{-1}]$, $[0; 6.2e5\ s^{-1}]$, $[0; 5.5e6\ s^{-1}]$, $[0; 1.7e6\ s^{-1}]$, and $[0; 2.1e7\ s^{-1}]$, respectively. Blue and red contours represent the extent of the turbulent flame brush defined as the iso-surfaces of $\hat{C} = 0.05$ and $\hat{C} = 0.8$.

## 5.1.2 Vortex stretching

In dimensional form, the vortex stretching term can vary by more than an order of magnitude across the flame and varies by several orders of magnitude between the different cases (Fig. 5.3a). Scaling of this term requires estimates for vorticity and the rate of strain tensor.

Scaling the rate of strain tensor is accomplished through the viscous dissipation rate

$$\langle \epsilon | C \rangle = \langle \tau' : S'' | C \rangle / \langle \rho | C \rangle. \tag{5.2}$$

By assuming the molecular viscosity is only a function of the progress variable, $\mu = \mu(C)$, Eq. 5.2 may be rewritten as,

$$\frac{1}{2\tau_\eta^2} = \langle S' : S'' - \frac{1}{3}(\nabla \cdot \boldsymbol{u})'(\nabla \cdot \boldsymbol{u})'' | C \rangle. \tag{5.3}$$

Next, by assuming conditional Favre and Reynolds averages are equivalent (section 4.3), the following equation may be obtained,

$$\langle S' : S' | C \rangle = \frac{1}{2\tau_\eta^2} + \frac{1}{3}\langle (\nabla \cdot \boldsymbol{u}')^2 | C \rangle. \tag{5.4}$$

By this, the rate of strain tensor scales with the Kolmogorov time scale, a quantity related to the turbulence characteristics, as well as the velocity divergence, a quantity related to the flame characteristics. The velocity divergence may be rewritten through the continuity equation as $-(D\rho/Dt)/\rho$ and estimated using the density jump across the flame and the laminar flame timescale,

$$\langle \nabla \cdot \boldsymbol{u} | C \rangle \propto \frac{-1}{\langle \rho | C \rangle} \frac{\Delta \rho}{l_F / S_L}. \tag{5.5}$$

The magnitudes of these two components of the rate of strain tensor are then compared through the ratio,

$$\frac{1/\tau_\eta}{\Delta \rho / (\rho l_F / S_L)} = \frac{1}{\gamma} Ka. \tag{5.6}$$

As this ratio gets larger, the component related to the turbulence increases in magnitude compared to the component related to the flame. Therefore, in the present configuration of high Karlovitz

(a) Dimensional.
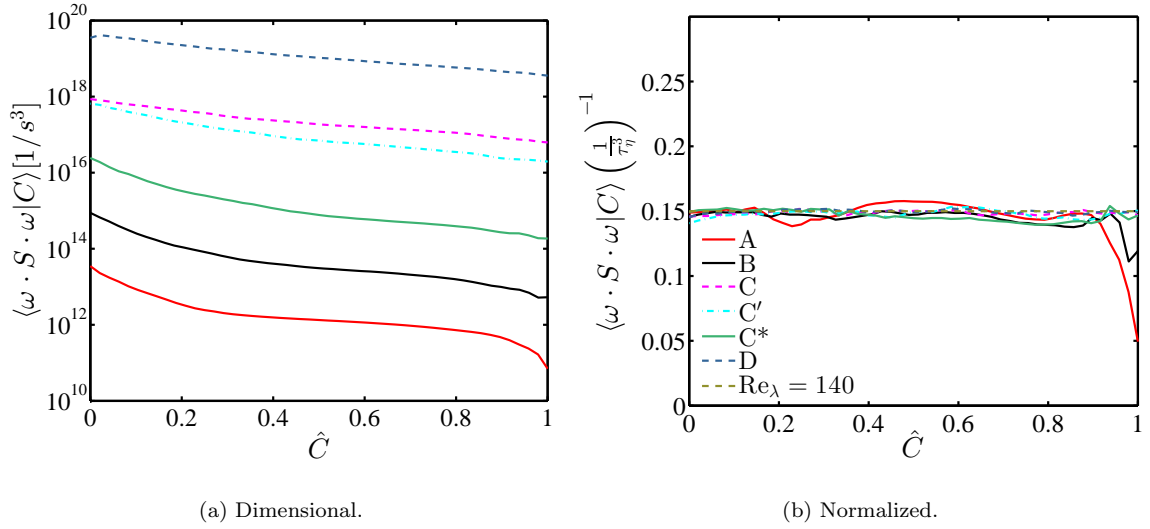
(b) Normalized.

Figure 5.3: Vortex stretching term in dimensional and normalized form. The line $Re_\lambda$ is calculated from the previous simulations of homogeneous, isotropic turbulence by Carroll and Blanquart [11].

number ($Ka_u > 70$), the magnitude of $S$ is estimated as $1/\tau_\eta$. This result is consistent with homogeneous, isotropic turbulence where $\overline{S' : S'}$ also scales as $(1/\tau_\eta^2)$ [87]. As a spatial gradient of velocity, like the rate of strain tensor, vorticity is estimated as $1/\tau_\eta$ and enstrophy with $1/\tau_\eta^2$. Previous experimental and numerical work supports a correlation of vorticity with the Kolmogorov time scale under conditions of homogeneous, isotropic turbulence [88, 46, 72]. The above analysis results in the scaling,

$$\langle \boldsymbol{\omega} \cdot S \cdot \boldsymbol{\omega} | C \rangle \propto \frac{1}{\tau_\eta^3}. \tag{5.7}$$

The same scaling was obtained in the case of homogeneous isotropic turbulence by Tennekes and Lumley [112].

Normalized according to the above expression, the vortex stretching term for each case collapses to a fairly constant value close to 0.15, which is the same value obtained in DNS of homogeneous, isotropic turbulence (Fig. 5.3b). Near $\hat{C} = 0.95$, the values for cases A and B decrease below 0.15; and at this point, the local values of $Ka/\gamma$ are 2.1 and 6.5, respectively, which are the lowest values among all the cases. As the validity of Eq. 5.7 depends on Eq. 5.6 being large, this observed decrease may be due to the low values of $Ka/\gamma$ and a breakdown of the proposed scaling. Otherwise, the

(a) Dimensional.
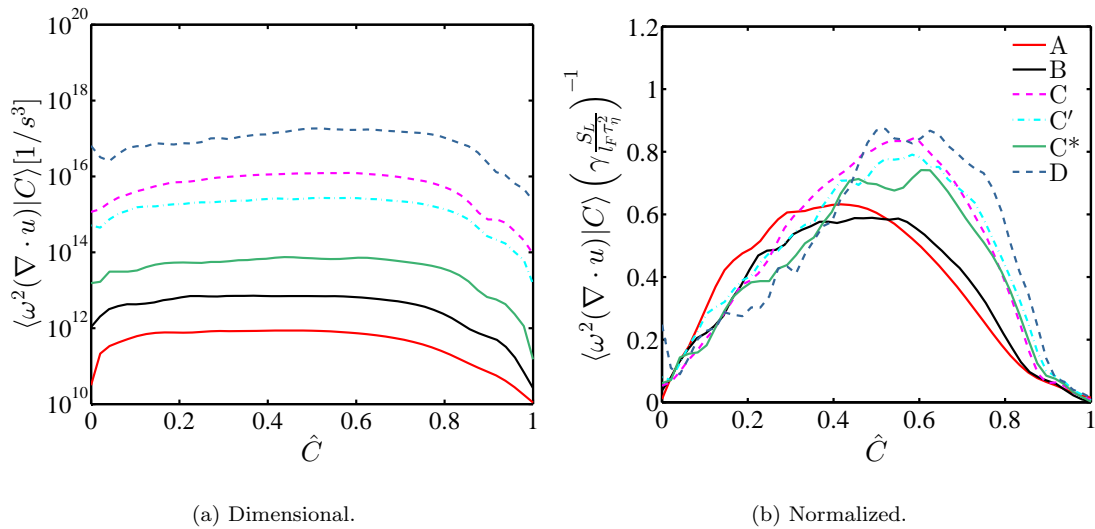
(b) Normalized.

Figure 5.4: Dilatation term in dimensional and normalized form.

proposed normalization accurately represents the changes in this term through the flame and across all runs. The small magnitude of the constant obtained for this term (0.15) may be due to the preferential alignment of vorticity with the second eigenvector of the rate of strain tensor [38], whose eigenvalue is known to be small [113, 1]. The success of the normalization suggests that within the flame, the vortex stretching term behaves similar to homogeneous, isotropic turbulence in the limit of high Karlovitz number.

### 5.1.3 Dilatation

Dilatation in the present configuration is due only to the effects of the flame. Therefore, it will tend toward zero away from the flame. This is shown in Fig. 5.4a, where dilatation decreases going towards the largest and smallest values of the progress variable and the peak value varies by nearly six orders of magnitude between cases. Scaling the dilatation term requires estimates of enstrophy and the divergence of velocity, which are analyzed in the previous subsection on vortex stretching. This leads to the following scaling:

$$\langle \omega^2 (\nabla \cdot \boldsymbol{u}) | C \rangle \propto \gamma \frac{S_L}{l_F \tau_\eta^2}. \tag{5.8}$$

Normalized in this manner, results from all cases obtain a similar trend and magnitude (Fig. 5.4b). In the present cases, the peak value increases slightly with a higher unburnt Karlovitz number and lower flame density ratio. Considering the wide range of conditions tested, the curves in Fig. 5.4b are sufficiently similar to support that Eq. 5.8 captures the scaling of dilatation. Additionally, the peak value obtained is near unity, supporting that the normalization captures not only the scaling of this term but the magnitude as well.

### 5.1.4   Baroclinic torque

Baroclinic torque, like dilatation, is only present due to the density variations within the flame. Likewise, it tends toward zero in the reactants and products. This is shown in Fig. 5.5a, which also demonstrates that the peak value varies by orders of magnitude between cases. Though analytically equivalent, baroclinic torque is calculated as $\boldsymbol{\omega} \cdot \nabla \times (\nabla P / \rho)$ rather than $\boldsymbol{\omega} \cdot (\nabla \rho \times \nabla P) / \rho^2$ to reduce errors in the numerical evaluation. Scaling of baroclinic torque requires estimates for the gradients of pressure and density. In this estimate, only the magnitude and not alignment of these two vectors are considered.

Analogous to the previous analysis for the rate of strain tensor, we consider pressure decomposed into turbulence and flame related quantities and note that through dimensional analysis pressure gradients scale with $\rho u^2 / l$. Using quantities related to the flame produces the scaling $\rho S_L^2 / l_F$. Using turbulent quantities, this scaling is largest at the smallest turbulent length scales, providing the scaling $\rho u_\eta^2 / \eta$. The ratio of these scalings is given by,

$$\frac{\rho u_\eta^2 / \eta}{\rho S_L^2 / l_F} = \alpha Ka^{3/2}, \tag{5.9}$$

where $\nu(C) = \alpha(C)^2 S_L l_F$. Given the present definition of $l_F$, $\alpha(C)$ commonly varies between about 0.1 to 1. Therefore, in the present case of high $Ka$, the pressure gradients scale with the turbulence quantities, $\rho u_\eta^2 / \eta$.

Next, the gradient of density is estimated. Analogous to the temporal derivative of density, we

(a) Dimensional.
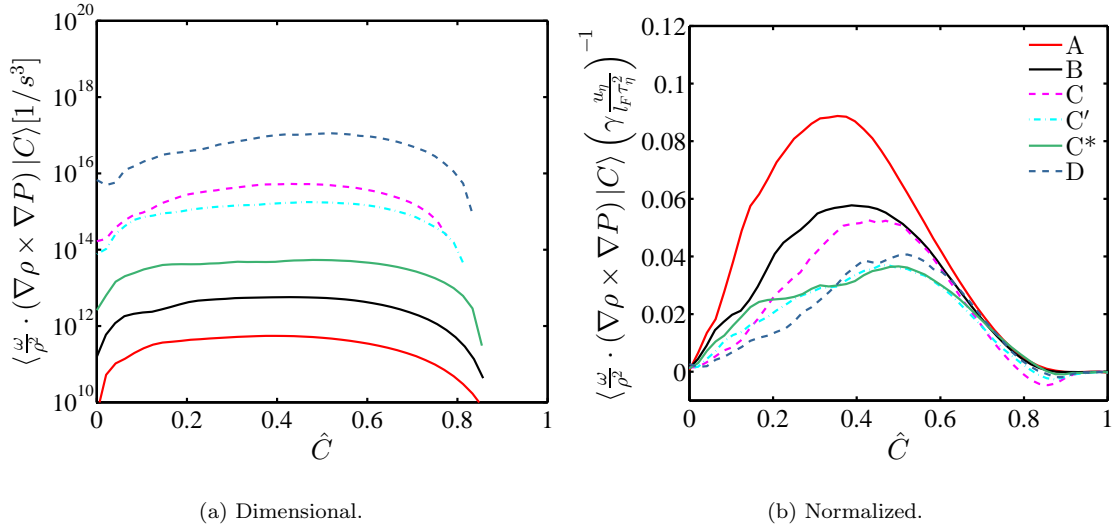
(b) Normalized.

Figure 5.5: Baroclinic torque term in dimensional and normalized form.

scale spatial density gradients with the density change across the flame, $\Delta\rho$, divided by the laminar flame thickness so that, $\frac{\partial\rho}{\partial x} \simeq \frac{\Delta\rho}{l_F}$. The following scaling for baroclinic torque is obtained:

$$\langle \frac{\boldsymbol{\omega}}{\rho^2} \cdot (\nabla\rho \times \nabla P)|C\rangle \propto \gamma \frac{u_\eta}{l_F \tau_\eta^2}. \tag{5.10}$$

When normalized according to the above expression, the variation in the peak value between the six cases reduces from five orders of magnitude to a factor of 2 (Fig. 5.5). The peak value is small and varies from 0.1 at the lower Karlovitz numbers to a constant value of about 0.04 for sufficiently high Karlovitz numbers. This transition is made more clear in Fig. 5.6a, which shows for each case the peak value of the normalized baroclinic torque versus the local Karlovitz number. To possibly reduce this variability with $Ka$, two alternative scalings are proposed: multiplying the proposed scaling with $1/\sqrt{Ka_u}$ and replacing $l_F$ with $l_T$ (Fig. 5.6b and c, respectively). Both reduce the overall variability; however, the first is somewhat arbitrary and the second requires an *a priori* expression for $l_T$ based on $l_F$ and $Ka_u$ for further scaling analysis, of which no adequate expression is known. The original scaling is used subsequently for its theoretical basis, suitability for scaling analysis, and consistent behavior at high Karlovitz number, which is the focus of the present study. As the present simulations only include pressure gradients from hydrodynamic pressure fluctuations,

(a) Scaling of Eq. 5.10.    (b) Alternative scaling 1.    (c) Alternative scaling 2.
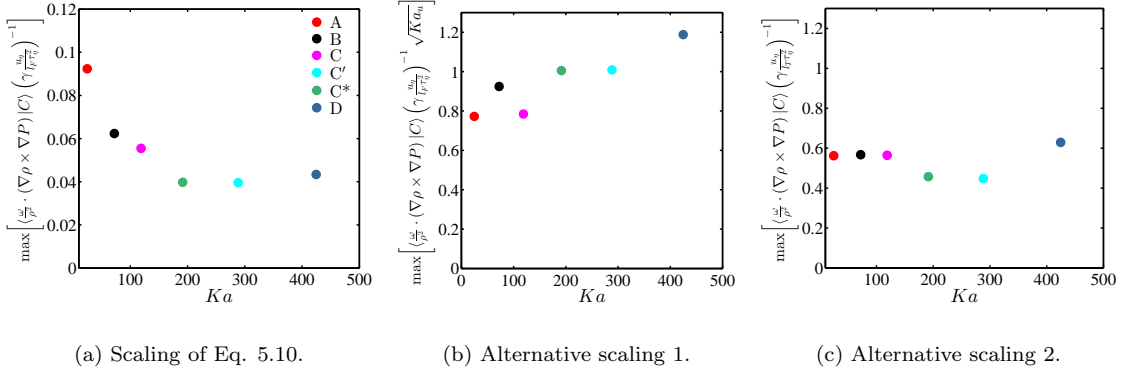
Figure 5.6: Peak value of normalized baroclinic torque plotted against the local value of $Ka$ for the scaling proposed in Eq. 5.10, along with two alternative scalings: multipling Eq. 5.10 by $Ka_u^{-1/2}$, and employing $l_T$ in place of $l_F$.

the overpressures discussed by Poludnenko [84] and observed to play a role in the production of baroclinic torque are not included here. However, their effect on vorticity transport was observed to be lower at higher Karlovitz numbers [84], suggesting their relevance to the transport of enstrophy diminishes as $Ka$ increases. Their effect at high $Ka$ on vorticity and anisotropy should be the subject of future work.

To further investigate the mechanisms controlling the magnitude of baroclinic torque, the normalized gradients of density and pressure are calculated (Fig. 5.7). Though baroclinic torque decreases with $Ka_u$, these quantities do not. The gradient of pressure increases with $Ka_u$, due to finite $Re$ effects, and the density gradient primarily varies with the flame density ratio. Additionally, as both have a magnitude close to unity, the small peak magnitude of the normalized baroclinic torque is not explained by the behavior of these quantities. Next, the alignment of the density and pressure gradient vectors is calculated. Figure 5.7c shows for case B that these vectors are either preferentially parallel or anti-parallel. Either case corresponds to a cross product of zero, so that the preferential alignment modulates the magnitude of baroclinic torque. This alignment of the pressure and density gradients is not accounted for in the proposed scaling (Eq. 5.10), hence the small magnitude observed in Fig. 5.5b.

(a) Normalized pressure gradient norm.

(b) Normalized density gradient norm

(c) Conditional PDF of $\nabla\rho \cdot \nabla P/|\nabla\rho||\nabla P|$ for case B.
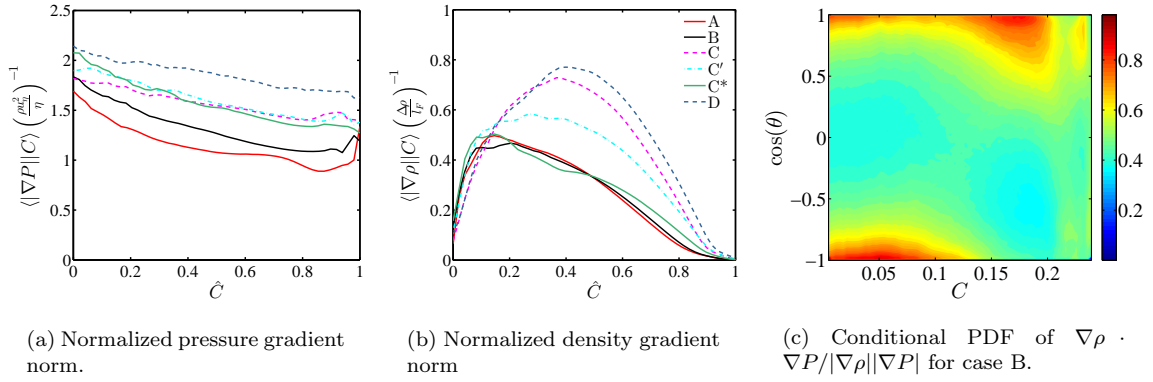
Figure 5.7: Normalized components of baroclinic torque and preferential alignment of pressure and density gradients. In (c), the angle between the vectors, $\theta$, is defined such that $\cos(\theta) = 0$ represents perfect misalignment.



(a) Dimensional.
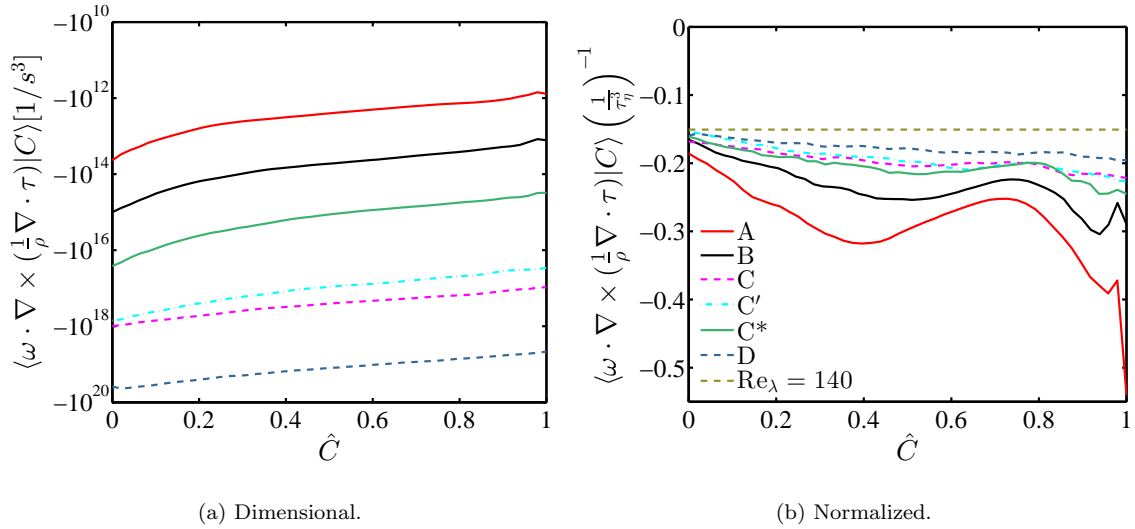
(b) Normalized.

Figure 5.8: Viscous dissipation term in dimensional and normalized form. The line $\text{Re}_\lambda$ is calculated from the previous simulations of homogeneous, isotropic turbulence by Carroll and Blanquart [11].

## 5.1.5 Viscous dissipation

Viscous dissipation, like vortex stretching, is present in constant density flow. In dimensional form, it can vary by nearly two orders of magnitude across the flame and it varies by many orders of magnitude between the cases tested (Fig. 5.8a). The primary component of viscous dissipation, $\nabla \times ((\nabla \cdot \tau)/\rho)$, by considering dimensional analysis scales as $\nu u/l^3$. Given a Kolmogorov turbulent cascade, this is again largest for the smallest scales of turbulence resulting in the scaling,

$$\langle \nabla \times \left( \frac{1}{\rho} \nabla \cdot \tau \right) |C\rangle \propto \frac{1}{\tau_\eta^2}. \tag{5.11}$$

As with several quantities discussed prior, in the case of high $Ka$, viscous dissipation scales with the turbulent quantities, specifically,

$$\langle \boldsymbol{\omega} \cdot \nabla \times \left( \frac{1}{\rho} \nabla \cdot \tau \right) |C\rangle \propto \frac{1}{\tau_\eta^3}. \tag{5.12}$$

In the high Reynolds number limit of homogeneous, isotropic turbulence, Tennekes and Lumley [112] propose a similar scaling.

Normalized according to the above expression, viscous dissipation obtains a fairly constant value through the flame and across conditions (Fig. 5.8b). As $Ka_u$ increases between cases A, B, and C*, the variation in the normalized quantity decreases. This suggests that the normalization better characterizes the behavior of this term as the Karlovitz number increases, which aligns with the chosen normalization representing the high $Ka$ limit. Additionally, the constant tends toward the value obtained for homogeneous, isotropic turbulence as $Ka_u$ increases.

## 5.1.6 Forcing term

In dimensional form, the forcing term varies by several orders of magnitude between the cases tested (Fig. 5.9a). Assuming the TKE is everywhere equal to the imposed value, $k_o$, the forcing term is identically $A\omega^2$. As stated in section 4.1.3, $A$ is equal to $A = (2\tau_o)^{-1}$ and is imposed as a parameter

(a) Dimensional.  (b) Normalized.
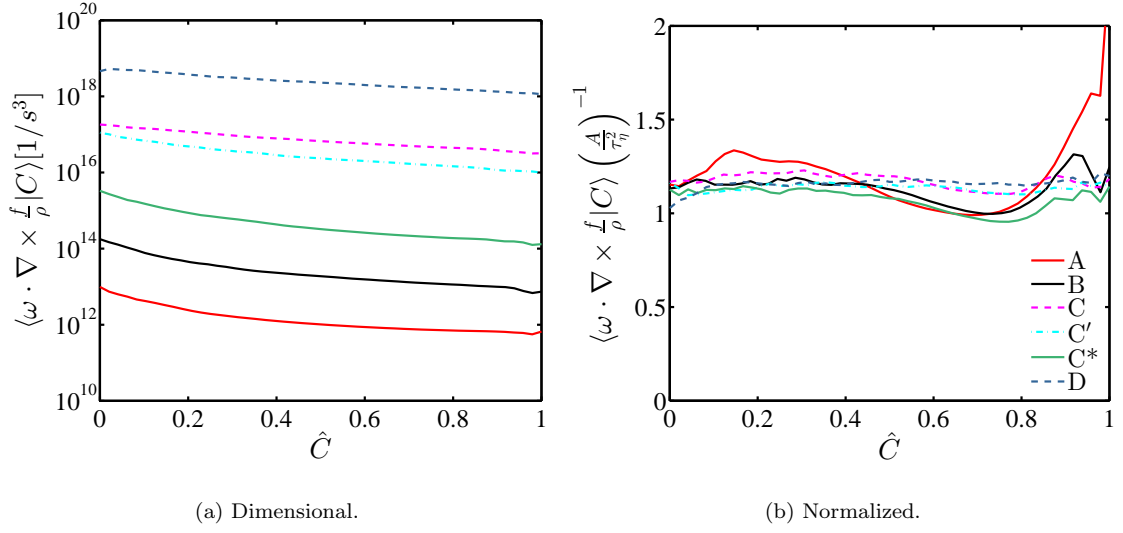
Figure 5.9: Forcing term in dimensional and normalized form.

of the simulation. Therefore, the forcing term scales as

$$\langle \boldsymbol{\omega} \cdot \nabla \times \left( \frac{\boldsymbol{f}}{\rho} \right) | C \rangle \propto \frac{1}{2\tau_o \tau_\eta^2}. \tag{5.13}$$

Normalized in this manner, the forcing term obtains a nearly constant value through the flame and across conditions (Fig. 5.9b). It is observed that the normalized forcing term has less variation as the Karlovitz number increases.

## 5.1.7 Normalized enstrophy transport equation

The above scaling estimates are used to propose a normalization of the entire enstrophy transport equation, which is then given by,

$$\frac{1}{2} \frac{D\hat{\omega}^2}{D\hat{t}} = Ka\hat{T}_1 + \gamma \hat{T}_2 + \alpha\gamma\sqrt{Ka}\hat{T}_3 + Ka\hat{T}_4 + \frac{1}{2Da}\hat{T}_5, \tag{5.14}$$

where $\hat{t} = t/\tau_F$, $\hat{\omega}^2 = \langle \omega^2 | C \rangle \tau_\eta^2$, and the Damköhler number is $Da = \tau_o/\tau_F$. Again, $Ka$ is the local Karlovitz number, $Ka(C)$. As written above, $\hat{T}_1$ is vortex stretching, $\hat{T}_2$ is dilatation, $\hat{T}_3$ is baroclinic torque, $\hat{T}_4$ is viscous dissipation, and $\hat{T}_5$ is the forcing with each component normalized
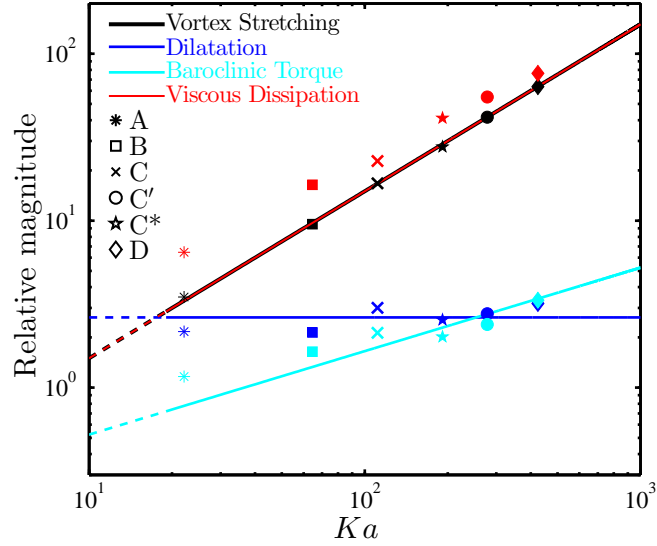
Figure 5.10: Theoretical values and numerical results for the relative magnitude of terms in the enstrophy transport equation. Lines are calculated from Eq. 5.14 using the parameters ($\alpha$ and $\gamma$) of case B. Symbols represent simulation results evaluated at $\hat{C} = 0.5$ with $\alpha$ and $\gamma$ scaled to match conditions.

according to the above discussion. The form of these terms are written explicitly in B. The preceding analysis in this section shows that the normalized terms obtain nearly constant values (or a constant peak value) through the flame and across conditions with $\hat{T}_1 \simeq 0.15$, $0 < \hat{T}_2 \lesssim 0.7$, $0 < \hat{T}_3 \lesssim 0.1$, $-0.3 < \hat{T}_4 < -0.15$, and $\hat{T}_5 \simeq 1$, which are shown to be valid at high $Ka_u$. Equation 5.14 is not intended to be precisely solved for enstrophy transport, but provides the scaling and approximate magnitude of each term. It also represents the local balance of vortex stretching, viscous dissipation, and forcing in the present high $Ka_u$ cases, as shown in Fig. 5.1.

The scaling in Eq. 5.14 suggests that as the Karlovitz number increases, vortex stretching and dissipation increase in magnitude relative to baroclinic torque, dilatation, and forcing. This is consistent with the observed relative decrease of baroclinic torque and dilatation as $Ka$ increased in the results of Hamlington *et al.* [38]. It is also consistent with the behavior observed at low $Ka_u$ where baroclinic torque and dilation contribute significantly to the transport of vorticity [59]. Going further, Eq. 5.14 may be used to predict the relative magnitude of vortex stretching, dilatation, baroclinic torque, and viscous dissipation as a function of the Karlovitz number (Fig. 5.10). It is important to stress that these predictions are only accurate when the proposed scaling is valid, *i.e.*

at high Karlovitz numbers. Thus, dashed lines in Fig. 5.10 are used to reflect the uncertainty in extrapolating below the lowest value of $Ka$ tested in this work. Lines in Fig. 5.10 are calculated using $\alpha$ and $\gamma$ from the results of case B evaluated at $\hat{C} = 0.5$, which is near the location of peak dilatation and baroclinic torque. Symbols represent the simulation results with each term again evaluated at $\hat{C}$=0.5. The numerical and theoretical values show good agreement, and this agreement improves as the Karlovitz number increases. Using these results, vortex stretching and viscous dissipation are both predicted to be larger than dilatation and baroclinic torque when $Ka \gtrsim 20$. This value of the Karlovitz number was calculated using $\alpha$ and $\gamma$ from case B, and will vary slightly with different reactant conditions. Sufficiently above this value of $Ka$, it is predicted that vortex stretching and dissipation dominate the transport of enstrophy.

## 5.1.8  Summary

In the limit of high $Ka$, enstrophy transport results in a local balance between production and dissipation. This is also the case for homogeneous, isotropic turbulence [111, 112]. This confirms theoretically the hypothesis that, in high $Ka$ premixed flames, the mean enstrophy behaves locally in a similar manner to constant density, homogeneous, isotropic turbulence. This implies that enstrophy should scale with the Kolmogorov time scale, which is confirmed in Fig. 5.11, with a proportionality constant close to unity. From homogeneous, isotropic turbulence it can be shown that

$$\bar{\epsilon} = 15\nu \overline{\left(\frac{\partial u}{\partial x}\right)^2}, \tag{5.15}$$

as well as

$$\overline{\omega^2} = 15 \overline{\left(\frac{\partial u}{\partial x}\right)^2}, \tag{5.16}$$

so that a normalized value of unity is expected [87]. Variations in the normalized enstrophy decrease as the Karlovitz number increases, which is expected as the normalizations are chosen for the limit of high $Ka$. Therefore, for sufficiently high $Ka_u$, the mean enstrophy has the same value as in homogeneous, isotropic turbulence given the local $\epsilon$ and $\nu$. This demonstrates that it is the change

(a) Dimensional.　　　　　　　　　　　(b) Normalized.
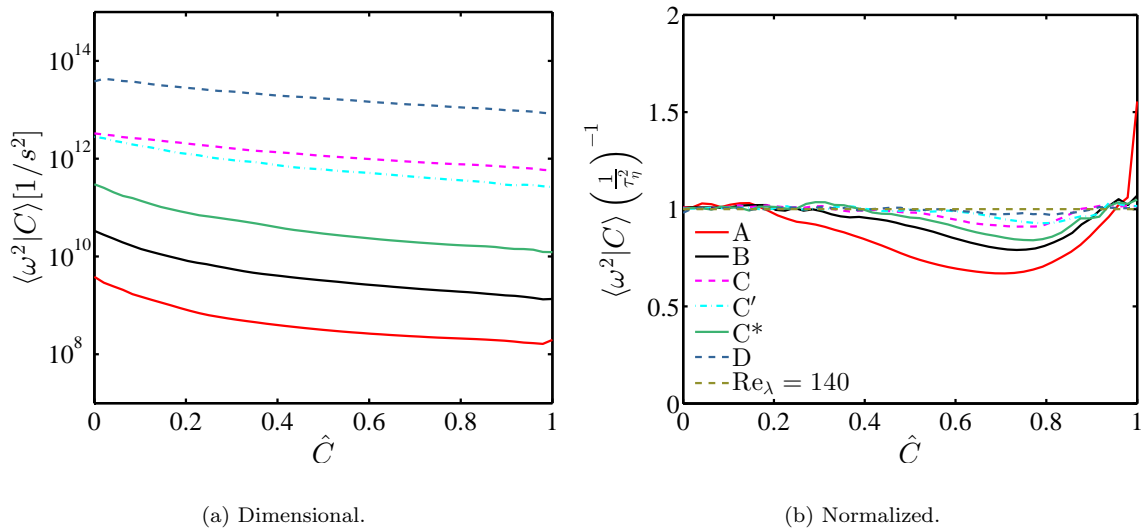
Figure 5.11: Enstrophy in dimensional and normalized form. In normalized form, enstrophy has less variation through the flame as the Karlovitz number increases. The line $\text{Re}_\lambda$ is calculated from the previous simulations of homogeneous, isotropic turbulence by Carroll and Blanquart [11].

in kinematic viscosity, as opposed to the effect of the density change through dilatation and baroclinic torque, which drives the enstrophy transformation through the flame.

These results shed light on the validity of Kolmogorov's first similarity hypothesis within premixed flames, since enstrophy is characteristic of the smallest turbulent scales. Though the fluid properties and turbulence characteristics vary widely across the flame and between the present cases, enstrophy is found to vary only as a function of $\tau_\eta$, or equivalently $\nu$ and $\epsilon$ alone. This supports that Kolmogorov's first similarity hypothesis is valid for sufficiently high Karlovitz number premixed flames. In contrast, this result suggests that Kolmogorov's first similarity hypothesis may not be valid for low $Ka_u$ premixed flames, but remains to be confirmed. While aspects of these results may not be surprising, high $Ka_u$ behavior is found to be fundamentally different than low $Ka_u$ behavior. For example, Kolla $et\ al.$ [52] performing DNS of low Karlovitz number flames show a collapse of the viscous scales in the TKE spectrum when normalizing using the flame thickness. At low $Ka$, the impact of the flame is more than to simply increase the viscosity, which is the primary effect in high $Ka$ flames, as demonstrated here.

## 5.2 Model testing

The above conclusions are obtained using finite-rate chemistry and non-unity Lewis numbers. Turbulent combustion research often employs other chemical and transport models. In this section, the effects of chemical and transport models on the conclusions of this work are tested. Case B is chosen for these tests as the Karlovitz number is high enough such that substantial flame broadening and chemical source term variation occurs, but low enough such that differential diffusion effects are not eliminated [101, 103, 102] providing a rigorous test case for both transport and chemical models.

### 5.2.1 Effects of unity-Lewis number assumption

To test the effects of transport models, case B is repeated setting all Lewis numbers to unity, which is referred to as case $B_1$. These two cases are compared primarily to investigate changes in the mean enstrophy, as this study focuses on the transport of this quantity.

Figure 5.12a and b show that varying the transport model has negligible effects on the dimensional and normalized mean enstrophy. The agreement between cases B and $B_1$ can be understood by considering the vortex stretching and viscous dissipation terms. Figure 5.12c shows that vortex stretching is nearly identical between cases B and $B_1$; similar agreement is found for viscous dissipation. As vortex stretching and viscous dissipation dominate the transport of enstrophy at high Karlovitz number, the mean enstrophy evolves similarly in the two cases. Good agreement is also observed in the remaining terms, such as dilatation (Fig. 5.12d). These results suggest that, at high Karlovitz number, the transport model has negligible effects on the smallest turbulent scales. This is in contrast to the importance of the transport model in representing the effects of the turbulence on the flame. For example, Savard and Blanquart [102] found that with non-unity $Le$ transport (compared with unity $Le$ transport) the fuel chemical consumption rate in case B exhibited more local extinctions and its mean value was reduced by 40%. This variation in the fuel source term was found to significantly reduce the turbulent flame speed ($S_T/S_L$) compared to the unity $Le$ flame. While the transport model may affect quantities central to flame propagation, the resulting impact on the mean enstrophy is found here to be negligible. It is important to note that this analysis is

(a) Dimensional enstrophy.

(b) Normalized enstrophy.

(c) Dimensional vortex stretching.

(d) Dimensional dilatation.
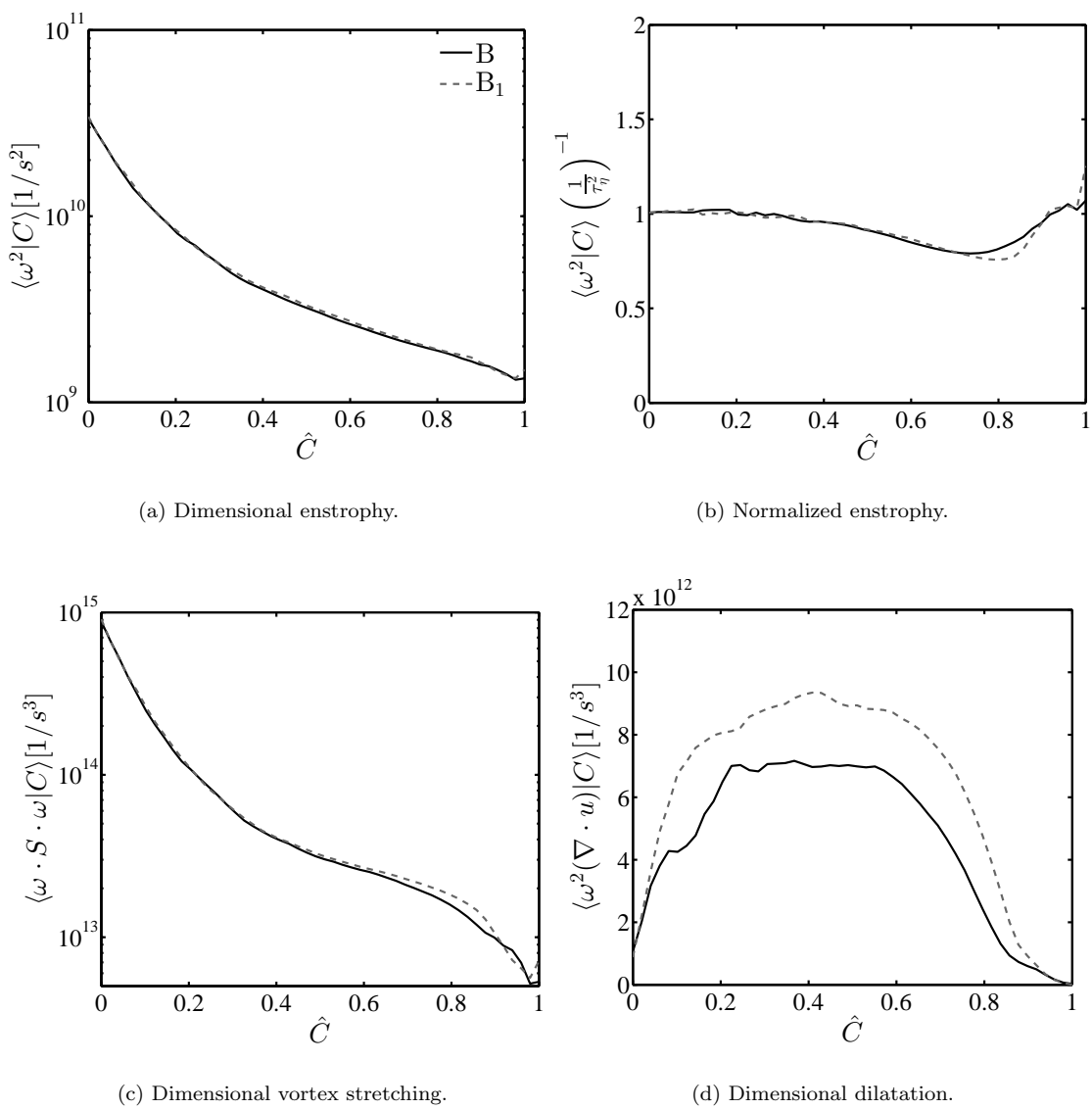
Figure 5.12: Comparison of case B with constant non-unity (B) and unity Lewis numbers ($B_1$).

in the absence of thermo-diffusive instabilities, and these results may not extend to flames, such as lean hydrogen/air, where these instabilities occur.

## 5.2.2 Effect of chemical models

To investigate the implications of chemical models, case $B_1$ is repeated using two alternative chemical mechanisms: one-step ($B_{OS,1}$) and tabulated chemistry ($B_{Tab,1}$). These models are introduced in sections 2.2.3 and 2.2.2, respectively. In order to focus on the effects of the chemical model, unity Lewis numbers are used in all three simulations in order to eliminate effects due to differences in the transport models.

Using one-step chemistry, only the reactants and products, $n$-$C_7H_{16}$, $O_2$, $H_2O$, and $CO_2$, are transported. The chemical source terms are determined through a single irreversible, one-step reaction (Eq. 2.15). The rate constant, $A$, and activation temperature, $T_a$, are chosen so that the 1D unstretched laminar flame speed and thickness closely match that of the finite-rate mechanism ($A = 6.0 \times 10^9 \text{ m}^3/\text{kg s}$ and $T_a = 15,000\text{K}$). As this model excludes intermediate species, the progress variable is defined as the sum of the chemical product mass fractions, $C = Y_{H_2O} + Y_{CO_2}$. One-step chemistry requires less computation resources compared to finite-rate chemistry as fewer species must be transported.

Using flamelet generated manifolds (FGM), or tabulated chemistry, the flame is modeled through a single progress variable, $C$, with which fluid properties and the chemical source term are tabulated [51, 33, 116, 91]. Tabulation is performed using the 1D unstretched flame solution of the finite-rate chemical model obtained using FlameMaster [81]. Once again, the progress variable is defined as the sum of $H_2O$, $H_2$, $CO_2$, and $CO$ mass fractions and its transport is governed by Eq. 2.13. The use of tabulated chemistry relaxes the computational cost compared to finite-rate chemistry as a single scalar must be transported. Time integration of the chemical source terms is performed explicitly for tabulated and one-step chemistry.

The results obtained with each model are compared primarily through the mean enstrophy as, again, the transport of enstrophy is the focus of this study. Figures 5.13a and b show that the

(a) Dimensional enstrophy.

(b) Normalized enstrophy.

(c) Dimensional vortex stretching.

(d) Dimensional dilatation.
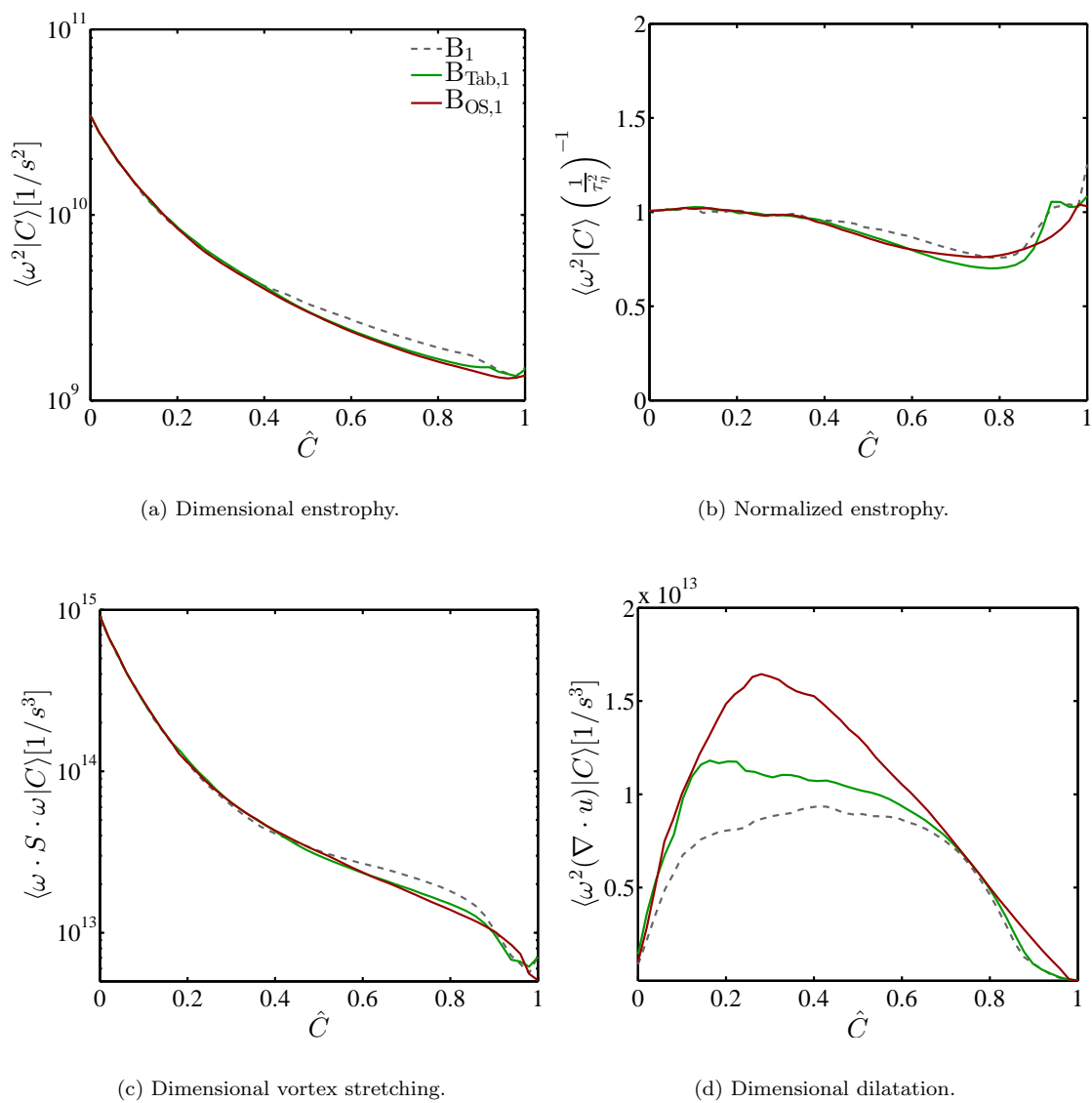
Figure 5.13: Comparison of case $B_1$ with finite-rate, tabulated, and one-step chemistry.

chemical models induce little differences in the dimensional and normalized mean enstrophy. This is again explained by the agreement of vortex stretching (Fig. 5.13c) and dissipation among the chemical models, which control the transport of enstrophy in high $Ka$ premixed flames. As one-step has a slightly different definition of $C$ and value of $C_{max}$, a small shift in the curves in $\hat{C}$ space and differences near $\hat{C} = 1$ are expected. A greater effect is observed for the dilatation (Fig. 5.13d) and baroclinic torque terms with one-step chemistry, though this has negligible effects in the transport of enstrophy as their magnitude is small relative to vortex stretching and viscous dissipation. The agreement observed in the mean enstrophy further emphasizes that the smallest turbulent scales evolve through the flame with the local fluid properties, independent of the tested transport or chemical models.

## 5.3   Results extension

In this section, the above results are compared with a higher Reynolds number simulation and the recent slot Bunsen flames of Sankaran *et al.* [99], demonstrating the applicability of the present conclusions to these alternative configurations.

### 5.3.1   Higher Reynolds numbers

While this study considers a wide range of Karlovitz numbers, the integral length scale in each DNS discussed thus far is limited to approximately the flame thickness. It is important to consider whether these results are applicable to larger values of $l_o/l_F$, or equivalently, larger Reynolds numbers. This is investigated, first, theoretically through the vorticity spectrum, $\Omega(\kappa)$ and, second, practically through an additional DNS with a larger integral length scale.

In the present low $Re$ DNS, all the entrophy is contained in scales smaller than the flame thickness. For a larger $Re$, the portion of enstrophy contained in scales smaller than the flame thickness may be determined by considering the model spectrum of Pope for the high $Re$ limit [87],

$$E(\kappa) = 1.5\epsilon^{2/3}\kappa^{-5/3}\left(\frac{\kappa l_o}{[(\kappa l_o)^2 + 6.78]^{1/2}}\right)^{11/3}\exp\left[-5.2\left([(\kappa\eta)^4 + 0.4^4]^{1/4} - 0.4\right)\right], \qquad (5.17)$$

(a) case B$_{\text{Tab},1}$



(b) case B$^4_{\text{Tab},1}$
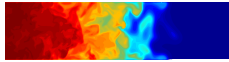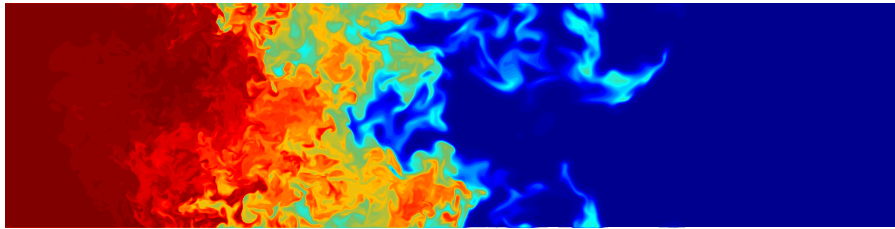
Figure 5.14: Two-dimensional slices of density from cases B$_{\text{Tab},1}$ and B$^4_{\text{Tab},1}$. Each figure represents a region of size $L \times 4L$ and both are scaled to match physical length scales.

and evaluating the vorticity spectrum as $\Omega(\kappa) = 2\kappa^2 E(\kappa)$. Using this model spectrum, the wavenumber $\kappa^*$, corresponding to $\kappa^* = 2\pi/l_F$, for which 80% of the enstrophy is contained in scales smaller than the flame thickness may be found through the integral

$$\frac{1}{\omega_u^2} \int_{\kappa^*}^{\infty} \Omega(\kappa) d\kappa = 0.8. \tag{5.18}$$

Considering an infinite $Re$, at least 80% of the enstrophy is contained in scales smaller than the flame if $l_F/\eta > 40$. This is approximately the condition of case B. Said another way, if case B had an arbitrarily large $Re$ but the same $Ka_u$, then only 20% of the enstrophy would be in scales larger than the flame thickness. In summary, any high Reynolds number turbulent flame with the same Karlovitz number of the present cases would have nearly the same fraction of vorticity contained in scales smaller than the flame. The present results should thus remain valid for larger integral to flame length scale ratios.

An additional DNS, labeled case B$^4_{\text{Tab},1}$, is performed to verify if the results are indeed independent of the Reynolds number. This simulation has the exact same conditions as case B$_{\text{Tab},1}$, but a higher Reynolds number, $Re_t = 1150$. The increase in $Re_t$ is accomplished by increasing both $L$ as well as $u'$, in order to maintain the same $Ka_u$ number, resulting in a four-fold increase in the integral

length scale ($l_o/l_F = 4$ and $u'/S_L = 33$). Figure 5.14 presents instantaneous density contour plots from $B_{Tab,1}$ and $B_{Tab,1}^4$. While still maintaining sufficient length for the turbulent flame brush, $L_x$ is set to $6.5L$ with the forcing applied between $L_x = 0.5L$ and $L_x = 4.5L$. To further minimize the computational cost, the grid is stretched in the $x$-direction near the x-outflow where the forcing is not applied. Utilizing the results of section 5.2, which found little effect of the transport and chemical models on the vorticity transformation, this much larger simulation employs tabulated chemistry with unity Lewis number transport. This, again, reduces the computational cost of the simulation (compared to finite-rate chemistry), while still retaining the physics necessary to this study. Due to the larger domain size, each data file represents significantly more independent statistical samples than case $B_{Tab,1}$. Therefore, after an initial transient, it is only necessary to collect data over $7\tau_o$.

Cases $B_{Tab,1}$ and $B_{Tab,1}^4$ are compared, as before, by considering the mean enstrophy, vortex stretching, and dilatation terms. Figure 5.15 shows that increasing the turbulent Reynolds number introduces only small changes to these quantities. Particularly, the mean enstrophy exhibits a similar variation through the flame. This agreement, along with the preceding theoretical analysis, supports that the conclusions of this chapter are independent of the turbulent Reynolds number (or equivalently the integral to flame length scale ratio). Combined with the results of section 5.2, this reinforces the primary conclusion of this chapter.

To summarize, first, the unity Lewis number case, $B_1$, has significantly less local extinction than case B [102, 55], yet there is virtually no effect observed on the behavior of the smallest turbulent scales (Fig. 5.12). Second, $B_{Tab,1}$ and $B_{OS,1}$ have entirely different chemical models and responses to straining and wrinkling. Even more, in the case of tabulated chemistry, all chemical source terms are only functions of the progress variable, and hence remain the same regardless of flow straining and flame wrinkling. Despite these difference, no effects were observed on enstrophy (Fig. 5.13). Third, case $B_{Tab,1}^4$ has a four times larger integral length scale, intentionally introducing straining and wrinkling on a much larger scale (as shown in Fig. 5.14). Yet again, virtually no effect is observed on the smallest turbulent scales (Fig. 5.15). These results support the conclusion of the thesis that, given a sufficiently high Karlovitz number, it is not the large flame dynamics which

(a) Dimensional enstrophy.

(b) Normalized enstrophy.

(c) Dimensional vortex stretching.

(d) Dimensional dilatation.
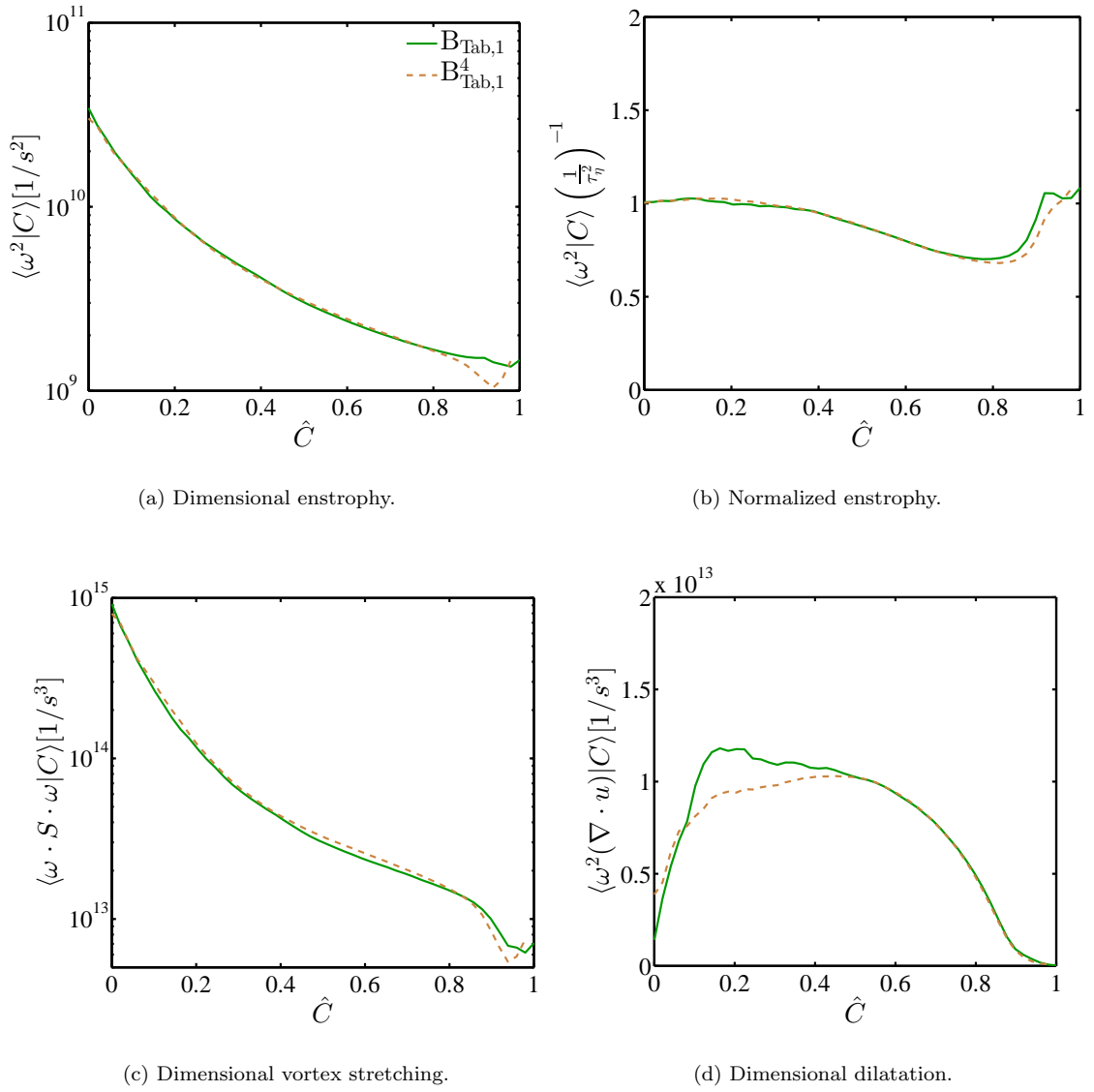
Figure 5.15: Comparison of case $B_{\text{Tab},1}$ with the case of a larger Reynolds number, $B^4_{\text{Tab},1}$.

determine the smallest turbulent scales, but only the local kinematic viscosity and dissipation rate. This is essentially a restatement of Kolmogorov's first similarity hypothesis.

## 5.3.2 Slot Bunsen flame

The simulations in the present study consider a statistically-planar flame with zero mean shear and forced turbulence. While providing a configuration favorable to fundamental study, other simulations and most practical devices operate under different conditions. To investigate the applicability of the current results and conclusions to alternative configurations, the present results are compared to the recent high Karlovitz number slot Bunsen flames of Sankaran *et al.* [99]. The reader is referred to Ref. [99] for complete details about the DNS. Only a brief overview is provided here.

Sankaran *et al.* [99] simulated preheated ($T_u$=800K) methane/air premixed slot Bunsen flames at atmospheric pressure. The slot, containing unburnt reactants, extends in the spanwise, $z$, direction and is bounded in the transverse, $y$, direction by a heated, laminar coflow of burnt products. The difference in inlet velocities between the slot and laminar coflow introduces a strong mean shear. The flame and flow spatially develop in the streamwise, $x$, direction. This configuration is illustrated in Fig. 5.16. The present comparison considers case C, which has the highest unburnt Karlovitz number and turbulent Reynolds number among their cases. To remove any confusion with our case C, case C from Sankaran *et al.* [99] is referred to as S-C in the following. The chemistry is modeled using a reduced finite rate chemical mechanism with 13 transported species and four additional species assumed in quasi-steady state. Species transport is performed with constant non-unity Lewis numbers.

Downstream of the slot, the Karlovitz number decreases along the centerline. This gives rise to different values of $Ka$ through the flame within different $y - z$ planes, as shown in Fig. 5.17. As we use a different definition of $Ka_u$ than used by Sankaran *et al.* [99], the exact numerical values are expected to be slightly different. These results are compared with the present cases A and B, as they have comparable Karlovitz numbers. In case S-C, the abrupt decrease in $Ka$ near $\hat{C} = 1$ is likely due to the laminar coflow bounding the turbulent flame. Additionally, the S-C$^{3/4}$ curve does not
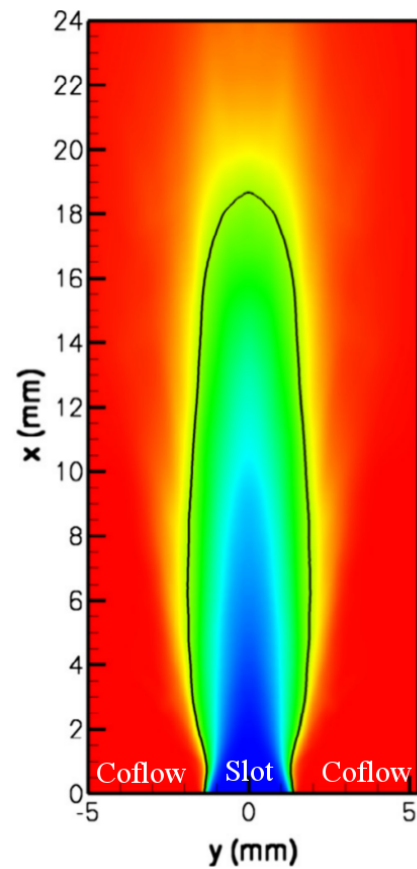
Figure 5.16: Configuration of the slot Bunsen flame performed by Sankaran *et al.* [99] and analyzed here. Plotted is the Favre averaged mean progress variable, where red denotes the products and blue denotes the reactants. The black line is the iso-contour where the Favre averaged mean progress variable equals 0.65 and represents the mean location of the flame front. Figure adapted from Ref. [99].
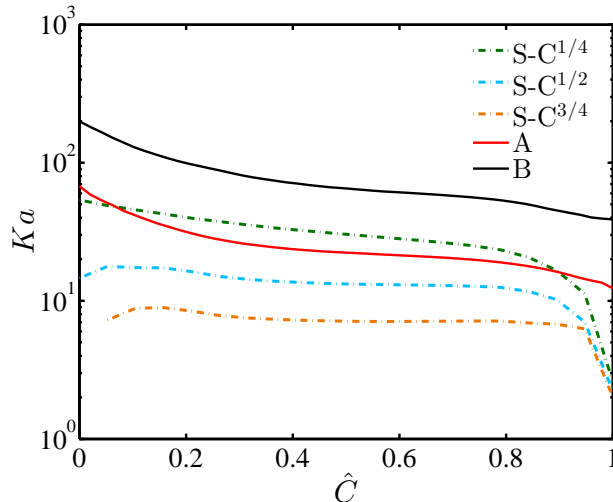
Figure 5.17: Local Karlovitz number versus $\hat{C}$ for the present cases A and B, as well as the slot Bunsen flame S-C of Sankaran *et al.* [99] at three downstream locations. For case S-C, superscripts refer to 1/4, 1/2, and 3/4 of the domain length. The progress variable is defined as the sum of $H_2O$, $H_2$, $CO_2$, and CO mass fractions.

extend to $\hat{C} = 0$ because there are no more pure unburnt reactants. The simulation results may be parameterized by two variables, one to represent the spatial progress in the $x$ direction and another for the progress through the flame. Investigating different planes in $x$ provides a similar function as varying $Ka_u$ between cases in the present configuration. Therefore, comparison is performed by analyzing the data at three $y - z$ planes, corresponding to 1/4, 1/2, and 3/4 of the domain length, denoted as S-$C^{1/4}$, S-$C^{1/2}$, and S-$C^{3/4}$, respectively. These are the same locations where Sankaran *et al.* [99] primarily report results. Quantities are then conditionally averaged on the progress variable $C$ in these individual planes to characterize the variation through the flame. The progress variable is again defined as the sum of $H_2O$, $H_2$, $CO_2$, and CO mass fractions. All quantities are computed based on the fluctuating velocity after the mean flow has been subtracted.

Once again, the normalized enstrophy is considered to test the dependence of the smallest turbulence scales on $\epsilon$ and $\nu$. Figure 5.18 shows good agreement between these two very different configurations. Most notably, the normalized enstrophy is nearly constant with values slightly below unity within the flame (Fig. 5.18a), as observed in the present forced cases. The normalized vortex stretching term is also nearly constant through the flame (Fig. 5.18b), again supporting the proposed scaling. Similar to $Ka$ in Fig. 5.17, low turbulence levels close to the products (near

(a) Normalized enstrophy.

(b) Normalized vortex stretching.
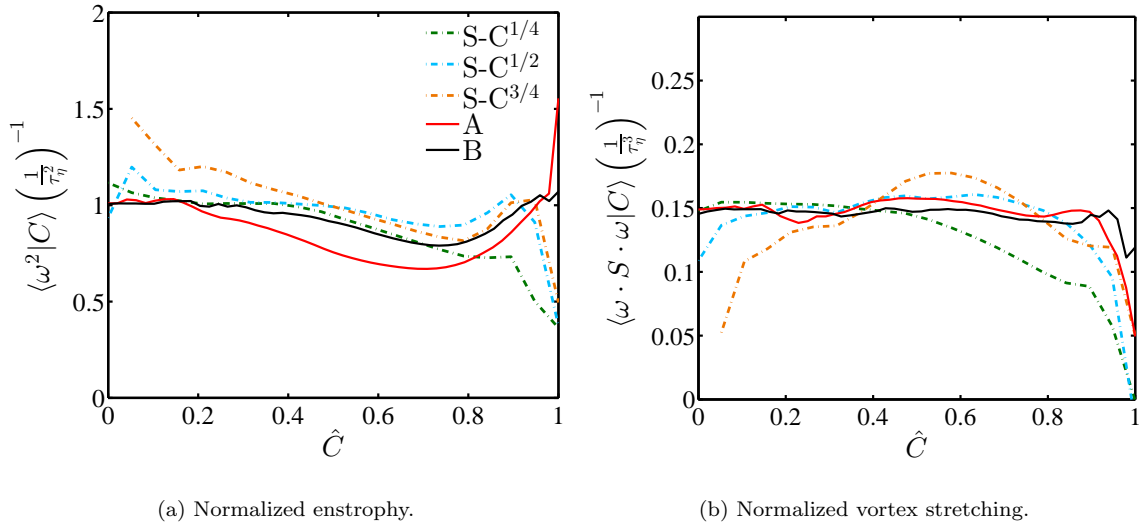
Figure 5.18: Comparison of normalized enstrophy and vortex stretching between cases A and B and the slot Bunsen flame S-C of Sankaran *et al.* [99] at three downstream locations.



(a) Enstrophy.

(b) Vortex stretching.
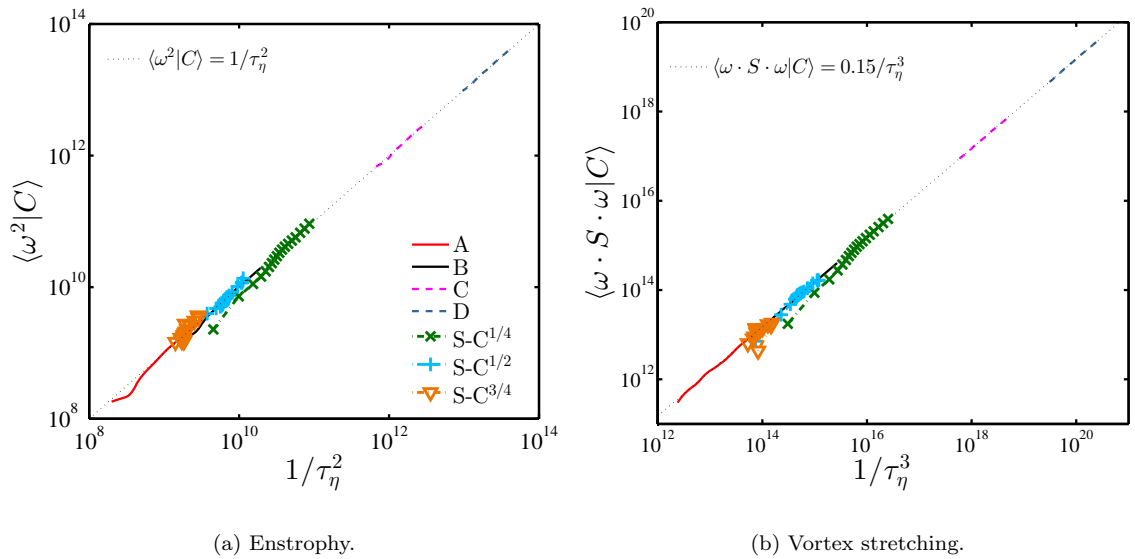
Figure 5.19: Comparison of enstrophy and vortex stretching and their respective proposed scalings for the slot Bunsen flame S-C of Sankaran *et al.* [99] as well as the present cases A, B, C, and D. Black dotted lines represent the theoretical values.

$\hat{C} = 0.9$) due to the laminar coflow may be responsible for differences in these quantities, particularly for the plane closest to the slot inlet, S-C$^{1/4}$. Additionally, the curves corresponding to the S-C$^{3/4}$ plane do not extend to $\hat{C} = 0$ as there are no pockets of unburnt reactants left.

Despite some differences in the curves shown in Fig. 5.18, the proposed scaling remains valid in the turbulent Bunsen flame. This is made clearer in Fig. 5.19 by comparing the dimensional enstrophy and vortex stretching to the expected scaling through the flame ($0.05 < \hat{C} < 0.9$). In summary, the present simulations and the results from the slot Bunsen flame of Sankaran *et al.* [99] follow the proposed scalings, and no effects of the physical configuration could be identified.

## 5.4   Correspondence to vortex-flame interaction

The conclusions of this chapter may be qualitatively compared with the 2D vortex-flame interaction discussed in chapter 3.

In high Karlovitz number flames, the smallest turbulent scales (where most of the vorticity is located) are much smaller than the flame thickness ($\eta \ll l_F$). The corresponding representative 2D vortex is a small vortex ($l_v \ll l_F$). In chapter 3, it was found that such a vortex is dominated by viscous effects, given by the ratio of $\tau_2/\tau_4$ in Eq. 3.5. In the current chapter, it is also found that viscous effects dominate over baroclinic torque and dilatation in the limit of high Karlovitz number. More specifically, viscous effects were shown in this chapter to scale with the Karlovitz number, which (by defining $a \equiv S_L l_F/\nu$) may be rewritten as $Ka = (l_F/\eta)^2/a$. Comparison with Eq. 3.5, $\tau_2/\tau_4 = (l_F/l_v)^2/a$, reveals that there is a similar scaling for the importance of viscous effects in the vortex and turbulence cases.

However, the vortex stretching/production term was not present in the 2D vortex-flame interaction. This term, in addition to viscous dissipation, was found to be critical to the transport of enstrophy. In the turbulent case, vortex stretching/production term balances viscous dissipation, which does not occur with a 2D vortex.

In contrast, at low Karlovitz numbers, the smallest turbulent scales are larger and slower than the flame ($\eta \gg l_F$, $u_\eta \ll S_L$). This condition corresponds to a large-slow 2D vortex. In the

present chapter, dilatation and baroclinic torque were found to increase in relative magnitude as the Karlovitz number decreases. Furthermore, dilatation and baroclinic torque were found in a previous study at low Karlovitz numbers to contribute significantly to the transport of vorticity [59]. In chapter 3, the corresponding large-slow vortex was also found to be dominated by baroclinic torque. Though not pursued in this thesis, further comparison of these cases could help shed light on the mechanisms controlling the production of baroclinic torque in turbulent combustion.

## 5.5   Summary and conclusions

The primary goal of the present chapter was to understand the changes in the smallest turbulent scales within a high Karlovitz number turbulent premixed flame brush via the study of the mean enstrophy. For this purpose, the series of high Karlovitz number direct numerical simulations described in chapter 4 were analyzed and which spanned a wide range of Karlovitz numbers and flame density ratios. These simulations of $n$-heptane/air premixed flames employed a reduced finite-rate chemical mechanism and non-unity Lewis number transport. Using the DNS results, a theoretical scaling analysis was performed to estimate the magnitude of each term in the enstrophy transport equation. As a result, a normalized enstrophy transport equation was proposed for high Karlovitz numbers. Several conclusions are as follows.

The proposed normalized enstrophy transport equation involves a small set of parameters so that the relative magnitude of vortex stretching, dilatation, baroclinic torque, and viscous dissipation may be predicted as a function of the Karlovitz number and flame conditions.

In the limit of high $Ka$, vortex stretching and viscous dissipation dominate the behavior of enstrophy. A balance of these two terms is also observed in homogeneous, isotropic turbulence. As a consequence, given a sufficiently high $Ka$, the mean enstrophy scales in the same manner as homogeneous, isotropic turbulence, namely with the inverse of the Kolmogorov time scale squared, $1/\tau_\eta^2$. Therefore, for sufficiently high $Ka_u$, the mean enstrophy obtains the same value as in homogeneous, isotropic turbulence given the local $\epsilon$ and $\nu$. These conclusions were found to be independent of the Reynolds number and the physical configuration (*i.e.* forced or unforced).

As $\tau_\eta$ is only a function of $\epsilon$ and $\nu$, this conclusion supports the validity of Kolmogorov's first similarity hypothesis in high $Ka$ premixed flames. In contrast, this suggests that in moderate to low $Ka$ flames this hypothesis may not be valid and different characteristics of the turbulence through the flame are expected. The following chapter will address the validity of the Kolmogorov's hypothesis of local isotropy in high Karlovitz number premixed flames.

Several additional DNS were performed and analyzed with alternative transport and chemical models to test their effects on the transformation of enstrophy. It was found that unity Lewis number transport provided sufficient detail of the flame structure to capture the relevant effects of the flame on turbulence. Additionally, simulations using one-step and tabulated chemistry captured the behavior of the mean enstrophy. This suggests that future research studying the effects of the flame on turbulence at high Karlovitz number does not need to include details of finite-rate chemistry and differential diffusion in numerical simulations to accurately capture the behavior of the smallest turbulent scales.

# Chapter 6

# Vorticity isotropy[1]

In the previous chapter, the validity of Kolmogorov's first similarity hypothesis was addressed in high Karlovitz number ($Ka$) turbulent premixed flames by considering enstrophy. The current chapter investigates the isotropy of the small scale turbulence through the vorticity vector, which relates to Kolmogorov's hypothesis of local isotropy. The source of anisotropy is then investigated through the vorticity transport equation, which is followed by an analysis of how different parameters (such as $Ka_u$ and $l/l_F$) impact small scale anisotropy.

For the sake of clarity, only cases A, B, $B_{\mathrm{Tab},1}$, $B^4_{\mathrm{Tab},1}$, C*, and D (presented in chapter 4) are considered here. Between the cases considered in this chapter, the turbulence intensity, $l_o/l_F$, and the unburnt temperature are varied in order to investigate the effects of the unburnt Karlovitz number, largest turbulent length scales, and flame density ratio. Case $B_{\mathrm{Tab},1}$ has the same conditions as case B and is provided to test the impact of unity Lewis number transport and tabulated chemistry on the behavior of small scale isotropy.

The chapter is organized as follows. Section 6.1 presents an analysis addressing the presence of small scale isotropy followed by an investigation of the vorticity equation to identify the specific term primarily responsible for the production of anisotropy. Section 6.2.1 then presents a further analysis of the impact of different parameters on anisotropy. The correspondence between this chapters results and the vortex-flame interaction is discussed in section 6.3. Lastly, a discussion of the conclusions and their application is provided in section 6.4.

---

[1]This chapter is based in large part on the publication [7]: Brock Bobbitt and Guillaume Blanquart. Vorticity anisotropy in high Karlovitz number premixed flames. *Phys. Fluids*, (To be submitted).

## 6.1 Vorticity isotropy

In this section, the presence of small scale isotropy is investigated in the high Karlovitz number premixed flames. The vorticity transport equation is then analyzed to isolate the term (or terms) primarily responsible for the production of anisotropy.

### 6.1.1 Isotropy

If the smallest turbulent scales are isotropic, then the vorticity vector components are statistically equal in a fixed Galilean coordinate system. As the present configuration is statistically one-dimensional in $x$, and periodic in $y$ and $z$, an orthogonal coordinate system aligned with $x$ best characterizes any anisotropy resulting from the flame. Furthermore, as a result of the symmetry in $y$ and $z$, any differences between the two corresponding vector components would be due to statistical uncertainty.

Using this domain fixed coordinate system, isotropy of the vorticity vector is assessed by considering a vector, $\boldsymbol{W}$, defined here as the square of each vorticity component less one-third of the enstrophy,

$$W_i = \omega_i^2 - \frac{\omega^2}{3}. \tag{6.1}$$

Subsequently, $\boldsymbol{W}$ will be referred to as the anisotropy vector. Figure 6.1 presents $W_x$ conditionally averaged on the progress variable. Once again, any deviations from zero are signs of anisotropy. As a result of the symmetry in $y$ and $z$, $\langle \omega_y^2 | C \rangle$ is equal to $\langle \omega_z^2 | C \rangle$. Therefore, the components in Eq. 6.1 may be rewritten as

$$\langle W_x | C \rangle = \frac{2}{3} \langle \omega_x^2 | C \rangle - \frac{2}{3} \langle \omega_y^2 | C \rangle, \tag{6.2}$$

$$\langle W_y | C \rangle = \frac{1}{3} \langle \omega_y^2 | C \rangle - \frac{1}{3} \langle \omega_x^2 | C \rangle. \tag{6.3}$$

From this, $\langle W_y | C \rangle$ and $\langle W_z | C \rangle$ are equal to $-\langle W_x | C \rangle / 2$, so that their values may be inferred based on $\langle W_x | C \rangle$ provided in Fig. 6.1.
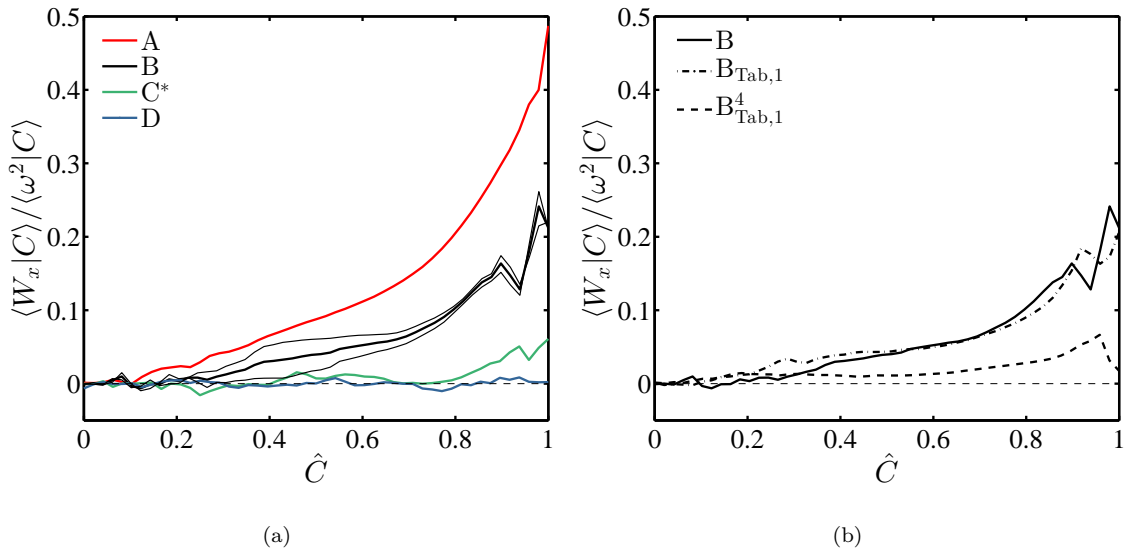
Figure 6.1: The anisotropy vector in the $x$ direction, $W_x$, for cases (a) A, B, C*, and D; as well as (b) B, $B_{\text{Tab},1}$, $B^4_{\text{Tab},1}$. Dashed line at zero represents perfect isotropy. $W_x$ is normalized by the conditionally averaged enstrophy. In (a), thin black lines correspond to averages for case B when either the first or second half of the data is used; they are indicative of the statistical uncertainty in the computed averages.

Near the reactants ($\hat{C} \simeq 0$), vorticity is isotropic for all flames. This is simply because the reactants are initialized with homogeneous isotropic turbulence. Consider first cases A, B, and C* (Fig. 6.1a). As the turbulence enters the preheat zone, anisotropy begins to develop in case A, and to a lesser extent in case B. The anisotropy is characterized by a larger vorticity in the direction of the mean flow ($x$ direction) than in the plane of the time-averaged flame ($y$ and $z$ directions). The degree of anisotropy in both cases continues to increase toward the products. In case C*, discernible levels of anisotropy only develop later in the flame. Finally, for case D, with a similar $Ka_u$, but lower flame density ratio compared to case C*, the anisotropy is negligible throughout the flame.

Between cases A, B, and C*, the unburnt Karlovitz number increases by an order of magnitude, yet the ratio of the integral length scale to flame thickness remains close to unity. In contrast, cases B and $B^4_{\text{Tab},1}$ have the same Karlovitz number, but different integral length scales ($l_o/l_F$=1 and 4 respectively). Equivalently, they also have different turbulent Reynolds numbers ($Re_{t,u}$=190 and 1150, respectively) since the Karlovitz number, turbulent Reynolds number, and length scale ratio

are not independent:

$$Re_{t,u} = \left(\frac{l}{l_F}\right)^{4/3} (Ka_u^*)^{2/3}. \tag{6.4}$$

As shown in Fig. 6.1b, the vorticity in $B_{\text{Tab},1}^4$ is more isotropic than case B throughout the flame. (Note that there is very good agreement between cases B and $B_{\text{Tab},1}$, supporting the independence of the observed behavior from the chemical and transport model.)

In summary, at a sufficiently large Karlovitz number and $l/l_F$, the smallest turbulent scales are found to be isotropic, as defined by Eq. 6.1. Additionally, isotropy is promoted by lower flame density ratios. This is exemplified in case D, which shows no anisotropy throughout the flame. The dependence of small scale anisotropy on the large turbulent scales is somewhat surprising given they were found to have virtually no impact on the enstrophy (chapter 5). The impact of these parameters on the anisotropy will be further discussed in section 6.2.

Hamlington *et al.* [38] observed that the probability density function (PDF) of the vorticity component in the mean flow direction ($x$ direction) resembled isotropic conditions at large turbulence intensities (defined as $u'/S_L$). Their results are consistent with the decreasing vorticity anisotropy as observed in Fig. 6.1a with increasing $Ka_u$. However, Hamlington *et al.* [38] observed the onset of isotropy at significantly lower Karlovitz numbers than in the current study. Considering similar density ratios, their case F4 ($Ka_u = 57$, calculated assuming $Sc = 1$, where $Sc = \nu/D$) demonstrated negligible anisotropy, while the present case B ($Ka_u = 220$) has significant anisotropy. The reason for this difference is addressed in section 6.4.

## 6.1.2 Transport equation

The source of anisotropy is determined by considering the transport equation for vorticity derived from the momentum equation,

$$\frac{D\boldsymbol{\omega}}{Dt} = S \cdot \boldsymbol{\omega} - \boldsymbol{\omega} \left(\nabla \cdot \boldsymbol{u}\right) + \frac{1}{\rho^2} \left(\nabla\rho \times \nabla P\right) + \nabla \times \left(\frac{1}{\rho}\nabla \cdot \tau\right) + \nabla \times \frac{\boldsymbol{f}}{\rho}. \tag{6.5}$$

Equation 6.5 represents a set of three equations, one for each component of the vorticity vector. Analogous to the enstrophy transport equation (Eq. 5.1), each term on the right hand side is associated with a specific physical process: production/vortex stretching, dilatation, baroclinic torque, viscous dissipation, and forcing, respectively. Vortex stretching, viscous dissipation, and forcing are active even when density is constant, while dilatation and baroclinic torque arise here only due to the presence of the flame. The enstrophy transport equation is obtained by taking the dot product of vorticity with this set of equations.

From Eq. 6.5, we derive the transport equation for the anisotropy vector, $\boldsymbol{W}$. This is accomplished by multiplying each component of the vorticity transport equation by its respective vorticity component, then subtracting one-third of the enstrophy transport equation and grouping corresponding terms,

$$\frac{1}{2}\frac{D\boldsymbol{W}}{Dt} = \boldsymbol{A}_1 + \boldsymbol{A}_2 + \boldsymbol{A}_3 + \boldsymbol{A}_4 + \boldsymbol{A}_5. \tag{6.6}$$

Terms are again ordered as in Eq. 6.5 and the explicit form of each is provided in Appendix C. In the remainder of this work, these terms will be referred to as the anisotropic transport terms. For example, $A_{1,x}$ is the anisotropic vortex stretching term in the $x$ direction. To disrupt the base isotropic flow, the flame must alter the behavior of at least one term in Eq. 6.6 in order to produce anisotropy. The flame directly alters these terms through changes in the velocity divergence, fluid properties (such as $\rho$ and $\mu$), and mean gradients of turbulence quantities (such as the mean velocity). The dilatation and forcing terms are addressed first.

The anisotropic dilatation term may be written analytically as

$$\boldsymbol{A}_2 = (-\boldsymbol{W})(\nabla \cdot \boldsymbol{u}). \tag{6.7}$$

In other words, this term is a function of the velocity divergence and depends linearly on $\boldsymbol{W}$. In the absence of anisotropy, this term is identically zero. Thus, this term cannot be responsible for the initial production of vorticity anisotropy. Furthermore, dilatation is expected to decrease the magnitude of $\boldsymbol{W}$ since fluid expansion from heat release results in a positive divergence of velocity.
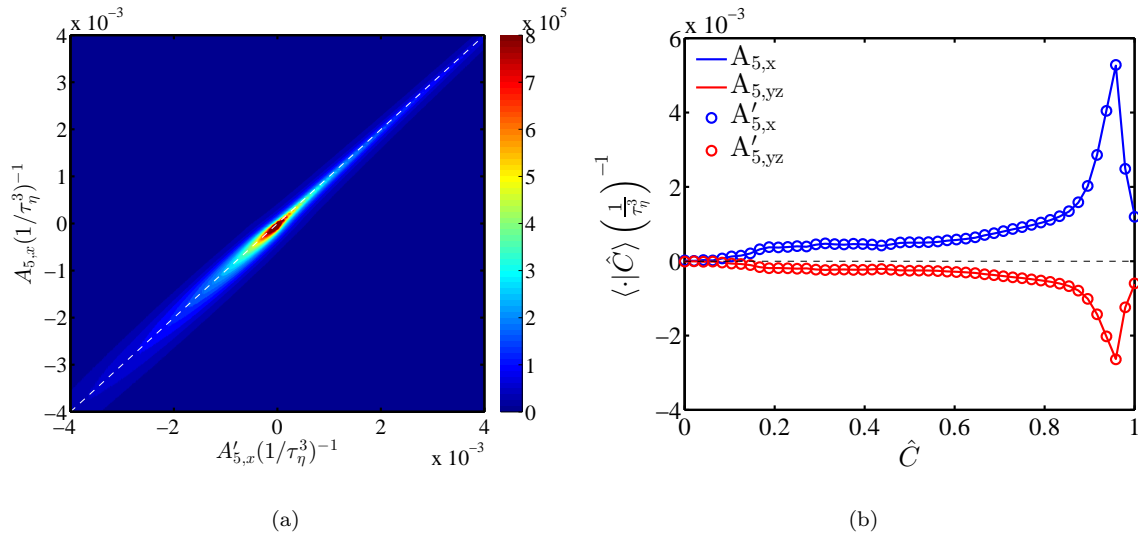
Figure 6.2: Comparison of exact versus approximate anisotropic forcing term for case $B^4_{\text{Tab},1}$ through the (a) joint PDF at $\hat{C} = 0.75$ and (b) conditional average of $A_{5,x}$ and $A'_{5,x}$. Both quantities are normalized by $1/\tau^3_\eta$. In (a) the dashed line represents perfect equality between $A_{5,x}$ and $A'_{5,x}$, and in (b) the dashed line at zero represents no anisotropy production.

In conclusion, this term cannot initiate or increase anisotropy, and will not be further considered as the possible source of anisotropy.

By neglecting gradients of the TKE and mean velocity (*i.e.* the associated effects of the flame), the forcing term is approximated by

$$\boldsymbol{A}'_5 = A \frac{k_o}{k} \boldsymbol{W}. \tag{6.8}$$

Note that $A$ is the forcing parameter defined in Eq. 4.5. If the effects of the flame on the forcing term are small, then $\boldsymbol{A}'_5$ well approximates $\boldsymbol{A}_5$. These quantities are compared by computing the joint PDF of the instantaneous, point-wise values of $A_{5,x}$ versus $A'_{5,x}$ for case $B^4_{\text{Tab},1}$ within the flame ($\hat{C} = 0.75$). As shown in Fig. 6.2a, the effect of the flame on this term is very small locally and instantaneously. Additionally, Fig. 6.2b shows that, on average, the effects of the flame introduce a negligible contribution to the value of anisotropic forcing ($\boldsymbol{A}_5$). Similar results are found for the remaining cases. As the effects of the flame on the anisotropic forcing term are negligible, we approximate $\boldsymbol{A}_5$ as $\boldsymbol{A}'_5$. As with dilatation, this term depends linearly on $\boldsymbol{W}$ and is exactly zero when vorticity is isotropic. Therefore, the growth of anisotropy is not caused by this term, and it

will not be further considered.

By exclusion of $\boldsymbol{A}_2$ and $\boldsymbol{A}_5$, either the vortex stretching, baroclinic torque, or dissipation terms must be responsible for the development of vorticity anisotropy. To isolate the cause, their relative contribution to the development of anisotropy is investigated subsequently by considering the effect of the flame on each.

### 6.1.3    Possible sources of anisotropy

The effects of the flame on vortex stretching are isolated by considering $\boldsymbol{A}_1 = \boldsymbol{A}_1' + \boldsymbol{A}_1^F$, similar to the forcing term, where the effects of the flame are associated with $\boldsymbol{A}_1^F$. In the absence of the flame, $\boldsymbol{A}_1 = \boldsymbol{A}_1'$. The flame may alter the anisotropic vortex stretching term through the strain-rate tensor (S). The flame-induced flow strain is isolated by performing a Helmholtz (or Weyl) decomposition of the velocity field, $\boldsymbol{u} = \boldsymbol{u}^D + \boldsymbol{u}^S$. For three-dimensional vector fields, there exists a decomposition which separates the vector field into an irrotational component ($\boldsymbol{u}^D$) and a divergence free component ($\boldsymbol{u}^S$), where $\boldsymbol{u}^D = \nabla \phi$ and $\boldsymbol{u}^S = \nabla \times \boldsymbol{B}$. Here $\phi$ is a scalar potential and $\boldsymbol{B}$ is a vector potential. As a result,

$$\nabla \cdot \boldsymbol{u}^S = 0, \qquad \nabla \cdot \boldsymbol{u}^D = \nabla \cdot \boldsymbol{u},$$

$$\nabla \times \boldsymbol{u}^S = \boldsymbol{\omega}, \qquad \nabla \times \boldsymbol{u}^D = 0.$$

The dilatational velocity field is computed by solving for $\phi$ through the Poisson equation $\nabla^2 \phi = \nabla \cdot u$ and computing $\boldsymbol{u}^D = \nabla \phi$. The solution of the Poisson equation follows the same methodology as used for NGA (chapter 2). The solenoidal velocity field is then calculated as $\boldsymbol{u}^S = \boldsymbol{u} - \boldsymbol{u}^D$.

This decomposition is used to separate the strain-rate tensor into that resulting from the dilatational velocity field ($S^D$) and the solenoidal velocity field ($S^S$). Under the current low-Mach conditions, dilatation is due only to the heat release and $\boldsymbol{\omega} \cdot S^D \cdot \boldsymbol{\omega}$ can be associated with the effects of the flame in the enstrophy transport equation. The two terms employing the separate velocity fields are plotted for case $\mathrm{B}_{\mathrm{tab},1}^4$ in Fig. 6.3. As expected, $\boldsymbol{\omega} \cdot S^D \cdot \boldsymbol{\omega}$ is non-zero within the flame,
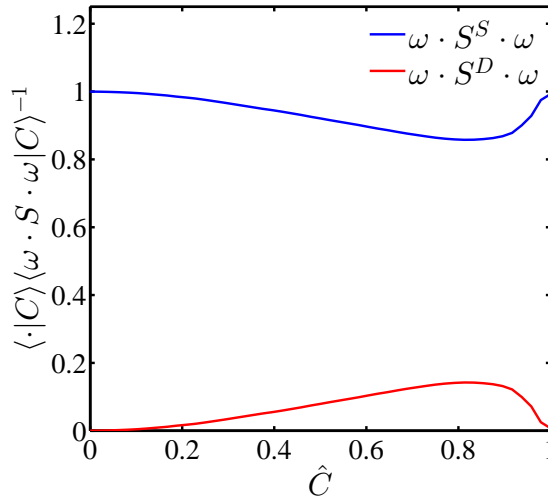
Figure 6.3: Dilatational and solenoidal parts of the vortex stretching term in the enstrophy transport equation ($\boldsymbol{\omega} \cdot S^D \cdot \boldsymbol{\omega}$ and $\boldsymbol{\omega} \cdot S^S \cdot \boldsymbol{\omega}$, respectively) for case $\mathrm{B}^4_{\mathrm{Tab},1}$. Each are normalized by the vortex stretching term using the full velocity field, $\boldsymbol{\omega} \cdot S \cdot \boldsymbol{\omega}$.

while going to zero in the reactants and products where $\boldsymbol{\omega} \cdot S^S \cdot \boldsymbol{\omega}$ is equal to the full term, $\boldsymbol{\omega} \cdot S \cdot \boldsymbol{\omega}$.

This decomposition is applied to the anisotropic vortex stretching term, so that $\boldsymbol{A}_1^D$ and $\boldsymbol{A}_1^S$ employ the strain-rate tensor calculated using only the dilatational and solenoidal velocity fields, respectively. $\boldsymbol{A}_1^D$ is associated with the effects of the flame and, as such, is subsequently referred to as $\boldsymbol{A}_1^F$. The $x$ components of these terms are plotted in Fig. 6.4a for case A. Like the anisotropy vector ($\boldsymbol{W}$), $\boldsymbol{A}_1^F$ is positive in the $x$-direction. Additionally, the qualitative behavior as a function of $\hat{C}$ is very similar to $\boldsymbol{W}$, with the magnitude increasing through the flame. In contrast, $A_{1,x}^S$ is negative, and has the opposite sign as $W_x$; behavior similar to case A is found in the remaining cases. This suggests that $A_{1,x}^S$ acts to relax the flow to isotropy. In the absence of the flame, the turbulence relaxes the small scales toward isotropy. $A_{1,x}^F$ is provided in Fig. 6.4b for cases A, B, $\mathrm{B}^4_{\mathrm{Tab},1}$, $\mathrm{C}^*$, and D; and it decreases in magnitude as both the Karlovitz number and $l/l_F$ increase (Fig. 6.4b). From these results, the effects of the flame on the vortex stretching term must be considered as the possible cause for anisotropy.

Lastly, baroclinic torque and viscous dissipation are considered. Baroclinic torque is non-zero only due to the presence of the flame and the induced density gradient. It was observed to contribute significantly to vorticity anisotropy at low values of $Ka_u$ [59]. The effects of the flame on viscous
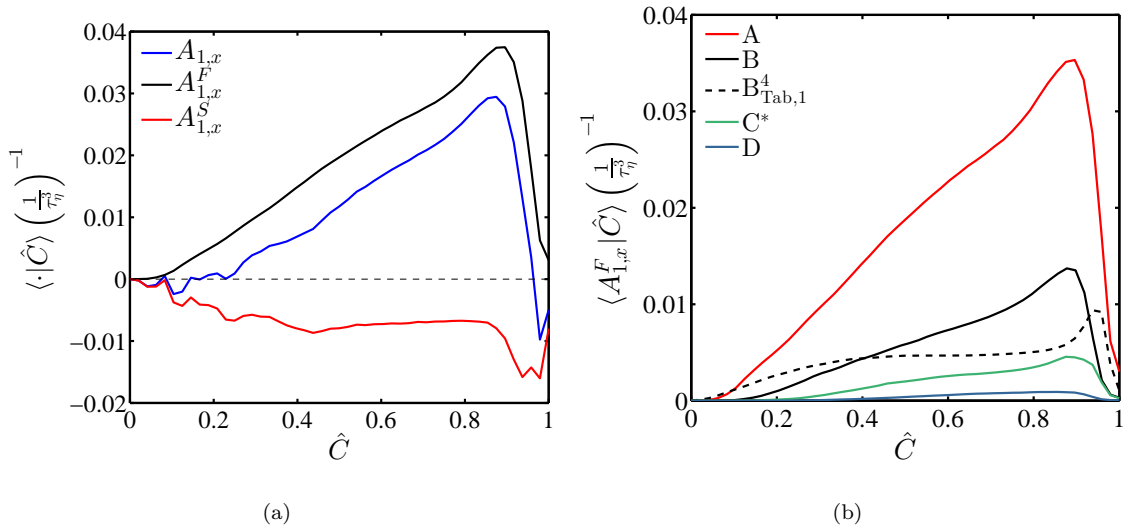
Figure 6.4: (a) Anisotropic vortex stretching term $(A_{1,x})$ along with the dilatational $(A_{1,x}^F)$ and solenoidal $(A_{1,x}^S)$ parts for case A. Dashed line at zero represents no anisotropy production. (b) $A_{1,x}^F$ for cases A, B, $B_{\text{tab},1}^4$, C*, and D.

dissipation are determined by, again, separating the flame contribution as $\boldsymbol{A}_4 = \boldsymbol{A}_4' + \boldsymbol{A}_4^F$, where

$$\boldsymbol{A}_{4,j}' = \nu \omega_j \nabla^2 \omega_j - \frac{1}{3} \sum_{i=1}^{3} \nu \omega_i \nabla^2 \omega_i, \tag{6.9}$$

(summation over repeated indices is not implied). The $\boldsymbol{A}_4^F$ term includes gradients of fluid properties and the velocity divergence.

## 6.1.4 Summary

The contribution of $A_{1,x}^F$, $A_{3,x}$, and $A_{4,x}^F$ to the growth of anisotropy is compared in Fig. 6.5 for cases A and $B_{\text{Tab},1}^4$. As shown, effect of the flame on the anisotropic vortex stretching term is greater than for both the baroclinic torque and viscous dissipation terms. In all the remaining cases, the magnitude of $A_{1,x}^F$ is larger than $A_{3,x}$ and $A_{4,x}^F$ to a similar or greater extent than in case A.

From these results, it is concluded that the effect of the flame on the vortex stretching term is the primary cause for the growth of anisotropy. As these effects are through the velocity divergence, which may be equated to $-(D\rho/Dt)/\rho$, the anisotropy is a result of the density change through the flame. The following section investigates the impact of the Karlovitz number and $l/l_F$ on the
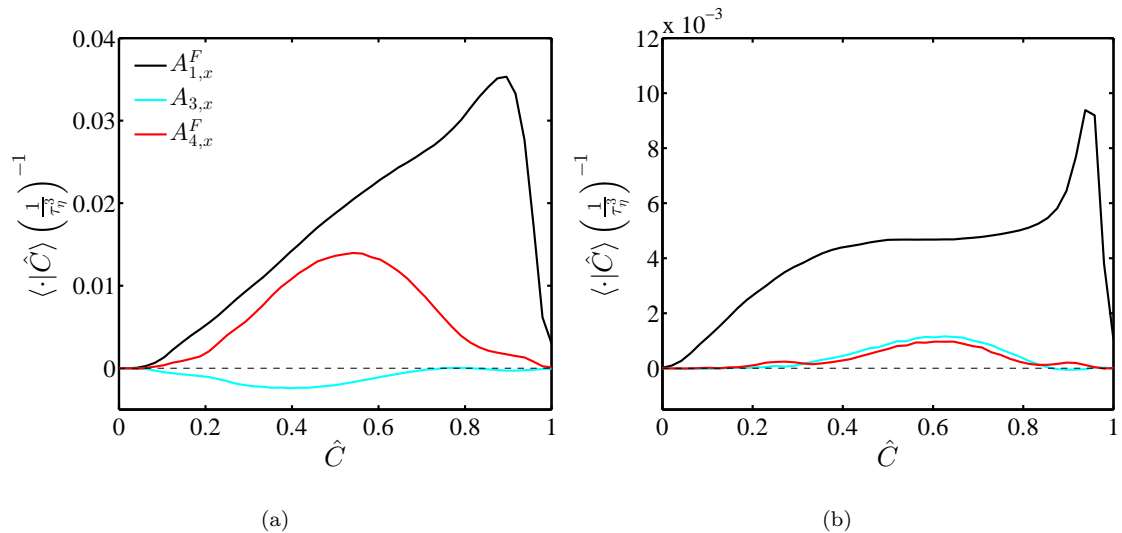
Figure 6.5: Terms $A_{1,x}^F$, $A_{3,x}$, and $A_{4,x}^F$ for case (a) A and (b) $B_{\text{Tab},1}^4$, showing the contribution to anisotropy by the effect of the flame on the anisotropic vortex stretching, baroclinic torque, and viscous dissipation terms.

vorticity anisotropy.

## 6.2 Local versus global effects

The purpose of this section is to address how the parameters $Ka$ and $l/l_F$ impact the behavior of the anisotropic vortex stretching term and vorticity vector. This is accomplished by distinguishing aspects of the local flame-turbulence dynamics from the flame geometry and its orientation.

### 6.2.1 Local vorticity behavior

In this section, the local behavior of the vorticity vector is investigated by considering its alignment within the strain-rate tensor, $S$, eigenframe [42, 43]. This is considered because of the importance of this vorticity alignment to the vortex stretching term and the local dynamics of homogeneous isotropic turbulence [113, 1, 47, 36].

**6.2.1.1 Review of homogeneous isotropic turbulence**

As $S$ is a real symmetric tensor, its eigenvectors are orthogonal and all the eigenvalues are real. The eigenvectors of the strain-rate tensor are denoted as $S_1$, $S_2$, $S_3$ with corresponding eigenvalues, $\lambda_1$, $\lambda_2$, $\lambda_3$. The eigenvalues are listed in decreasing order so that $S_1$ is the most extensive direction and $S_3$ is the most compressive direction. Considering DNS of homogeneous isotropic turbulence, Ashurst et al. [1] found that vorticity preferentially aligns with the second, or intermediate, eigenvector of the strain-rate tensor ($S_2$), with a slight preference to align with the $S_1$ over the $S_3$ eigenvector. This preferential alignment of vorticity within the eigenframe is often used for gaining insight into the local turbulence dynamics and for modeling purposes [117]. It was also found that $\lambda_2$ is, on average, positive, and $\lambda_1$ and $\lambda_3$ are nearly equal in magnitude but of opposite sign [113, 1]. Finally, vortex stretching (represented in the vortex stretching term) is the amplification of vorticity through its alignment with the $S$ eigenvectors which have positive eigenvalues. Therefore, vortex stretching can only occur if vorticity is aligned in either the $S_1$ or $S_2$ directions [113].

**6.2.1.2 High Karlovitz number case**

The alignment of vorticity with the eigenvectors is discussed first for case D, which is the least anisotropic case, as it has the highest Karlovitz number and lowest flame density ratio. This is investigated qualitatively by computing three-dimensional surface PDFs, referred to here as spherical PDFs. Color levels represent the PDF of the vector orientation, and are normalized by the value corresponding to uniform random vector orientation [117]. Spherical PDFs have been previously used as an effective means of communicating the alignment of vorticity in the strain-rate eigenframe [42, 43, 117]. Figure 6.6 presents the spherical PDFs of the vorticity alignment for case D near the reactants ($\hat{C} = 0.05$) and within the flame ($\hat{C} = 0.8$). These results show the preference for vorticity to align with the $S_2$ direction, as expected from homogeneous isotropic turbulence.

Results are compared quantitatively with a previous DNS of homogeneous isotropic turbulence by Carroll et al. [13] ($Re_t = 201$; $Re_\lambda = 55$), which has a comparable turbulent Reynolds number to case D ($Re_{t,u} = 380$, which reduces to $Re_{t,b} = 68$ in the products). Comparison is made through
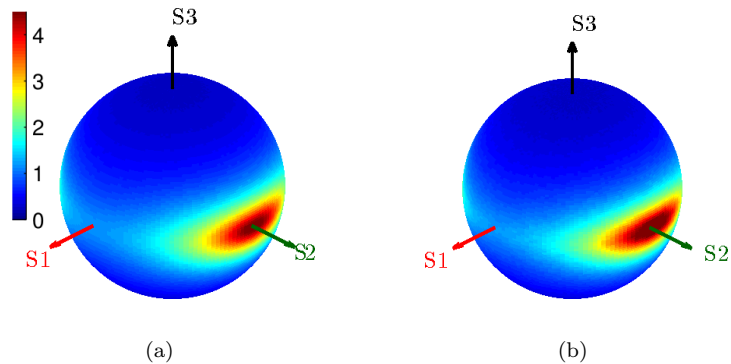
Figure 6.6: Spherical PDF for the alignment of vorticity with the $S$ eigenvectors for case D (a) in the reactants ($\hat{C} = 0.05$) and (b) within the flame ($\hat{C} = 0.8$).
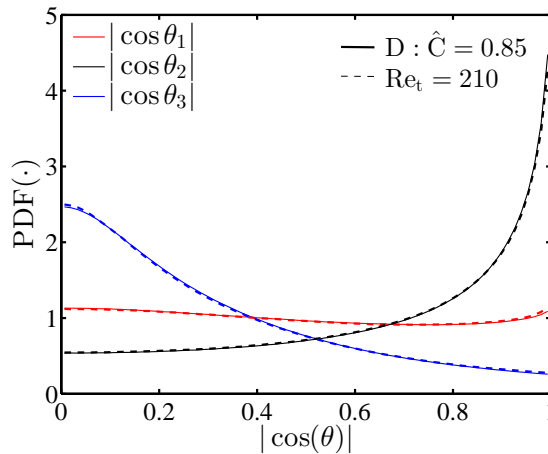


Figure 6.7: PDFs of $|\cos(\theta_i)|$ where $\theta_i$ is the angle between the vorticity vector and the eigenvector $S_i$. Solid lines correspond to case D at $\hat{C} = 0.85$. Dashed lines representing $Re_t = 201$ are calculated from the previous simulation of homogeneous, isotropic turbulence by Carroll *et al.* [13].

the PDFs of $|\cos(\theta_i)|$, where $\theta_i$ is the angle between the vorticity vector and the eigenvector $S_i$, as similarly calculated in previous studies [1, 14] (Fig. 6.7). The alignment of the vorticity vector within the flame is in excellent agreement with results from homogeneous isotropic turbulence. Good agreement was also found in the eigenvalue of $S$, as discussed in Appendix D. Combined with the vorticity isotropy found in section 6.1, these results support that given a sufficiently high Karlovitz number, the vorticity isotropy and its alignment within the $S$ eigenframe are unaltered by the flame and resemble that of homogeneous isotropic turbulence.
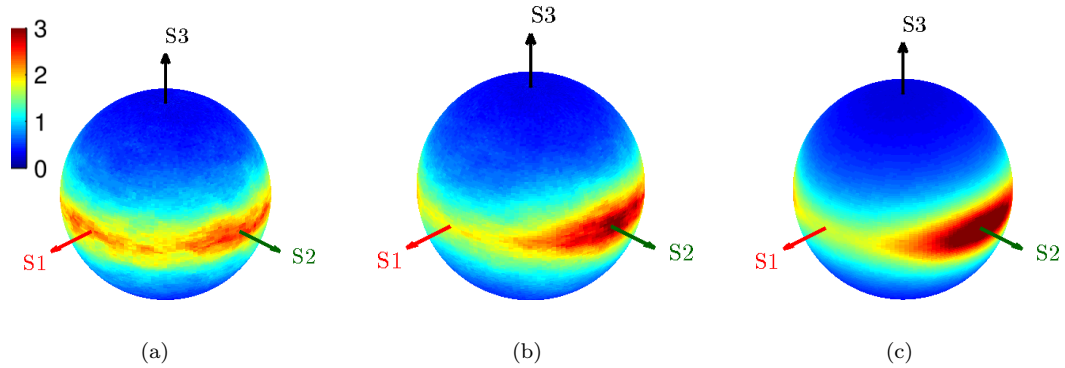
Figure 6.8: Spherical PDFs of the vorticity alignment with the strain-rate tensor eigenvectors for case (a) A, (b) B, and (c) $\mathrm{B}^4_{\mathrm{Tab},1}$ at $\hat{C} = 0.8$.

### 6.2.1.3   Moderate Karlovitz number cases

In the remaining cases, spherical PDFs (Fig. 6.8) show that the alignment of vorticity within the $S$ eigenframe is altered by the flame. Qualitatively, there is greater alignment with the $S_1$ eigenvector, and this change is more prominent at lower values of $Ka$. Notably, the spherical PDFs of cases B and $\mathrm{B}^4_{\mathrm{Tab},1}$ show a similar increase in the alignment with $S_1$.

Quantitatively, the PDFs of $|\cos(\theta_i)|$ in Fig. 6.9 similarly show the alignment with the $S_1$ direction increases, while the alignment with the $S_2$ direction decreases in the flame. This result agrees with previous findings in turbulent reacting flows [45, 14, 38]. To further compare the increased alignment with $S_1$ between the different cases, the mean value of $|\cos(\theta_1)|$ at $\hat{C} = 0.85$ is plotted versus the corresponding value of $Ka/\gamma$ (Fig. 6.10). The quantity $Ka/\gamma$ was shown in chapter 5 to capture the competing effects of the turbulence and the velocity divergence on the strain-rate tensor (Eq. 5.6) and appears to present a good scaling for the vorticity alignment in the present cases. Once again, cases B and $\mathrm{B}^4_{\mathrm{Tab},1}$ are very similar, suggesting the independence of the local vorticity behavior from $l/l_F$.

As the alignment with the $S_1$ direction increases at lower Karlovitz numbers, the effects of the flame are to promote an increase in vortex stretching in this direction ($S_1$ has a positive eigenvalue). This additional production of vorticity by vortex stretching in a manner unlike homogeneous isotropic turbulence is consistent with a growth of anisotropy.
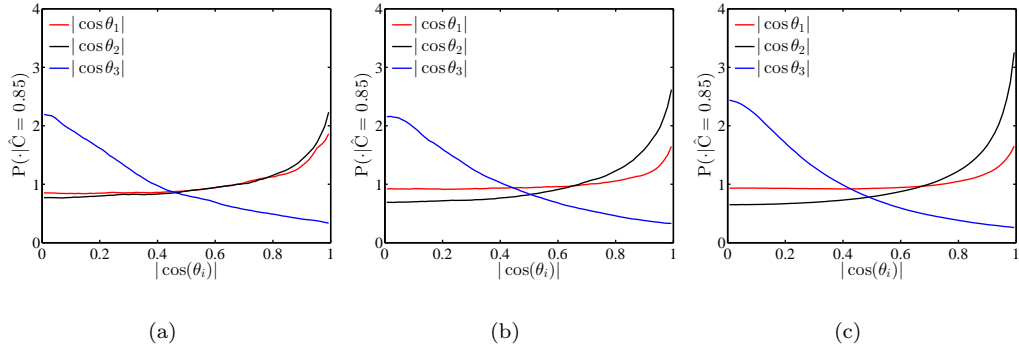
Figure 6.9: PDFs of $|\cos(\theta_i)|$ where $\theta_i$ is the angle between the vorticity vector and the eigenvector $S_i$: cases (a) A, (b) B, and (c) $B^4_{\text{tab},1}$ at $\hat{C} = 0.85$.
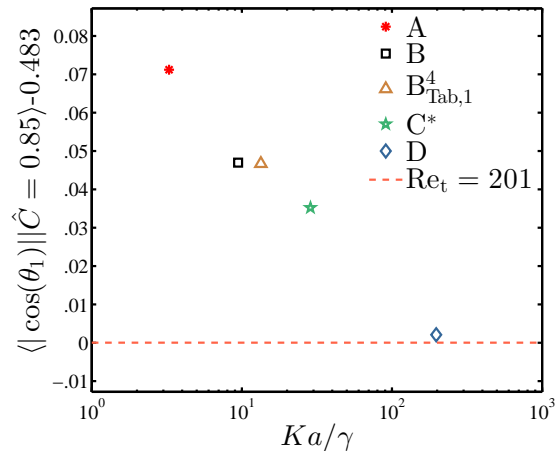


Figure 6.10: Mean value of $|\cos(\theta_1)|$ at $\hat{C} = 0.85$, showing the increased alignment with the $S_1$ eigenvector as a function of $Ka/\gamma$ (also evaluated at $\hat{C} = 0.85$). Values are relative to that of homogeneous, isotropic turbulence at $\text{Re}_t = 201$, calculated from the DNS previously preformed by Carroll *et al.* [13] and represented by the dashed line at zero.
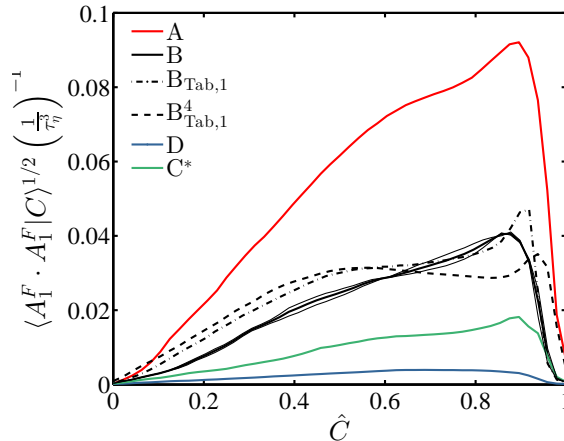
Figure 6.11: Conditional average of $\boldsymbol{A}_1^F \cdot \boldsymbol{A}_1^F$ for cases A, B, $B_{\text{Tab},1}$, $B_{\text{Tab},1}^4$, and D. Thin black lines correspond to averages for case B when either the first or second half of the data is used; they are indicative of the statistical uncertainty in the computed averages.

The following section further investigates the local turbulence behavior by considering the vortex stretching term, due to its importance in generating anisotropy.

## 6.2.2 Local vortex stretching term

The local dynamics of the vortex stretching term are investigated by considering the scalar quantity $\boldsymbol{A}_1^F \cdot \boldsymbol{A}_1^F$, as it is independent of the vector orientation. The purpose of considering this quantity is to remove any dependence on the geometry and coordinate system. A value of zero signifies the flame does not contribute to anistoropy through the production term. Figure 6.11 shows, as expected, that this quantity is reduced as the Karlovitz number increases and the density ratio decreases. In case D, the effect of the flame on the anisotropic vortex stretching term is smallest.

Notably, there is good agreement between cases B and $B_{\text{Tab},1}^4$. This agreement points to the similar behavior of the anisotropic vortex stretching term in a local sense based on the Karlovitz number and flame density ratio, independent of the flame geometry and large turbulent length scales $(l/l_F)$. Combined with the previous section (sec. 6.2.1), these results suggest that the fundamental flame-turbulence interaction is largely unaltered between cases B and $B_{\text{Tab},1}^4$. The cause for the differences of $\langle A_{1,x}^F|C\rangle$ and $\langle W_x|C\rangle$ between cases B and $B_{\text{Tab},1}^4$ (Fig. 6.1b and Fig. 6.4b) is investigated next by considering the impact of the large scales through the flame geometry.
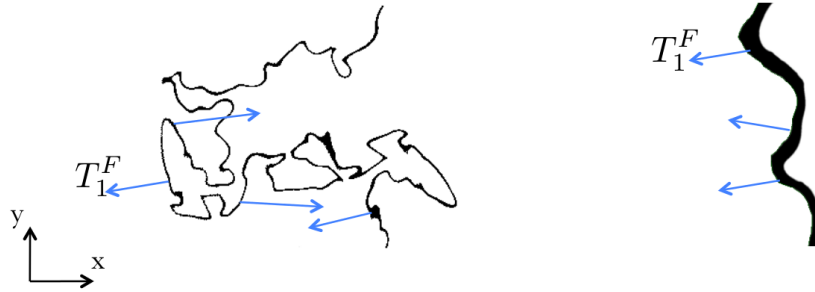
Figure 6.12: Illustration of the influence of flame geometry on the resulting anisotropy production. The solid black line represents the flame surface while arrows represents the effect of the flame on vorticity.

### 6.2.3 Flame orientation

The net contribution to anisotropy by $\boldsymbol{A}_1^F$ may be zero ($\langle A_{1,i}^F | C \rangle = 0$), even if $\boldsymbol{A}_1^F$ is locally and instantaneously non-zero. This occurs if the flame alters the vortex stretching term, but does so equally in all directions. This geometric effect is particularly relevant due to this term's dependence on the dilatational velocity field, $\boldsymbol{u}^D$, which depends on the flame geometry through the density field. This is illustrated in Fig 6.12 by considering two hypothetical cases with different flame geometries. In this figure, the solid black line represents the surface of the flame and the arrows represent the effect of the flame on vorticity. As shown, even if the local behavior is similar along the flame surface, differences in a fixed coordinate system cause the net contribution to anisotropy to not be equal.

As a measure of the flame surface orientation, Fig. 6.13 presents the PDFs of $(\partial \rho / \partial x)/|\nabla \rho|$ within the flame ($\hat{C} = 0.85$). For all cases, the density gradient is on average in the $x$ direction, corresponding to a value of $(\partial \rho / \partial x)/|\nabla \rho| = 1$. Departure of the PDFs from this alignment is due to wrinkling of the flame. In the limit that the density gradient is completely isotropic, the PDFs uniformily equal 0.5.

Considering cases A, B, C*, and D, the orientation of the density gradient becomes more isotropic as the Karlovitz number increases and density gradient decreases. In addition, there is a significant increase in the isotropy of the density gradient with a larger value of $l/l_F$, (case B versus $B_{Tab,1}^4$). The greater isotropy of the flame normal (defined as the unit normal aligned with the density gradient) in $B_{Tab,1}^4$ is visually evident when considering Fig. 4.2 and is due to the larger length scales over
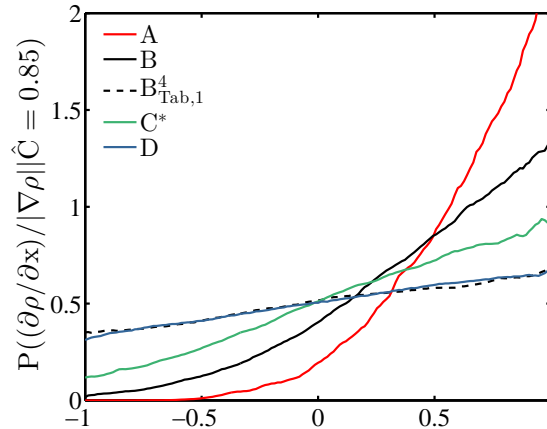
Figure 6.13: PDFs of $(\partial\rho/\partial x)/|\nabla\rho|$ for cases A, B, $B^4_{Tab,1}$, $C^*$, and D at $\hat{C} = 0.85$. Values of 1 and -1 represent alignment of the density gradient and the respective coordinate direction, while 0 represents orthogonality.

which the flame may wrinkle.

## 6.2.4    Discussion

In section 6.1, it was found that larger values of both the Karlovitz number and large turbulent scales $(l/l_F)$ promote vorticity isotropy. However, they alter the isotropy of the smallest turbulent scale in different ways.

At sufficiently high Karlovitz numbers, the local dynamics of the vortex stretching term and vorticity vector were found to resemble homogeneous isotropic turbulence (exemplified by case D in sections 6.2.1 and 6.2.2). Small scale isotropy results because of a fundamental similarity in the behavior of the smallest turbulent scales throughout the flame and in homogeneous isotropic turbulence. The $Ka$ and density ratio dependence helps explain the increasing isotropy between cases A, B, $C^*$, and D.

This description is illustrated in Fig. 6.14, which highlights the competing effects of the turbulence and flame on the alignment of vorticity in the strain-rate eigenframe. In the flame, the alignment with the $S_1$ direction increases at lower Karlovitz numbers, promoting an increase in vortex stretching in $S_1$ (possibly scaling with $Ka/\gamma$). Concurrently, the turbulence attempts to relax the flow towards homogeneous isotropic turbulence with vorticity preferentially aligning with $S_2$. As written in the figure, vortex stretching (when considered alone) amplifies vorticity, resulting in
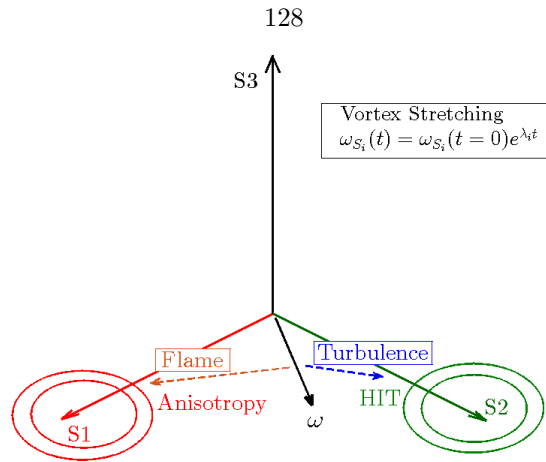
Figure 6.14: Illustration of the competition between the flame and the turbulence on the local alignment of vorticity in the strain-rate eigenframe, relaxing the turbulence toward homogeneous isotropic turbulence (HIT) or causing the growth of anisotropy. The quantity $\omega_{S_i}$ is vorticity aligned with the $S_i$ eigenvector, and, considering the effects of vortex stretching alone, exponentially grows or decays according to its associated eigenvalue, $\lambda_i$.

its exponential growth. Qualitatively, the effects of this mechanism are consistent with the observed behavior of $W_x$, as $\lambda_1$ is the largest positive eigenvalue and vorticity anisotropy demonstrates a compounding growth through the flame (Fig. 6.1). This is most clearly seen in cases A and B which have the greatest levels of anisotropy.

The local dynamics of vorticity and the vortex stretching term, however, do not explain the greater vorticity isotropy observed in case $B^4_{Tab,1}$ compared to case B (Fig. 6.1b), as the large scales $(l/l_F)$ were found to have minimal impact on their behavior (Fig. 6.10 and 6.11). However, greater isotropy of the flame normal in case $B^4_{Tab,1}$ compared with case B (Fig. 6.13) suggests the decreased vorticity anisotropy is simply due to the flame altering the vortex stretching term more equally in all directions, thus reducing the net contribution to anisotropy (the different flame geometries are also visually evident in Fig. 4.2). This a geometric effect only and is expected to be configuration dependent. The resulting small scale isotropy does not reflect a fundamental similarity between the small scale turbulence dynamics in the flame and in homogeneous isotropic turbulence.

In summary, local and global effects are found to depend separately on the Karlovitz number and large turbulent scales. The combination of these effects produces the observed dependence of anisotropy on these parameters.

## 6.3 Correspondence to vortex simulations

This chapter found that anisotropy is primarily produced through the vortex stretching term. This term involves inherently 3D dynamics, which are not present when considering a 2D vortex. While the 2D vortex-flame interaction is useful, it does not have a correspondence to the mechanism responsible for the production of anisotropy found at high Karlovitz numbers.

Previous studies at low Karlovitz numbers [59], found anisotropy in vorticity and related this anisotropy primarily to the effects of baroclinic torque. At low Karlovitz numbers, the smallest turbulent scales are larger and slower than the flame ($\eta \gg l_F$, $u_\eta \ll S_L$), which corresponds a large-slow vortex. As this type of vortex is also dominated by baroclinic torque, further comparison of these two cases may yield useful insights into the mechanism producing anisotropy at low Karlovitz numbers.

## 6.4 Summary and conclusion

The isotropy of the smallest turbulent scales in high Karlovitz number premixed flames was studied in this chapter by considering the vorticity vector and its transport equation. For this purpose, the DNS of high Karlovitz number premixed flames described in chapter 4 were analyzed. The conclusions are summarized in the following and several points of application are discussed.

Larger values of both the Karlovitz number and $l/l_F$ were found to promote vorticity isotropy. Given a sufficiently high value of the Karlovitz number, the vorticity is isotropic throughout the flame and the behavior of vorticity within the strain-rate tensor eigenframe resembles that of homogeneous isotropic turbulence. This supports the validity of Kolmogorov's hypothesis of local isotropy in this case.

Vorticity anisotropy, at moderate values of $Ka$, suggests that Kolmogorov's hypothesis of local isotropy is not valid at lower Karlovitz numbers. The primary cause for the growth of anisotropy was determined to be the vortex stretching term. The local dynamics of the vortex stretching term and vorticity were found to depend on the Karlovitz number and flame density ratio. In this case, the

vorticity was found to have greater alignment with the most extensive eigenvector of the strain-rate tensor compared with homogeneous isotropic turbulence. This suggests that the flame promotes an increase in vortex stretching.

A larger value of $l/l_F$ was found to have minimal impact on the local dynamics of vorticity and the vortex stretching term. The results suggest that greater vorticity isotropy is simply due to the flame altering the vortex stretching term more equally in all directions, reducing the net contribution to anisotropy. The resulting isotropy does not reflect a fundamental similarity between smallest turbulent scales in the flame with homogeneous isotropic turbulence. This is a geometric effect only and is expected to be configuration dependent. This conclusion is particularly relevant to practical applications which possess larger integral length scales.

Lastly, it was found that using tabulated chemistry with unity Lewis number transport resulted in the same vorticity anisotropy as with a finite-rate chemical model and constant non-unity Lewis numbers, as similarly found previously for the transport of enstrophy in chapter 5. This further supports the use of these simplified chemical and transport models in simulations studying the effects of the flame on turbulence. The ability to employ alternative chemical models allows the future study of more complex geometries and larger turbulent Reynolds numbers. Extension of these conclusions to other conditions, such as lean hydrogen/air flames, where thermo-diffusive instabilities occur, is unclear and should be the subject of future work.

The present results may be related to those of Hamlington *et al.* [38]. The primary source of anisotropy identified in the current study is similar to the explanation offered in their work, that being vortex stretching. However, Hamlington *et al.* [38] observed the onset of isotropy at significantly lower Karlovitz numbers than in the current study. The reasons are as follows. Temperature dependent viscosity increases through the flame which reduces the local Karlovitz number. Lower local Karlovitz numbers were shown here to support an increase in flame induced vortex stretching (possibly scaling with $Ka/\gamma$). Without the effects of temperature dependent viscosity (absent in an ILES framework with zero molecular viscosity), the local Karlovitz number will be relatively larger and vortex stretching by the flame will be weaker, which will promote isotropy at lower values of

$Ka_u$. This emphasizes the importance of the physical viscosity to correctly capture the behavior of the smallest turbulent scales in premixed turbulent combustion.

# Chapter 7

# Comprehensive summary and conclusions

The objective of this thesis was to characterize the behavior of the smallest turbulent scales within high Karlovitz number premixed flames through the study of vorticity. Three specific objectives were addressed. The first objective was to understand how the flame alters an individual 2D vortex through the different terms in the vorticity transport equation based on the initial size and strength of the vortex. After studying this simplified test case, the second objective was to characterize the behavior of enstrophy and its transport through high Karlovitz number premixed flames. The final objective was to then assess the isotropy of vorticity.

The primary conclusion from this thesis is that the effect of the flame on both the magnitude and orientation of vorticity diminishes as the Karlovitz number increases. The results support the validity of Kolmogorov's first similarity hypothesis and the hypothesis of local isotropy given a sufficiently high Karlovitz number ($Ka \gtrsim 100$). As the limit of a low Karlovitz number represents the absence of any effects of the turbulence on the flame, this provides a cohesive picture that the limit of high Karlovitz number represents the absence of any effects of the flame on the small scale turbulence. Therefore, the Kolmogorov time, length, and velocity scales ($\tau_\eta$, $\eta$, and $u_\eta$, respectively) correctly characterize the smallest turbulent scales within the flame, just as in homogeneous isotropic turbulence. Thus, it is physically meaningful to consider the local Karlovitz number within the flame. However, the Kolmogorov scales are likely not meaningful at lower Karlovitz numbers, where the smallest turbulent scales do not depend on $\epsilon$ and $\nu$ alone.

The following provides a discussion of the individual conclusions of each chapter, implications on implicit large eddy simulations (ILES) and, lastly, possible directions for future LES modeling efforts given these results. These results may be used within future work to develop improved LES models of high Karlovitz number premixed turbulent combustion. With more accurate models, the design of aircraft combustors and other combustion based devices may better mitigate the detrimental effects of combustion, from reducing $CO_2$ and soot production to increasing engine efficiency.

## 7.1 2D vortex-flame interaction

In chapter 3, the 2D vortex-flame interaction was studied. Simulations were performed over a wide range of sizes and strengths of the initial vortex. These results were combined with a theoretical analysis to determine different limiting behaviors of the vortex. In each limiting case, the most relevant transport term and the resulting impact on vorticity by the flame was characterized.

Specifically, it was found that large ($l_v/l_F \gg 1$) and slow ($u_v/S_L \ll 1$) vortices generate large scale curvature of the flame front which results in the significant production of vorticity by baroclinic torque. Small ($l_v/l_F \ll 1$) and fast ($u_v/S_L \gg 1$) vortices do not produce large scale curvature, and the vortex is altered by the effects of dilatation when viscous effects do not dominate. This causes the vortex vorticity to decrease and expand radially. A fast and large vortex generates significant distortions to the flame front geometry; the vortex is transformed by the effects of both dilatation and baroclinic torque. A small and slow vortex is dampened and lengthened normal to the flame due to dilatation. In the limit of an infinitely small vortex, viscous effects dominate and destroy the vortex before it even interacts with the flame.

This study of the vortex-flame interaction yielded a qualitative understanding of how and when the flame affects vorticity through the terms in the vorticity transport equation. Specifically, dilatation reduces vorticity through volumetric expansion. This term is important for small vortices when viscous effects do not dominate. Baroclinic torque may significantly alter the initial vortex and was found to be important only for large vortices. Lastly, viscous effects become more important as vortices become smaller. This qualitative description provides a foundation for investigating

vorticity in turbulent combustion. The limit of a small vortex was found to relate to high Karlovitz number behavior ($\eta \ll l_F$ and $l_v \ll l_F$) as viscous effects scale similarly and dominate over dilatation and baroclinic torque in both cases. Additionally, baroclinic torque has been found to be important for both lower Karlovitz numbers [59] and larger vortices (section 3.3), but investigating this correspondence requires further study.

## 7.2 DNS of high Karlovitz number premixed flames

In chapter 4, the physical and numerical configurations of the high Karlovitz number, $n$-heptane/air, premixed flame DNS performed in this thesis were presented. The turbulence intensity, $l_o/l_F$, and temperature in the reactants were varied between simulations to investigate the effects of the unburnt Karlovitz number, largest turbulent length scales, and flame density ratio. The unburnt Karlovitz number and turbulent Reynolds number each varied by an order of magnitude ($Ka_u$=70 - 750, $Re_{t,u}$=83 - 1150). A preliminary analysis found that the turbulent kinetic energy, integral length scale, and viscous dissipation rate were in good agreement with the expected values imposed by the forcing.

## 7.3 Enstrophy transport at high Karlovitz numbers

The behavior of the mean enstrophy and terms in its transport equation were characterized in chapter 5. A theoretical scaling analysis was performed to estimate the magnitude of each term through the flame and across run conditions. Supported by the DNS results, this analysis was used to propose a normalized enstrophy transport equation for high Karlovitz numbers. Three primary conclusions are as follows.

First, the proposed normalized enstrophy transport equation involves a small set of parameters. From this equation, the relative magnitude of vortex stretching, dilatation, baroclinic torque, and viscous dissipation within the flame may be predicted as a function of the Karlovitz number and flame conditions.

Second, the normalized enstrophy equation predicts that vortex stretching and viscous dissipation dominate the behavior of enstrophy in the limit of high $Ka$. In homogeneous, isotropic turbulence, enstrophy transport also obtains a balance of these two terms. As a consequence, enstrophy scales in the same manner within the flame as in homogeneous, isotropic turbulence given a sufficiently high $Ka$. Specifically, the mean enstrophy scales with the inverse of the Kolmogorov time scale squared, $1/\tau_\eta^2$. Therefore, for sufficiently high $Ka_u$, the mean enstrophy obtains the same value as in homogeneous, isotropic turbulence given the local $\epsilon$ and $\nu$. These conclusions were found to be independent of the Reynolds number and the physical configuration (*i.e.* forced or unforced).

Third, as $\tau_\eta$ is only a function of $\epsilon$ and $\nu$, this conclusion supports the validity of Kolmogorov's first similarity hypothesis in high $Ka$ premixed flames. It also suggests that in low Karlovitz number flames, the smallest turbulent scales behave differently through the flame and this hypothesis may not be valid.

## 7.4 Vorticity isotropy at high Karlovitz numbers

The isotropy of the smallest turbulent scales in high Karlovitz number premixed flames was studied in chapter 6 by considering the vorticity vector and its transport equation. This analysis was also performed using the simulations discussed in chapter 4. The conclusions are summarized in the following.

Larger values of both the Karlovitz number and $l/l_F$ were found to promote vorticity isotropy. Given a sufficiently high value of the Karlovitz number, the vorticity is isotropic throughout the flame and the behavior of vorticity within the strain-rate tensor eigenframe resembles that of homogeneous isotropic turbulence.

Combined with chapter 5, these results support that for a sufficiently high Karlovitz number the only effect of the flame, which is relevant to the smallest turbulence scales, is the increase in local viscosity. The increase in viscosity reduces enstrophy through the relationship, $\omega^2 = 1/\tau_\eta^2$. Both the magnitude and orientation of vorticity are otherwise unaffected by the flame. Together, these studies support the validity of Kolmogorov's first similarity hypothesis and the hypothesis of local

isotropy given a sufficiently high Karlovitz number.

At moderate values of $Ka$, significant anisotropy was found in vorticity, suggesting that Kolmogorov's hypothesis of local isotropy is not valid in this case. Considering the vorticity equation, the vortex stretching term was determined to be the primary cause for the growth of anisotropy. The local dynamics of the vortex stretching term and vorticity were found to depend on the Karlovitz number and flame density ratio. In this case, the vorticity was found to have greater alignment with the most extensive eigenvector of the strain-rate tensor compared with homogeneous isotropic turbulence. This suggests that the flame promotes an increase in vortex stretching.

A larger value of $l/l_F$ was found to have minimal impact on the local dynamics of vorticity and the vortex stretching term. The results suggest that greater vorticity isotropy is simply due to the flame altering the vortex stretching term more equally in all directions, reducing the net contribution to anisotropy. The resulting isotropy does not reflect a fundamental similarity between smallest turbulent scales in the flame with homogeneous isotropic turbulence. This is a geometric effect only and is expected to be configuration dependent.

## 7.5   Impact of chemistry and transport models

In chapters 5 and 6, simplified chemical and transport models employed in additional DNS were observed to introduce negligible effects on the results. Tabulated chemistry modeled with unity Lewis number transport provided sufficient detail of the flame structure to capture the same characteristics of mean enstrophy and vorticity isotropy as detailed chemistry with constant non-unity Lewis numbers. This suggests that future numerical simulations used to study the effects of the flame on small scale turbulence does not need to include details of finite-rate chemistry and differential diffusion to accurately capture the relevant physics. The ability to employ alternative chemical models allows the study of more complex geometries and larger turbulent Reynolds numbers.

## 7.6 ILES

The results of this thesis have implications on numerical methods, such as implicit large eddy simulations (ILES) [35], which rely on numerical viscosity for all or part of the energy dissipation in simulations of premixed turbulent combustion. This discussion builds upon this thesis and the recent work of Lapointe *et al.* [55], both of which shed light on the importance of temperature dependent viscosity in premixed turbulent combustion.

Recall that one conclusion of the present work is that, at high $Ka$, the smallest turbulent scales throughout the flame are controlled entirely by the local dissipation rate and the local molecular viscosity; this is Kolmogorov's first similarity hypothesis. Given the importance of viscosity, two simulations performed with different viscosity models would produce correspondingly different transformation of the enstrophy field. For instance, in the work of Hamlington *et al.* [38] which used an ILES framework (with zero molecular viscosity), it was observed that the flame had little effect on the mean vorticity at high turbulence intensities. This behavior is in contrast to the present work, which demonstrated large changes through the flame, and the behavior is likely due to the absence of temperature dependent molecular viscosity which varies through the flame.

A further implication of these results relates to the response of the flame chemical reaction zone to the incoming turbulent flow. Lapointe *et al.* [55] found that the reaction zone behavior in high $Ka_u$ premixed flames is controlled by the local reaction zone Karlovitz number, $Ka_\delta = (\delta/\eta)^2$, where $\delta$ is the reaction zone thickness, rather than the unburnt Karlovitz number. As $\eta$ increases significantly through the flame via its dependence on $\epsilon$ and $\nu$, any discrepancies in these quantities due to modeling simplification (such as used in ILES) would result in a different value of $Ka_\delta$. In other words, the treatment of molecular viscosity through the flame directly impacts the behavior of the chemical reaction zone. Therefore, the transition between the thin reaction zone, broken reaction zone, and distributed reaction zone may vary between simulations employing numerical viscosity and physical molecular viscosity. This discussion highlights certain limitations of ILES given recent results which demonstrate the importance of temperature dependent viscosity in premixed turbulent combustion.

## 7.7   Future application to LES

While the development of subgrid scale (SGS) models is beyond the scope of this thesis, the above results provide/suggest directions for modeling high Karlovitz number premixed flames using LES. It was found that within high $Ka$ premixed flames, the vorticity is isotropic and its magnitude scales in the same manner as in constant density, homogeneous, isotropic turbulence. Once again, vorticity is characteristic of the smallest turbulent scales and these scales are smaller than the flame thickness at high $Ka$. Therefore, this suggests the scales smaller than the flame thickness may be modeled in the same manner as in homogeneous isotropic turbulence within the framework of large eddy simulations. This corresponds to an LES filter width smaller than the flame thickness: $l_F > \Delta > \eta$. For example, versions of the linear-eddy turbulent mixing model, used in premixed turbulent combustion, employ the Kolmogorov scales as parameters within the model [48]. At sufficiently high Karlovitz number this work suggests these parameters can remain the same as in homogeneous isotropic turbulence. While, it is unclear if this result holds for filter widths larger than the flame thickness, in section 5.3.1 it is shown that the majority of enstrophy is contained in scales smaller than the flame thickness. This suggests the possibility that models based on vorticity [70, 119] need not be altered for use in high $Ka$ premixed flames. In contrast, as the local turbulence dynamics at lower values of $Ka_u$ are not the same as in homogeneous isotropic turbulence, LES models based solely on homogeneous isotropic turbulence are not expected to fully capture the behavior of the smallest turbulent scales within the flame. Future testing and validation is required to confirm these hypotheses.

# Appendix A

# Vortex-flame simulations

## A.1 Numerical grid resolution

In this appendix, the resolution requirements and their evaluation are discussed for numerical simulations of the vortex-flame interaction. The resolution requirements are expressed as five parameters: the number of points across the flame, $n_F$, the number of points across the vortex length scale, $n_v$, length of domain in y direction, $L_y$, length of domain behind the flame, $L_x$, and the time step, $\Delta t$. The determined constraints are listed in table 3.1.

### A.1.1 Number of Points Across the Flame

The number of points required across the flame, $n_F$, is meant to capture the computational grid size required to resolve spatial gradients within the flame. The minimum acceptable value of $n_F$ is determined in four ways: convergence of the laminar flame speed, the number of points across the OH chemical source term, the species profiles in the flame, and a convergence study of run C.

First, a convergence study is performed for the flame speed of a one-dimensional flame varying the grid resolution. The flame speed is determined by linear regression of the flame position over time after reaching a steadily propagating flame. These show that the flame speed continues to increase until nearly 100 points per flame thickness, though changes may be under 1%. Second, Hawkes *et al.* [40] suggest that the OH source term should be spanned by at least 20 points. Here, this is satisfied when $n_F > 30$. Third, the chemical species profiles across the flame are compared based

upon the number of points across the flame. All the species profiles are very similar for $n_F > 18$ except for slight differences in the peak value of $H_2O_2$. These three results raise the question of how large of a deviation from the converged flame speed and species profiles is acceptable for the purposes of this study. To resolve this question, the convergence study of run C is performed, as described below in A.1.5. To summarize these results, the minimum value of $n_F$ is determined to be 55.

## A.1.2 Time Step

To determine the largest allowable time step, one-dimensional flame simulations are performed with various time steps, CFL conditions, and inflow velocities. Convergence occurs for $\Delta t = 2 \times 10^{-8}$ as no changes are observed in the flame below this value. With a larger time step, discontinuities or negative values develop in the chemical species profiles. The largest allowable time step is found to be related to the maximum production rate of the chemical reaction normalized by the local density and species mass fraction involved (*i.e.* smallest chemical time scales). The largest normalized reaction rate is approximately equal to $1/(2 \times 10^{-8}\text{s})$ and removing the associated reaction relaxes the required time step.

In the convergence study of run C, runs are performed with $\Delta t = 2 \times 10^{-8}$ and $\Delta t = 5.7 \times 10^{-9}$. Negligible differences are observed, supporting that $\Delta t = 2 \times 10^{-8}$ is sufficient in the one-dimensional flame as well as the full two-dimensional simulations.

## A.1.3 Number of Points Across the Vortex

To determine the number of points required to resolve the vortex, $n_v$, two-dimensional simulations of isolated decaying vortices are performed with varying grid resolutions. Simulated vortices are analyzed for asymmetries after the same duration of the corresponding vortex-flame interaction. Convergence requirements vary only slightly based on the size of the vortex and are most stringent for stronger vortices. For the vortex of run C, the vortex develops a non-symmetric profile about its axis with about 4% variation in the peak velocity when $n_v = 15$. This decreases to 0.5% when

$n_v = 22$. While this suggests convergence, run C requires a grid with $n_v$ equal to 180, which is nearly an order of magnitude larger. The large difference highlights the effects of the coupling of the fluid mechanics and chemistry. Therefore, the criteria of $n_v \geq 180$ is enforced for each simulation.

## A.1.4 Domain size

The requirement on the length of the domain in the y-direction, $L_y$, is primarily due to the expansion of products behind the flame while the length of the domain behind the flame, $L_x$, has the additional requirement of containing the flame thickness and final vortex.

During the flame-vortex interaction, the planar symmetry is broken and the rate of reactants consumed increases, causing the products to expand in all directions. Because of the periodic boundary conditions in the y-direction, the domain must be sufficiently large to capture this expansion unconstrained. Once again, a convergence study is performed, varying the length of the domain in the x and y-directions of run C providing six cases. Convergence is found for $L_x = 9l_v$, $L_y = 16.5l_v$, where the size and strength of the final vortex differs by about 1% from a significantly larger domain. Here, the fine grid occupies the central third of the domain which is also used subsequently.

The domain behind the flame, $L_x$, has the additional requirement of containing the flame thickness. In one-dimensional flame tests, the flame speed varies by less than 0.04% when $L_x$ was greater than $3l_F$. This criteria is relevant for the simulations of small vortices. Lastly, to practically contain the vortex within the region of fine grid spacing, the requirement is used that $2.5l_v$ be present in the region of fine grid spacing behind the flame. This is determined through run C and is found sufficient for the other cases.

## A.1.5 Convergence of run C

Several of the resolution requirements discussed above only consider the chemistry or the fluid dynamics in isolation. It is necessary to test convergence of the full vortex-flame interaction where these aspects are coupled. Towards that end, a convergence study is performed on the case $l_v/l_f = 3.25$ and $u_v/S_L = 52$, labeled run C. This is chosen because it is a fast and large vortex, which is

(a) $nx_{fine} = 720$     (b) $nx_{fine} = 1080$     (c) $nx_{fine} = 1680$
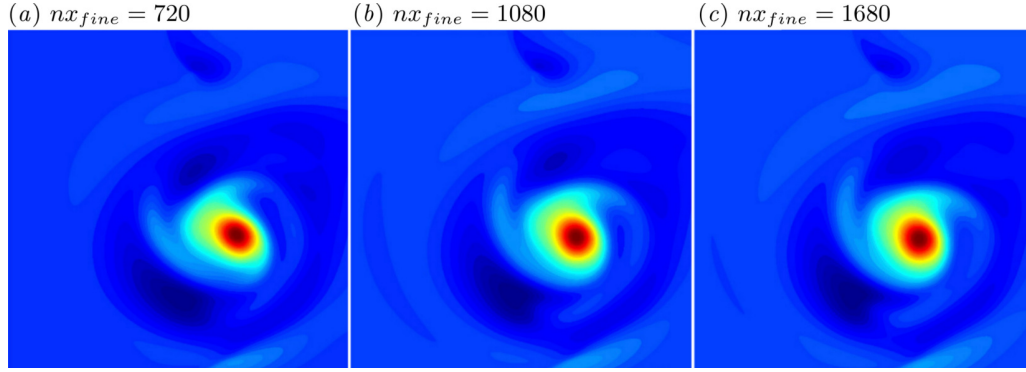


Figure A.1: Convergence tests of run C showing vorticity fields after the vortex has passed through the flame.
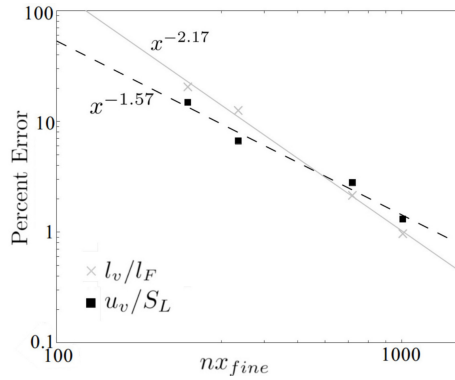


Figure A.2: Error in the vortex size and velocity after completion of burning based on grid resolution. The case of $nx_{fine} = 1680$ and $\Delta t = 5.7 \times 10^{-9}$s is taken as the exact solution.

expected to be the most difficult case to resolve.

Run C is simulated with five different grid resolutions: $nx_{fine} = 240$, 336, 720, 1008, and 1680, where $nx_{fine}$ is the number of grid point in $x$ within the central uniform mesh. These cases use the determined domain size and time step listed previously. One additional test with $nx_{fine} = 1680$ is performed using a smaller time step, $\Delta t = 5.7 \times 10^{-9}$s. Against this run, the others are compared.

To determine convergence, three items are investigated: the presence of negative mass fractions, the fields of temperature and vorticity, and the final vortex characteristics. First, negative mass fractions are due to numerical errors, which may be removed by increasing the grid resolution. Here, negative mass fractions are found for multiple species in non-negligible quantities when $nx_{fine} = 720$ or less. Finer grids do not possess the duration or quantity of negative mass fractions, with at most one species with a negative value. Second, the vorticity and temperature fields show qualitative

convergence for $nx_{fine} = 1080$. Figure A.1 displays vorticity fields $nx_{fine} = 720$, 1080, and 1680 at the completion of burning. These plots show little difference between the latter two, but the first vortex has differences in shape and orientation. Third, the velocity and length scale of the final vortex is computed for each of the tests. In Fig. A.2, the differences between these values and the most resolved are compared. This reveals near second-order convergence of the global flow field based on grid spacing. For $nx_{fine} = 1080$, the error in the vortex characteristics is near 1%. Based on all these results, it is determined that with $nx_{fine} = 1080$ the simulation is sufficiently converged. The convergence study supports that the simulations performed under these conditions capture all the relevant physics of this vortex-flame interaction.

For $nx_{fine} = 1080$, the number of points across the flame is approximately 55 and the number of points across the vortex is 180. These requirements on $n_F$ and $n_v$ are much more stringent than for an isolated vortex or flame. These requirements are placed on all the simulations, but are likely over restrictive for small values of $u_v/S_L$, as it is expected that the coupling is less severe.

## A.2    Tabulated chemistry

The analytical analysis in section 3.2 assumes the flame maintains the species temperature mapping of the one-dimensional flame by the use of tabulated chemistry. The validity of this assumption is tested by comparing the flame structure in the simulations and that of the one-dimensional flame. This is possible because of the use of detailed chemistry and is performed by plotting the temperature versus species mass fractions for every point in the domain. For run C, figures for two species are presented, $H_2O$ and OH, at the time when the deviation from the one-dimensional flame is approximately the greatest, Fig. A.3. For $H_2O$, the results of the vortex flame interaction fall almost identically onto the one-dimensional flame structure. This is especially important because this species is often used as the progress variable in $H_2$-air chemistry. For OH, the results show only slight deviations. These two examples are representative of the other species. $H_2O_2$, however, shows a greater discrepancy, but is a minor species. These results support that for the analytical analysis, the use of a progress variable in place of detailed chemistry introduces only small errors in
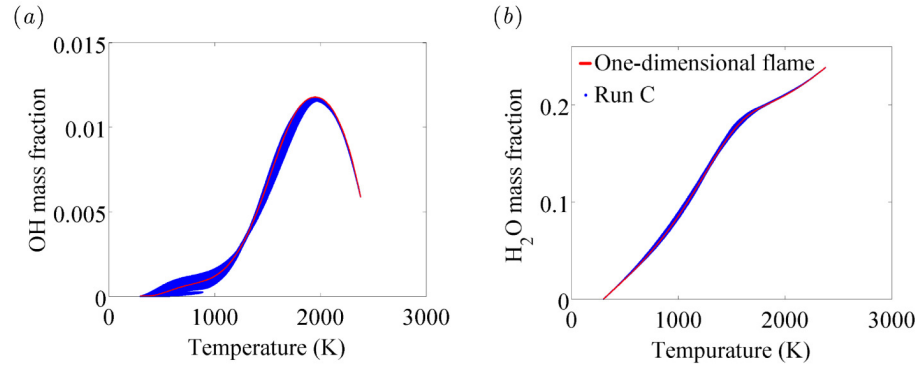
Figure A.3: Comparison of species mass fraction obtained with detailed chemistry, blue, with one-dimensional flame solution, red, for ($a$) OH and ($b$) $H_2O$.

the structure of the flame.

## A.3    Results detail

The simulation run conditions and final vortex characteristics are listed in table A.1. The vortex length scale and core circulation are obtained through identifying the vortex by the $\lambda_{ci}$ criterion [19]. Empty entries are a result of the vortex being effectively destroyed.

| Case | Run A | RunB | Run C | Run D | Run E |
|---|---|---|---|---|---|
| $L_x$ [m] | 0.00285 | 0.00285 | 0.0165 | 0.0378 | 0.0378 |
| $L_y$ [m] | 0.00114 | 0.00114 | 0.0165 | 0.0378 | 0.0378 |
| $nx_{fine}$ | 2528 | 2528 | 1008 | 2304 | 2304 |
| $ny_{fine}$ | 1011 | 1011 | 1008 | 2304 | 2304 |
| | | | | | |
| Initial Vortex | | | | | |
| $u_{\theta,max}$ [m/s] | 32.5 | 0.163 | 85 | 85 | 0.163 |
| $l_v$ [m]$\times 10^{-4}$ | 0.678 | 0.678 | 9.90 | 22.6 | 22.6 |
| $\omega_{max}$ [s$^{-1}$] $\times 10^5$ | 63.2 | 0.316 | 11.3 | 4.95 | 0.00947 |
| $\Gamma$ [m$^2$/s] $\times 10^{-2}$ | 0.346 | 0.00173 | 13.2 | 30.2 | 0.0578 |
| $Re_v$ | 100 | 0.51 | 3900 | 9000 | 17 |
| | | | | | |
| Final Vortex | | | | | |
| $u_{\theta,max}$ [m/s] | 11.2 | - | 29.9 | 46.0 | - |
| $l_v$ [m]$\times 10^{-4}$ | 1.68 | - | 22.1 | 49.7 | - |
| $\omega_{max}$ [s$^{-1}$] $\times 10^5$ | 8.35 | 0.0339 | 1.83 | 1.43 | - |
| $\Gamma$ [m$^2$/s] $\times 10^{-2}$ | 0.281 | - | 8.59 | 27.6 | - |

Table A.1: Simulation conditions with vortex initial and final characteristics. As the $\lambda_{ci}$ criterion only identifies the vortex core of the Taylor vortex, the calculated circulation is non-zero. Cases A and B have the same initial conditions as runs A$^v$ and B$^v$, respectively. The vortex Reynolds number is defined as $Re_v = u_{\theta,max} l_v/\nu$.

# Appendix B

# Normalized enstrophy transport equation

The scaling estimates in chapter 5 are used to propose a normalization of the entire enstrophy transport equation, which is then given by,

$$\frac{1}{2}\frac{D\hat{\omega}^2}{D\hat{t}} = Ka\hat{T}_1 + \gamma\hat{T}_2 + \alpha\gamma\sqrt{Ka}\hat{T}_3 + Ka\hat{T}_4 + \frac{1}{2Da}\hat{T}_5, \tag{B.1}$$

where, $\hat{t} = t/\tau_F$, $\hat{\omega}^2 = \langle \omega^2|C\rangle\tau_\eta^2$, and the Damköhler number is $Da = \tau_o/\tau_F$. Additionally, $Ka$ is the local Karlovitz number, $Ka(C)$, and the quantities $\gamma$ and $\alpha$ are assumed to be only function of the progress variable and defined through the relations $\gamma(C) = \Delta\rho/\langle\rho|C\rangle$ and $\nu(C) = \alpha(C)^2 S_L l_F$, respectively. The term $\hat{T}_1$ is the normalized vortex stretching term,

$$\hat{T}_1 = \langle \boldsymbol{\omega} \cdot S \cdot \boldsymbol{\omega}|C\rangle \left(\frac{1}{\tau_\eta^3}\right)^{-1}. \tag{B.2}$$

$\hat{T}_2$ is the normalized dilatation term,

$$\hat{T}_2 = \langle \boldsymbol{\omega}(\nabla \cdot \boldsymbol{u})|C\rangle \left(\gamma\frac{S_L}{l_F\tau_\eta^2}\right)^{-1}. \tag{B.3}$$

$\hat{T}_3$ is the normalized baroclinic torque term,

$$\hat{T}_3 = \langle \frac{\boldsymbol{\omega}}{\rho^2} \cdot (\nabla\rho \times \nabla P)|C\rangle \left(\gamma\frac{u_\eta}{l_F\tau_\eta^2}\right)^{-1}. \tag{B.4}$$

$\hat{T}_4$ is the normalized viscous dissipation term,

$$\hat{T}_4 = \langle \boldsymbol{\omega} \cdot \nabla \times \frac{\nabla \cdot \tau}{\rho} | C \rangle \left( \frac{1}{\tau_\eta^3} \right)^{-1}. \tag{B.5}$$

Lastly, $\hat{T}_5$ is the normalized forcing term,

$$\hat{T}_5 = \langle \boldsymbol{\omega} \cdot \nabla \times \frac{\boldsymbol{f}}{\rho} | C \rangle \left( \frac{1}{2\tau_o \tau_\eta^2} \right)^{-1}. \tag{B.6}$$

# Appendix C

# Transport equation for vorticity anisotropy

The terms in the transport equation for the anisotropy vector, $\boldsymbol{W}$, are provided explicitly here. This equation is written as

$$\frac{1}{2}\frac{D\boldsymbol{W}}{Dt} = \boldsymbol{A}_1 + \boldsymbol{A}_2 + \boldsymbol{A}_3 + \boldsymbol{A}_4 + \boldsymbol{A}_5, \tag{C.1}$$

where each term on the right hand side is associated with a specific physical process: production/vortex stretching, dilatation, baroclinic torque, viscous dissipation, and forcing, respectively. The anisotropic production term is written as

$$\boldsymbol{A}_{1,i} = \omega_i \boldsymbol{e}_i \cdot S \cdot \boldsymbol{\omega} - \frac{1}{3}\boldsymbol{\omega} \cdot S \cdot \boldsymbol{\omega}, \tag{C.2}$$

anisotropic dilatation may be written as

$$\boldsymbol{A}_2 = (-\boldsymbol{W})(\nabla \cdot \boldsymbol{u}), \tag{C.3}$$

anisotropic baroclinic torque writes

$$\boldsymbol{A}_{3,i} = \frac{\omega_i \boldsymbol{e}_i}{\rho^2} \cdot (\nabla \rho \times \nabla P) - \frac{1}{3}\frac{\boldsymbol{\omega}}{\rho^2} \cdot (\nabla \rho \times \nabla P), \tag{C.4}$$

anisotropic viscous dissipation is written as

$$\boldsymbol{A}_{4,i} = \omega_i \boldsymbol{e}_i \cdot \nabla \times \frac{\nabla \cdot \tau}{\rho} - \frac{1}{3}\boldsymbol{\omega} \cdot \nabla \times \frac{\nabla \cdot \tau}{\rho},  \tag{C.5}$$

and, lastly, anisotropic forcing takes the form

$$\boldsymbol{A}_{5,i} = \omega_i \boldsymbol{e}_i \cdot \nabla \times \frac{\boldsymbol{f}}{\rho} - \frac{1}{3}\boldsymbol{\omega} \cdot \nabla \times \frac{\boldsymbol{f}}{\rho}.  \tag{C.6}$$

# Appendix D

# Eigenvalues of $S$

In this appendix, the eigenvalues of the strain-rate tensor, $S$, are discussed. Figure D.1 presents all three eigenvalues for cases A, B, $B_{Tab,1}$, $B_{Tab,1}^4$ and D. As a result of the velocity divergence generated by the flame's heat release, the sum of the eigenvalues is non-zero. In case D, however, their normalized sum is approximately zero and the effect on the eigenvalues is negligible. This is not true of the remaining cases. In case A, this sum is relatively large within the flame, and $\lambda_1$ and $\lambda_2$ increase over their respective values in homogeneous isotropic turbulence. Figure D.1b shows that the eigenvalues are very similar between cases B, $B_{Tab,1}$ and $B_{Tab,1}^4$.

The changes in the eigenvalues may be explained by comparing their magnitude to the flow divergence. The eigenvalues of $S$ are proportional to $(S:S)^{1/2}$, which scales with $1/\tau_\eta$ in homogeneous isotropic turbulence [112]. By writing the velocity divergence as $-(D\rho/Dt)/\rho$, the velocity divergence (as in chapter 5) is estimated as

$$\nabla \cdot \boldsymbol{u} \simeq \frac{-1}{\langle \rho | C \rangle} \frac{\Delta \rho}{l_F/S_L}. \tag{D.1}$$

The ratio of these two terms scales as

$$\frac{1/\tau_\eta}{\Delta \rho/(\rho l_F/S_L)} = \frac{1}{\gamma} Ka. \tag{D.2}$$

As this ratio gets smaller, the flow divergence increases in magnitude compared to velocity gradients due to the turbulence. Therefore, at high flame density ratios and low Karlovitz numbers, the flame

(a) Cases A, B, and D.

(b) Cases B, $B_{\text{Tab},1}$, and $B_{\text{Tab},1}^4$.
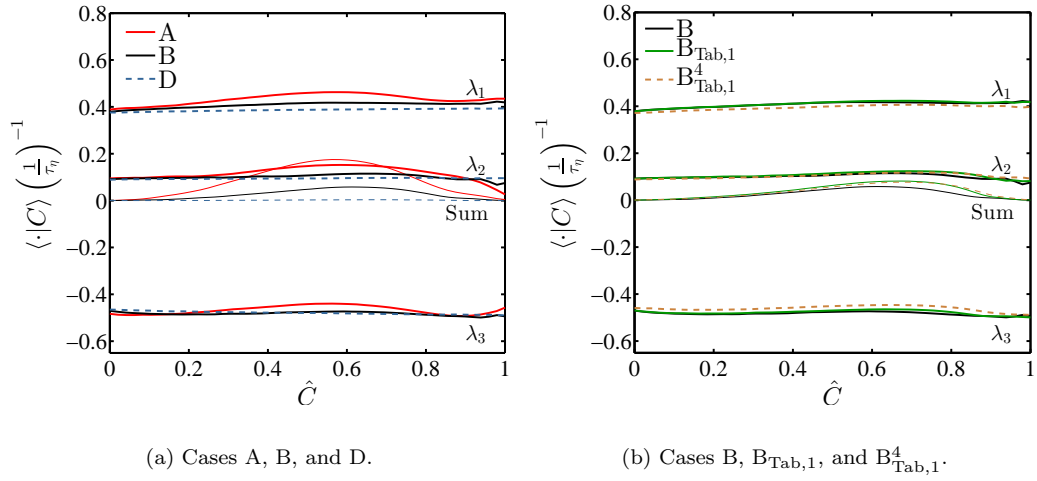
Figure D.1: Eigenvalues of the strain-rate tensor normalized by $1/\tau_\eta$ for cases (a) A, B, and D; and (b) B, $B_{\text{Tab},1}$, and $B_{\text{Tab},1}^4$.
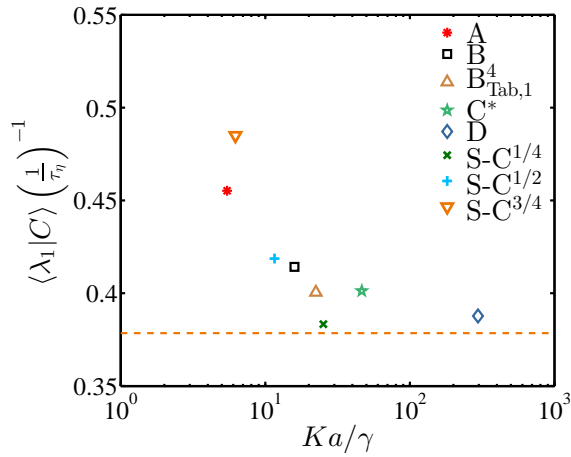


Figure D.2: Normalized value of $\lambda_1$ as a function of $Ka/\gamma$ evaluated at $\hat{C} = 0.55$. Dashed line is calculated from the previous simulation of homogeneous, isotropic turbulence ($Re_t = 201$) by Carroll *et al.* [13].

is able to induce greater changes in the eigenvalues. This scaling confirms the dependence of the magnitude of the eigenvalues on the Karlovitz number (Fig. D.1a) and the independence of the ratio of the integral length scale to the flame thickness (Fig. D.1b). In other words, this observed behavior should not be configuration dependent. Figure D.2 presents $\lambda_1$ evaluated at $\hat{C} = 0.55$ as a function of $Ka/\gamma$ including the high Karlovitz number slot Bunsen flames of Sankaran *et al.* [99]. There is fairly good agreement between these very different configurations.

# Bibliography

[1] Wm. T. Ashurst, A. R. Kerstein, R. M. Kerr, and C. H. Gibson. Alignment of vorticity and scalar gradient with strain rate in simulated Navier–Stokes turbulence. *Phys. Fluids*, 30(8):2343–2353, 1987.

[2] A. J. Aspden, J. B. Bell, M. S. Day, S. E. Woosley, and M. Zingale. Turbulence-Flame Interactions in Type Ia Supernovae. *Astrophys. J.*, 689(2):1173–1185, 2008.

[3] A. J. Aspden, M. S. Day, and J. B. Bell. Turbulence–flame interactions in lean premixed hydrogen: transition to the distributed burning regime. *J. Fluid Mech.*, 680:287–320, 2011.

[4] A.J. Aspden, M.S. Day, and J.B. Bell. Lewis number effects in distributed flames. *Proc. Comb. Inst.*, 33(1):1473–1480, 2011.

[5] J. B. Bell, N. J. Brown, M. S. Day, M. Frenklach, J. F. Grcar, and S. R. Tonse. The dependence of chemistry on the inlet equivalence ratio in vortex-flame interactions. *Proceedings of the Combustion Institute*, 28:1933 – 1939, 2000.

[6] F. Bisetti, G. Blanquart, M. E. Mueller, and H. Pitsch. On the formation and early evolution of soot in turbulent nonpremixed flames. *Combust. Flame*, 159(1):317–335, 2012.

[7] B. Bobbitt and G. Blanquart. Vorticity anisotropy in high Karlovitz number premixed flames. *Phys. Fluids*, page (To be submitted), 2015.

[8] B. Bobbitt, S. Lapointe, and G. Blanquart. Vorticity transformation in high Karlovitz number premixed flames. *Phys. Fluids*, 28(1), 2016.

[9] K.N.C. Bray, Paul A. Libby, Goro Masuya, J.B. R. Moss, and D. Escudie. Turbulence Production in Premixed Flames. *Combust. Sci. Technol.*, 25:127 – 140, 1981.

[10] N. Burali, S. Lapointe, B. Bobbitt, G. Blanquart, and Y. Xuan. Assessment of the constant non-unity Lewis number assumption in chemically-reacting flows. *Combust. Theor. Model.*, [Accepted].

[11] P. L. Carroll and G. Blanquart. A proposed modification to Lundgren's physical space velocity forcing method for isotropic turbulence. *Phys. Fluids*, 25 (2013)(105114).

[12] P. L. Carroll and G. Blanquart. The effect of velocity field forcing techniques on the Karman–Howarth equation. *J. Turbul.*, 15(7):429–448, 2014.

[13] P. L. Carroll, S. Verma, and G. Blanquart. A novel forcing technique to simulate turbulent mixing in a decaying scalar field. *Phys. Fluids*, 25(9), 2013.

[14] N. Chakraborty. Statistics of vorticity alignment with local strain rates in turbulent premixed flames. *European Journal of Mechanics - B/Fluids*, 46(0):201 – 220, jul 2014.

[15] N. Chakraborty, M. Katragadda, and R. S. Cant. Effects of Lewis number on turbulent kinetic energy transport in premixed flames. *Phys. Fluids*, 23(7):–, 2011.

[16] N. Chakraborty, M. Katragadda, and R. S. Cant. Statistics and Modelling of Turbulent Kinetic Energy Transport in Different Regimes of Premixed Combustion . *Flow Turbul. Combust.*, 87:205 – 235, 2011.

[17] N. Chakraborty and N. Swaminathan. Influence of the Damköhler number on turbulence-scalar interaction in premixed flames. I. Physical insight. *Phys. Fluids*, 19(4), 2007.

[18] N. Chakraborty and N. Swaminathan. Influence of the Damköhler number on turbulence-scalar interaction in premixed flames. II. Model development. *Phys. Fluids*, 19(4), 2007.

[19] P. Chakraborty, S. Balachandar, and R. J. Adrian. On the relationships between local vortex identification schemes. *Journal of Fluid Mechanics*, 535:189–214, 2005.

[20] R. K. Cheng, D. Littlejohn, W. A. Nazeer, and K. O. Smith. Laboratory Studies of the Flow Field Characteristics of Low-Swirl Injectors for Adaptation to Fuel-Flexible Turbines. *J. Eng. Gas Turb. Power*, 130:021501–1, 2008.

[21] R. A. Clark, J. H. Ferziger, and W. C. Reynolds. Evaluation of subgrid-scale models using an accurately simulated turbulent flow. *J. Fluid Mech.*, 91:1–16, 3 1979.

[22] S. G. Davis, A. V. Josh, H. Wang, and F. Egolfopoulos. An optimized kinetic model of H2/CO Combustion. *Proc. Comb. Inst.*, 30:1283–1292, 2005.

[23] O. Desjardins, G. Blanquart, G. Balarac, and H. Pitsch. High order conservative finite difference scheme for variable density low Mach number turbulent flows. *J. Comput. Physics*, 26:7125–7159, 2008.

[24] J. Driscoll. "Premixed turbulent combustion in the high Reynolds number regime of thickened flamelets and distributed reactions". *AFOSR and ARO Basic Combustion Research Review*, Basic Research Innovation and Collaboration Center, Arlington, VA, 2 June 2014, Presentation.

[25] J. F. Driscoll. Turbulent premixed combustion: Flamelet structure and its effect on turbulent burning velocities. *Progr. Energ. Combust.*, 34(1):91–134, 2008.

[26] J. F. Driscoll, D.J. Sutkus, Wm. L. Roberts, M.E. Post, and L. P. Goss. *The strain exerted by a vortex on a flame - Determined from velocityfield images.* Aerospace Sciences Meetings. American Institute of Aeronautics and Astronautics, Jan 1993.

[27] T. D. Dunstan, N. Swaminathan, K. N.C. Bray, and R. S. Cant. Geometrical Properties and Turbulent Flame Speed Measurements in Stationary Premixed V-flames Using Direct Numerical Simulation . *Flow Turbul. Combust.*, 87(2-3):237–259, 2011.

[28] S.B. Dworkin, M.D. Smooke, and V. Giovangigli. The impact of detailed multicomponent transport and thermal diffusion effects on soot formation in ethylene/air flames. *P. Combust. Inst.*, 32(1):1165–1172, 2009.

[29] Environmental Protection Agency. Proposed Finding That Greenhouse Gas Emissions From Aircraft Cause or Contribute to Air Pollution That May Reasonably Be Anticipated To Endanger Public Health and Welfare and Advance Notice of Proposed Rulemaking. *Federal Register*, 80(126):37758 – 37806, July 1, 2015.

[30] Environmental Protection Agency. Control of Air Pollution From Aircraft and Aircraft Engines; Emission Standards and Test Procedures. *Federal Register*, 77(117):36342 – 36386, June 18, 2012.

[31] A. Eucken. *Physik Z.*, 14:324–33, 1913.

[32] R.D. Falgout and U.M. Yang. HYPRE: a library of high performance preconditioners. In PeterM.A. Sloot, AlfonsG. Hoekstra, C.J.Kenneth Tan, and JackJ. Dongarra, editors, *Computational Science*, volume 2331 of *Lecture Notes in Computer Science*, pages 632–641. Springer, ICCS 2002.

[33] O. Gicquel, N. Darabiha, and D. Thévenin. Liminar premixed hydrogen/air counterflow flame simulations using flame prolongation of ILDM with differential diffusion. *Proc. Comb. Inst.*, 28(2):1901–1908, 2000.

[34] X. Gou, W. Sun, Z. Chen, and Y. Ju. A dynamic multi-timescale method for combustion modeling with detailed and reduced chemical kinetic mechanisms. *Combust. Flame*, 157(6):1111–1121, 2010.

[35] F. F. Grinstein, L. G. Margolin, and W. J. Rider. *Implicit Large Eddy Simulation*. Cambridge University Press, 2007.

[36] G. Gulitski, M. Kholmyansky, W. Kinzelbach, B. Lüthi, A. Tsinober, and S. Yorish. Velocity and temperature derivatives in high- Reynolds-number turbulent flows in the atmospheric surface layer. Part 3. Temperature and joint statistics of temperature and velocity derivatives. *Journal of Fluid Mechanics*, 589:103–123, 10 2007.

[37] P. E. Hamlington, A. Y. Poludnenko, and E. S. Oran. Intermittency in premixed turbulent reacting flows. *Phys. Fluids*, 24(7), 2012.

[38] Peter E. Hamlington, Alexei Y. Poludnenko, and Elaine S. Oran. Interactions between turbulence and flames in premixed reacting flows. *Phys. Fluids*, 23(12), 2011.

[39] C. Hassa. Partially Premixed and Premixed Aero Engine Combustors. In Tim C. Lieuwen and Vigor Yang, editors, *Gas Turbine Emissions*, pages 237–289. Cambridge University Press, 2013. Cambridge Books Online.

[40] E. R. Hawkes, R. Sankaran, J. C. Sutherland, and J. H. Chen. Scalar mixing in direct numerical simulations of temporally evolving plane jet flames with skeletal CO/H2 kinetics . *Proceedings of the Combustion Institute*, (31):1633 – 1640, 2007.

[41] M. Herrmann, G. Blanquart, and V. Raman. Flux Corrected Finite Volume Scheme for Preserving Scalar Boundedness in Reacting Large-Eddy Simulations. *AIAA Journal*, 44(12):2879–2886, 2014/12/16 2006.

[42] C. W. Higgins, M. B. Parlange, and C. Meneveau. Alignment Trends of Velocity Gradients and Subgrid-Scale Fluxes in the Turbulent Atmospheric Boundary Layer. *Bound Lay Meteorol*, 109(1):59 – 83, 2003.

[43] C. W. Higgins, M. B. Parlange, and C. Meneveau. The heat flux and the temperature gradient in the lower atmosphere. *Geophys Res Lett*, 31(22), 2004.

[44] O. Hirschfelder, C. Curtiss, and R. Bird. *Molecular Theory of Gases and Liquids*. John Wiley and Sons, 1954.

[45] F. A. Jaberi, D. Livescu, and C. K. Madnia. Characteristics of chemically reacting compressible homogeneous turbulence. *Phys. Fluids*, 12(5):1189–1209, 2000.

[46] J.r Jiménez, A. A. Wray, P. G. Saffman, and R. S. Rogallo. The structure of intense vorticity in isotropic turbulence. *J. Fluid Mech.*, 255:65–90, 10 1993.

[47] R. M. Kerr. Higher-order derivative correlations and the alignment of small-scale structures in isotropic numerical turbulence. *J. Fluid Mech.*, 153:31 – 58, 4 1985.

[48] A. R. Kerstein. Linear-eddy modelling of turbulent transport. Part 7. Finite-rate chemistry and multi-stream mixing. *J. Fluid Mech.*, 240:289–313, 7 1992.

[49] A. M. Klimov. Laminar flame in a turbulent flow. *Zhur. Prikl. Mekh. Tekh. Fiz.*, 3:49 – 58, 1963.

[50] Omar M Knio, Habib N Najm, and Peter S Wyckoff. A Semi-implicit Numerical Scheme for Reacting Flow: II. Stiff, Operator-Split Formulation. *J. Comput. Physics*, 154(2):428–467, 1999.

[51] E. Knudsen and H. Pitsch. A general flamelet transformation useful for distinguishing between premixed and non-premixed modes of combustion. *Combust. Flame*, 156(3):678 – 696, 2009.

[52] H. Kolla, E. R. Hawkes, A. R. Kerstein, N. Swaminathan, and J. H. Chen. On velocity and reactive scalar spectra in turbulent premixed flames. *J. Fluid Mech.*, 754:456–487, 9 2014.

[53] A. N. Kolmogorov. The local structure of turbulence in incompressible viscous fluid for very large reynolds numbers. *Dokl. Akad. Nauk SSSR*, (30):299–303, 1941.

[54] S. Lam. Singular perturbation for stiff equations using numerical methods. In Corrado Casci and Claudio Bruno, editors, *Recent Advances in the Aerospace Sciences*, pages 3–19. Springer, 1985.

[55] S. Lapointe, B. Savard, and G. Blanquart. Differential diffusion effects, distributed burning, and local extinctions in high Karlovitz premixed flames. *Combust. Flame*, 162(9):3341–3355, 2015.

[56] S. K. Lele. Compressibility effects on turbulence. *Ann. Rev. Fluid Mech.*, 26:211 – 254, 1994.

[57] B. P. Leonard. A stable and accurate convective modelling procedure based on quadratic upstream interpolation. *Comput. Methods Appl. M.*, 19:59 – 98, 1979.

[58] A. N. Lipatnikov and J. Chomiak. Effects of Premixed Flames on Turbulence and Turbulent Scalar Transport. *Prog. Energ. Combust.*, 36:1–102, 2010.

[59] A. N. Lipatnikov, S. Nishiki, and T. Hasegawa. A direct numerical simulation study of vorticity transformation in weakly turbulent premixed flames. *Phys. Fluids*, 26(10), 2014.

[60] D.S. Louch and K.N.C. Bray. Vorticity and scalar transport in premixed turbulent combustion. *Symposium (International) on Combustion*, 27:801 – 810, 1998.

[61] T. S. Lundgren. Linearly Forced isotropic turbulence. *Center Turbul. Res. Annu. Res. Briefs*, pages 461–473, 2003.

[62] M. Parviz and S. V. Apte. Large-Eddy Simulation of Realistic Gas Turbine Combustors. *AIAA Journal*, 44(4):698–708, 2006. doi: 10.2514/1.14606.

[63] U. Maas and S. Pope. Simplifying chemical kinetics: Intrinsic low-dimensional manifolds in composition space. *Combust. Flame*, 88(3–4):239–264, 1992.

[64] A. Majda. *Compressible Fluid Flow and Systems of Conservation Laws in Several Space Variables*, volume 53. 1984.

[65] A. Majda and J. Sethian. The Derivation and Numerical Solution of the Equations for Zero Mach Number Combustion. *Combust. Sci. Technol.*, 42(3-4):185–205, 1985.

[66] M. Matalon and B. J. Matkowsky. Flames as gasdynamic discontinuities . *Journal of Fluid Mechanics*, 124:239 – 259, 1982.

[67] S. Mathur, P.K. Tondon, and S.C. Saxena. Thermal conductivity of binary, ternary and quaternary mixtures of rare gases. *Mol. Phys.*, 12(6):569–579, 1967.

[68] S. Menon and W. H. Calhoon Jr. Subgrid mixing and molecular transport modeling in a reacting shear layer. *Proc. Comb. Inst.*, 26(1):59–66, 1996.

[69] S. K. Menon, P. A. Boettcher, and G. Blanquart. Enthalpy based approach to capture heat transfer effects in premixed combustion. *Combust. Flame*, 160(7):1242 – 1253, 2013.

[70] A. Misra and D. I. Pullin. A vortex-based subgrid stress model for large-eddy simulation. *Phys. Fluids*, 9(8):2443 – 2454, 1997.

[71] J. P. Moeck, J. Bourgouin, D. Durox, T. Schuller, and S. Candel. Nonlinear interaction between a precessing vortex core and acoustic oscillations in a turbulent swirling flame . *Combust. Flame*, 159:2650 – 2668, 2012.

[72] S. C. Morris and J. F. Foss. Vorticity spectra in high Reynolds number anisotropic turbulence. *Phys. Fluids*, 17(8), 2005.

[73] C. J. Mueller, J. F. Driscoll, D. L. Reuss, M. C. Drake, and M. E. Rosalik. Vorticity generation and attenuation as vortices convect through a premixed flame. *Combust. Flame*, 112:342 – 346, 1998.

[74] M. E. Mueller and H. Pitsch. LES model for sooting turbulent nonpremixed flames. *Combust. Flame*, 159(6):2166–2180, 2012.

[75] L. Mydlarski and Z. Warhaft. On the onset of high-Reynolds-number grid-generated wind tunnel turbulence . *J. Fluid Mech.*, 320:331 – 368, 1996.

[76] H. N. Najm, P. S. Wyckoff, and O. M. Knio. A semi-implicit numerical scheme for reacting flow: I. stiff chemistry. *J. Comput. Physics*, 143(2):381–402, 1998.

[77] S. Nishiki, T. Hasegawa, R. Borghi, and R. Himeno. Modeling of Flame-Generated Turbulence Based on Direct Numerical Simulation Databases. *Proc. Combust. Inst.*, 29:2017 – 2022, 2002.

[78] N Peters. Laminar flamelet concepts in turbulent combustion. In *21st Symposium (International) on Combustion*, number 1, pages 1231–1250. Combustion Institute, 1986.

[79] N. Peters. *Turbulent Combustion.* Cambridge University Press, 2000.

[80] C.D. Pierce. *Progress-variable approach for large-eddy simulation of turbulent combustion.* PhD thesis, Stanford University, 2001.

[81] H. Pitsch. A C++ Computer Program for 0D Combustion and 1D Laminar Flame Calculations. http://www.itv.rwth-aachen.de/downloads/flamemaster/, 1998.

[82] H. Pitsch. Large-Eddy Simulation of Turbulent Combustion . *Ann. Rev. Fluid Mech.*, 38:453 – 482, 2006.

[83] T. Poinsot, D Veynante, and S. Candel. Quenching processes and premixed turbulent combustion diagrams. *J. Fluid Mech.*, 228:561–606, 1991.

[84] A. Y. Poludnenko. Pulsating instability and self-acceleration of fast turbulent flames. *Physics of Fluids*, 27(1), 2015.

[85] A. Y. Poludnenko and E. S. Oran. The interaction of high-speed turbulence with flames: Global properties and internal flame structure. *Combust. Flame*, 157:995–1011, 2010.

[86] A. Y. Poludnenko and E. S. Oran. The interaction of high-speed turbulence with flames: Turbulent flame speed. *Combust. Flame*, 158:301–326, 2011.

[87] S. B. Pope. *Turbulent Flows*. Cambridge University Press, 2000.

[88] C. Poulain, N. Mazellier, P. Gervais, Y. Gagne, and C. Baudet. Spectral Vorticity and Lagrangian Velocity Measurements in Turbulent Jets. *Flow, Turbul. Combust.*, 72(2-4):245–271, 2004.

[89] D. I. Pullin. A vortex-based model for the subgrid flux of a passive scalar. *Phys. Fluids*, 12(9):2311–2319, 2000.

[90] J. Quinlan, J. C. McDaniel, T. G. Drozda, G. Lacaze, and J. C. Oefelein. A Priori Analysis of Flamelet-based Modeling for a Dual-Mode Scramjet Combustor. July 2014.

[91] J. D. Regele, E. Knudsen, H. Pitsch, and G. Blanquart. A two-equation model for nonunity Lewis number differential diffusion in lean premixed laminar flames. *Combust. Flame*, 160(2):240 – 250, 2013.

[92] P. H. Renard, D. Thévenin, J.C. Rolon, and S. Candel. Dynamics of flame/vortex interactions. *Progress in Energy and Combustion Science*, 26:225 – 282, 2000.

[93] W. L. Roberts, J. F. Driscoll, M. C. Drake, and L. P. Goss. Images of the Quenching of a Flame by a Vortex-To Quantify Regimes of Turbulent Combustion. *Combust. Flame*, 94:58–69, 1993.

[94] C. Rosales and C. Meneveau. Linear forcing in numerical simulations of isotropic turbulence: Physical space implementations and convergence properties. *Phys. Fluids*, 17 (2005)(095106), 2005.

[95] C. J. Rutland and J. H. Ferziger. Simulations of flame-vortex interactions. *Combust. Flame*, 84:343 – 360, 1991.

[96] P. G. Saffman. *Vortex Dynamics*. Cambridge University Press, 1992.

[97] P. Sagaut. *Large eddy simulation for incompressible flows*. Springer, 2001.

[98] R. Sankaran, E. R. Hawkes, J. H. Chen, T. Lu, and C. K. Law. Structure of a spatially developing turbulent lean methane–air Bunsen flame . *P. Combust. Inst.*, 31:1291–1298, 2007.

[99] R. Sankaran, E. R. Hawkes, C. S. Yoo, and J. H. Chen. Response of flame thickness and propagation speed under intense turbulence in spatially developing lean premixed methane–air jet flames. *Combust. Flame*, 162(9):3294–3306, 2015.

[100] B. Savard. *Characterization and modeling of premixed turbulent n-heptane flames in the thin reaction zone regime*. PhD thesis, California Institute of Technology, 2015.

[101] B. Savard and G. Blanquart. An a priori model for the effective species Lewis numbers in premixed turbulent flames. *Combust. Flame*, 161(6):1547–1557, 2014.

[102] B. Savard and G. Blanquart. Broken reaction zone and differential diffusion effects in high Karlovitz n-C7H16 premixed turbulent flames. *Combust. Flame*, 162(5):2020 – 2033, 2015.

[103] B. Savard, B. Bobbitt, and G. Blanquart. Structure of a High Karlovitz n-C7H16 Premixed Turbulent Flame. *Proc. Comb. Inst.*, 35(2):1377–1384, 2015.

[104] B. Savard, Y. Xuan, B. Bobbitt, and G. Blanquart. A computationally-efficient, semi-implicit, iterative method for the time-integration of reacting flows with stiff chemistry. *J. Comput. Physics*, 295(0):740 – 769, 2015.

[105] J. Savre, H. Carlsson, and X.S. Bai. Turbulent Methane/Air Premixed Flame Structure at High Karlovitz Numbers. *Flow. Turbul. Combust.*, 90(2):325–341, 2013.

[106] L. Shunn, F. Ham, and P. Moin. Verification of variable-density flow solvers using manufactured solutions. *J. Comput. Physics*, 231(9):3801–3827, 2012.

[107] J. Smagorinsky. General circulation experiments with the primitive equations. *Mon. Wea. Rev.*, 91(3):99–164, 1963.

[108] T. Smith and S. Menon. Model simulations of freely propagating turbulent premixed flames. *Proc. Comb. Inst.*, 26(1):299–306, 1996.

[109] A. M. Steinberg, J. F. Driscoll, and N. Swaminathan. Statistics and dynamics of turbulence flame alignment in premixed combustion. *Combust. Flame*, 159:2576–2588, 2012.

[110] A.M. Steinberg, B. Coriton, and J.H. Frank. Influence of combustion on principal strain-rate transport in turbulent premixed flames. *Proc. Combust. Inst.*, 35:1287–1294, 2015.

[111] G. I. Taylor. Production and Dissipation of Vorticity in a Turbulent Fluid. *Proc. R. Soc. Lon. Ser.-A*, 164(916):15– 23, 1938.

[112] H. Tennekes and J. L. Lumley. *A first course in turbulence*. MIT Press, 1972.

[113] A. Tsinober, E. Kit, and T. Dracos. Experimental investigation of the field of velocity gradients in turbulent flows. *J. Fluid Mech.*, 242:169–192, 9 1992.

[114] U.S. Energy Information Administration. Annual Energy Outlook 2015 with projections to 2040. Washington, DC, 2015.

[115] C. M. Vagelopoulos and J. H. Frank. Transient response of premixed methane flames. *Combustion and Flame*, 146(3):572–588, 2006.

[116] J.A. van Oijen, F.A. Lammers, and L.P.H. de Goey. Modeling of complex premixed burner systems by using flamelet-generated manifolds. *Combust. Flame*, 127(3):2124–2134, 2001.

[117] S. Verma and G. Blanquart. Subfilter scalar-flux vector orientation in homogeneous isotropic turbulence. *Phys. Rev. E*, 89(6), 2014.

[118] S. Verma, Y. Xuan, and G. Blanquart. An improved bounded semi-Lagrangian scheme for the turbulent transport of passive scalars. *J. Comput. Physics*, 272:1–22, 2014.

[119] T. Voelkl, D. I. Pullin, and D. C. Chan. A physical-space version of the stretched-vortex subgrid-stress model for large-eddy simulation. *Phys. Fluids*, 12(7):1810–1825, 2000.

[120] C. R. Wilke. A Viscosity Equation for Gas Mixtures. *J. Chem. Phys.*, 18(4):517–519, 1950.

[121] F. A. Williams. Criteria for existence of wrinkled laminar flame structure of turbulent premixed flames. *Combust. Flame*, 26:269 – 270, 1976.

[122] F. A. Williams. *Combustion Theory*. Addison-Wesley, 2nd edition edition, 1985.

[123] M. Wu and J. F. Driscoll. A Numerical Simulation of a Vortex Convected Through a Laminar Premixed Flame . *Combust. Flame*, 91:310 – 322, 1992.

[124] Y. Xuan and G. Blanquart. Numerical modeling of sooting tendencies in a laminar co-flow diffusion flame. *Combust. Flame*, 160(9):1657–1666, 2013.

[125] Y. Xuan and G. Blanquart. Effects of aromatic chemistry-turbulence interactions on soot formation in a turbulent non-premixed flame. *Proc. Combust. Inst.*, 35(2):1911–1919, 2015.

[126] Y. Xuan, G. Blanquart, and M. E. Mueller. Modeling curvature effects in diffusion flames using a laminar flamelet model. *Combust. Flame*, 161(5):1294–1309, 2014.

[127] S. Zhang and C. J. Rutland. Premixed Flame Effects on Turbulence and Pressure-Related Terms. *Combust. Flame*, 102:447 – 461, 1995.